# Branched polystyrene model systems to investigate the rheology of polymer fiber spinning

Zur Erlangung des akademischen Grades eines

DOKTORS DER NATURWISSENSCHAFTEN

(Dr.rer. nat.)

Fakultät für Chemie und Biowissenschaften

Karlsruher Institut für Technologie (KIT) – Universitätsbereich

genehmigte

DISSERTATION

von

Dipl.-Ing. Kamran Riazi

aus

Teheran

Dekan: Prof. Dr. Reinhard Fischer

Referent: Prof. Dr. Manfred Wilhelm

Korreferent: Prof. Dr. Dr. Christian Friedrich

Tag der mündlichen Prüfung: 11.12.2017

Diese Arbeit wurde in der Zeit vom 01. Oktober 2012 bis zum 2. November 2017 am Institut für Technische Chemie und Polymerchemie des Karlsruher Instituts für Technologie (KIT) unter Anleitung von Prof. Dr. Manfred Wilhelm durchgeführt.

Hiermit versichere ich, dass ich die von mir vorgelegte Arbeit selbständig verfasst habe, dass ich die verwendeten Quellen und Hilfsmittel vollständig angegeben und die Stellen der Arbeit, die anderen Werken im Wortlaut oder dem Sinn nach entnommen sind, entsprechend kenntlich gemacht habe.

Karlsruhe, den 26. Oktober 2017

Kamran Riazi

*Für Azadeh*

# Abbreviations

| | |
|---|---|
| 4-(chlorodimethylsilyl)styrene | CDMSS |
| Advanced rheometric expansion system | ARES |
| Alternating current | AC |
| Angular frequency | $\omega$ |
| Apparent extensional viscosity | $\eta_{E,app}$ |
| Average angle of inclination of the molecules | $\varphi$ |
| Average molecular weight between entanglements | $M_e$ |
| Berry number | $B_e$ |
| Birefringence | $n_{\parallel} - n_{\perp}$ |
| Butyllithium | BuLi |
| Bulked continuous filament | BCF |
| Calcium hydride | $CaH_2$ |
| Capillary break-up extensional rheometer | CaBER |
| Complex modulus | $G^*$ |
| Contraction factor | g and g' |
| Critical crossover concentration | c* |
| Critical molecular weight | $M_c$ |
| deci tex | dtex |
| Degree of polymerization | $P_n$ |
| Dielectric constant | $\varepsilon_r$ |
| Differential refractive index | DRI |
| Dimethyl formamide | DMF |
| Direct current | DC |
| Dispersity | Đ |
| Draw-down ratio | $DDR$ |
| Entanglement concentration | $c_e$ |
| Entanglement molecular weight in solution | $(M_e)_{soln}$ |
| Extensional relaxation time | $\lambda_E$ |
| Extensional Viscosity Fixture | EVF |
| First normal stress differences | $N_1$ |
| Fourier transformation | FT |
| Fully oriented yarn | FOY |
| Glassy temperature | $T_g$ |
| Henckey strain | $\varepsilon_H$ |
| High density polyethylene | HDPE |
| Huggins coefficient | $k_H$ |
| Ideal gas constant | $R$ |
| Intrinsic viscosities of the branched polymer | $[\eta]_{br}$ |
| Intrinsic viscosities of the linear polymer | $[\eta]_l$ |
| Isotactic polypropylene | iPP |
| Length of the backbone | $M_{n,bb}$ |

| | |
|---|---|
| Shear modulus | $G$ |
| Shear rate | $\dot{\gamma}$ |
| Shear rate at the wall | $\dot{\gamma}_w$ |
| Shear stress | $\sigma$ |
| Shear stress at the wall | $\sigma_w$ |
| Shear stress in the dashpot | $\sigma_d$ |
| Shear stress in the spring | $\sigma_s$ |
| Size exclusion chromatography | SEC |
| Solvent interaction coefficient | $\chi$ |
| Specific viscosity | $\eta_{sp}$ |
| Storage modulus | $G'$ |
| Strain | $\gamma$ |
| Strain hardening factor | SHF |
| tert-Butyllithium | t-BuLi |
| Tetrahydrofurane | THF |
| Time dependent extensional stress | $\sigma_{ext}(t)$ |
| Time temperature superposition | TTS |
| Ultra high molecular weight polyethylene | UHMWPE |
| Uniaxial extensional viscosity | $\eta_E^+(t, \dot{\varepsilon}_H)$ |
| Volumetric flow rates | $Q$ |
| Weight average molecular weight | $M_w$ |
| William-Landel-Ferry equation | WLF |
| Zero shear viscosity | $\eta_0$ |

# Contents

# 1. Introduction

The term fiber reminds generally an image of flexible threads, beautiful garments and dresses, home furnishings and curtains, ropes and burlap sacks used for transporting commodities. Two types of fibers are available today: natural fibers, which have been used for at least 4000 years, and man-made fibers (fibers, those are made artificially), which first appeared about 120 years ago when Count Chardonnet invented artificial silk, an achievement that had been only a dream [1, 2].

Natural fibers are divided into three chemical classes [3], which are cellulosic, protein and mineral fibers. Cellulosic fibers are obtained from various plant parts, such as leaves, seeds and stems. The protein fibers are obtained from wool and silk. The only naturally occurring mineral fiber is asbestos, which is banned in many countries because of its carcinogenic properties [4].

Man-made fibers also fall into three groups, which are regenerated, synthetic and inorganic fibers. Regenerated fibers are made from natural sources (e.g. cellulose rayon, casein, alginate and soya). Synthetic fibers are produced mostly from non-renewable sources (e.g. polyester, polyamide and polyolefin). Glass, ceramic and metal fibers are examples of inorganic man-made fibers. The classification of the various types of textile fibers is shown in Figure 1.1.

Nowadays a wide range of textile fiber types are commercially available. In the early 1990s, equal amounts of natural and synthetic fibers were produced. In step with increasing textile product consumption, the worldwide demand for textile fibers has grown and reached about 95.6 million tons per year in 2015 [5]. As shown in Figure 1.2, the size of the synthetic fiber group is the largest at 62.1 % by mass, and its rapid increase is due to the demand for polyester fibers. Polyester fiber, specifically polyethylene terephthalate (PET), is the largest volume of synthetic fiber produced worldwide (Table 1.1). It is remarkable that, while nearly all regions of the world produce textile fibers, the last decade has seen a considerable amount of synthetic fiber production shifted to China. The largest synthetic fiber manufacturers in the world are China (70%), USA (4%), India (4%), Taiwan (3%) and Indonesia (2%) [6]. Whereas in 1994, only 13.5% of the world synthetic fiber production was located in China. The production of synthetic fibers in Germany experienced between 2005 and 2015 a drop from 926 to 628 thousand tons (see Table 1.2) [6].

Textile fibers

Man-made fibers

Natural fibers

**Man-made fibers**

Natural — Synthetic — Inorganic

Cellulose rayon
Viscose
Cupro
Lyocell

Cellulose esters
Acetate
Triacetate

Others
Casein
Alginate
Collagen
Soya
Rubber

Inorganic
Carbon
Glass
Metal

Polyvinyl derivatives
Polyvinyl alcohol (PVA)
Polyvinyl chloride (PVC)
Polyacrylonitrile (PAN)

Polyamide (PA)
Nylon 6
Nylon 66
Aramids

Polyester (PET)
Polyester

Polyolefin
Polypropylene (PP)
Polyethylene (PE)

Polyurethane
Elastane
e.g. Lycra

Special fibers
e.g.
Polybenzoxazol
Polytetrafluoroethylene (PTFE)

**Natural fibers**

Vegetable (cellulose) — Animal (protein) — Mineral

Bast fibers
Flax
Jute
Hemp
Ramie

Leaf fibers
Sisal
Manilla
Abaca

Seed fibers
Cotton
Coir
Kapok

Hair fibers
Cashmere
Mohair
Alpaca

Wool fibers

Silk fibers

Mineral
Asbestos

Figure 1.1: Classification of the various types of textile fibers [3].

synthetic fibers
cotton
wood-based regenerated fibers
wool
other natural fibers

25.2 %
6.4 %
1.2 %
5.1 %
62.1 %
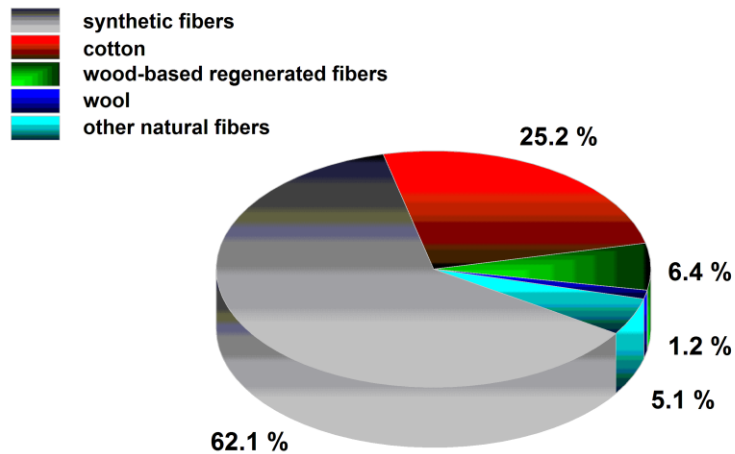
Figure 1.2: Share of the different fiber groups in the total world fiber consumption from 2015 [5]. Total production about 100 million tons, see Table 1.1.

Table1.1: Global production of selected textile fibers (million metric tons), 2015 [5, 6].

| Man-made fibers | | Natural fibers | |
|---|---|---|---|
| Polyester | 50.1 | Cotton | 24.6 |
| Cellulose | 6.0 | Wool | 1.3 |
| Polyamide | 4.7 | Others | 5.0 |
| Acrylic | 2.0 | | |
| Polypropylene | 2.7 | | |
| Others | 1.3 | | |
| | | | |
| Total | 66.8 | | 30.9 |

Table1.2: Production, export, import and number of workers related to the man-made fiber production in Germany between 2005-2015 [6].

| | 2005 | 2014 | 2015 |
|---|---|---|---|
| Production of fibers [$10^3$ tons] | 926 | 634 | 628 |
| • polyester | 281 | 195 | 182 |
| • polyacrylonitril | 192 | 165 | 173 |
| • polyamide | 171 | 68 | 67 |
| • other synthetics* | 83 | 15 | 28 |
| • cellulose | 199 | 191 | 178 |
| Export [$10^3$ tons] | 814 | 613 | 601 |
| Import [$10^3$ tons] | 459 | 609 | 612 |
| Sale of fibers [$10^9$ €] | 2.8 | 2.1 | 2.0 |
| Number of workers | 11500 | 7400 | 7300 |

* Polypropylene, polyurethane, and polyphenylene sulfone fibers.

A textile fiber is generally characterized by its flexibility, fineness and its high aspect ratio (ratio of the length to thickness of a fiber, generally > 1000) [7, 8]. In addition, if the fiber is to be of any use for general textile purposes, it must have a sufficiently high temperature stability, a certain minimum strength (steady force necessary to break a fiber, normalized to the cross-sectional area of the fiber) and moderate extensibility [8]. Ordinary textile fibers must be elastic up to breaking extensions between 5 and 50%. The materials, that meet these requirements and are used in textile applications are all linear polymers, that are partially crystalline and partially oriented (e.g. cellulosic, protein, polyamide, polyester, polyacrylonitrile and polypropylene fibers). Carbon fibers are oriented forms of imperfect graphitic crystals [7]. The inorganic fibers, glass and ceramic, are amorphous and less extensible, whereas organic fibers made from rubber are much more extensible compared to the ordinary textile fibers.

Fineness or linear mass density of fibers is one of the most important fiber characteristics. The standard unit of fiber fineness is tex, which is defined as the mass in grams per 1000 meters fiber length. Due to its closeness to the older unit denier (the mass in grams per 9000 meters fiber length), decitex (dtex, the mass in grams per 10000 meters fiber length) is widely used. Until the second half of the twentieth century, textile fibers had typical diameters between 10 and 50 $\mu$m, which corresponds to roughly 1 to 25 dtex [3, 7].

Many fibers do not have a uniform cross-sectional area. In the textile literature, the conventional engineering definition of stress (force/unit area) is replaced by tenacity (specific strength), which is force/linear mass density [2], and has the units of N/tex.

The process of producing fibers from the liquid state is called spinning. There are a few variations on the basic fiber spinning process [2, 3]. The most common method of fiber formation is called melt spinning, which means that the fiber is produced from a melt. This process is used for the production of fibers from organic polymers (and glasses). An appropriate thermoplastic polymer (e.g. PET), generally in the form of dry pellets, is fed into an extruder. The pellets are melted inside the extruder and pushed through a spinneret that consists of very tiny holes (e.g. rectangular spinneret with up to 1300 holes, 26 cm x 6.5 cm, diameter of capillary holes D = 0.3 mm [9]) to form filaments (single fibers with a continuous length). The molten polymer solidifies as the filaments exit the spinneret (see Figure 1.3) by quench air, which is blown over the filaments. Then the fibers are stretched and collected on a take-up device

(godets, winder or an air suction device) [9]. The next step is the drawing of filaments between two rolls with different speeds in order to orient the molecules and increase the filament strength.

The polymer extruded from a capillary directly after the die exit always has a larger diameter than the used capillary. This increase in the diameter of the extrudate is called die swell [10].
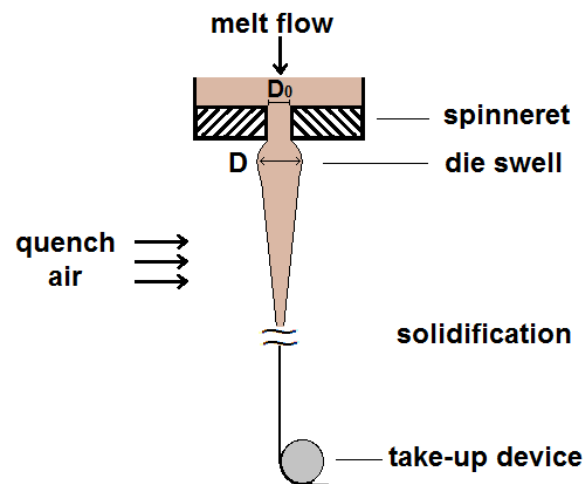


Figure 1.3: Schematic figure of the deformation of a single filament in the melt spinning process.

Melt spinning is used to produce polyamide (e.g. polyamide 66), polyester (e.g. polyethylene terephthalate) and polyolefin (e.g. polypropylene) fibers (see Figure 1.4). The production of some of the most important fibers from these groups is described in the following.

 Only a few of the known polyamides have reached large scale consumption in the textile industry. Nylon is the generic name for polyamides that are predominantly aliphatic. In textile applications only polyamide 66 (PA66 or nylon 66) and polyamide 6 (PA6 or nylon 6) are used in large scale production. Poly(hexamethylene adipamide) [11, 12], referred to as polyamide 66, is synthesized through polycondensation of hexamethylene diamine and adipic acid. Polyamide 6 is produced by the ring-opening polymerization of $\varepsilon$-caprolactam [12]. The mechanical properties of polyamide 66 and polyamide 6 are quite similar [3, 8]. In textile applications, polyamide fibers are mostly used for tights, swimwear and lingerie [3]. The number average molecular weight of the polyamides used in textile applications is between 15 and 30 kg/mol [13].

Polyethylene terephthalate (PET) was invented about 75 years ago [13], and is widely used to make synthetic fibers, films and bottles. The PET manufactured

through polycondensation includes dimethyl terephthalate and ethylene glycol among its starting materials [14]. The PET fibers are used in apparel (clothing), household, medical and industrial applications. Blends of PET and cotton or wool fibers can be used in shirts, skirt and dresses [3]. The number average molecular weight of the polymer used for clothes is about 20 kg/mol with a degree of polymerization of approximately 100. For tires and seatbelts, which require to have higher strength, PET has a number average molecular weight of 30 kg/mol or more [14].

Polypropylene is the most important polyolefin fiber. The melting point of polypropylene (isotactic) is about 165 °C, which is low in comparison with polyamide 66 ($T_m \sim 264$ °C ) or PET ($T_m = 265$ °C) [15], but is anyway high enough to make it suitable for most textile applications. Polypropylene fibers are highly resistant to mechanical abuse and chemical attack. This is why they are widely used in industrial carpet and geotextile applications. The number average molecular weight of the polypropylene used in textile applications is between 200 and 350 kg/mol [13].



polyamide 66
(nylon 66)

polyamide 6
(nylon 6)

polyethylene terephthalate
(PET)

isotactic
polypropylene
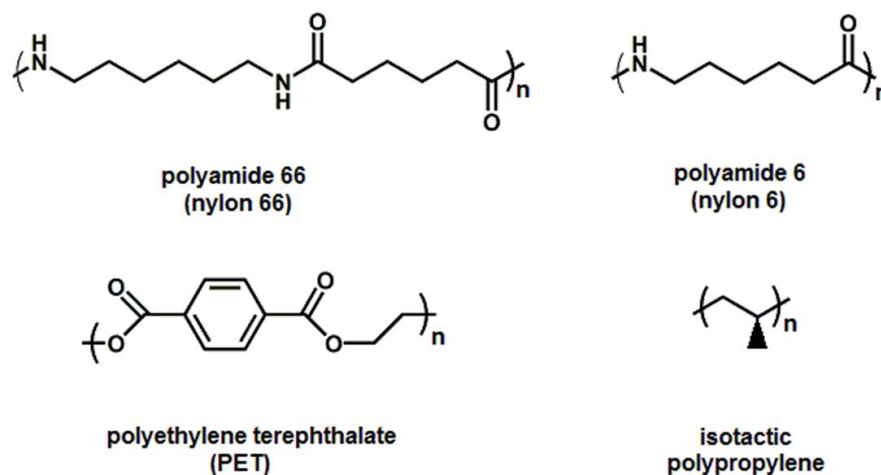
Figure 1.4: Schematic of the chemical structure of the most important synthetic polymers in the melt spinning process.

Polyethylene is more challenging to spin via the melt spinning process than polypropylene [16]. The first commercial application of polyethylene fibers was in the automobile industry in the late 1940s. The fibers made from low density polyethylene were not successful because of the lack of dimensional instability, abrasion resistance, resilience, and light stability [17]. Increasing commercial importance of polyethylene fibers began with high density polyethylene in the late 1950s. Ultra high molecular weight polyethylene (UHMWPE), with a molecular weight in the range of 3-

6 million g/mol, shows high-strength properties(because of extremely good orientation of the polymer chains in the fiber direction) and low-weight fiber utilization [18, 19]. The UHMWPE fibers are manufactured via a gel spinning process [20, 21] because molten ultra high molecular weight polyethylene is too viscous to be processed at any reasonable rate. The produced fiber is composed of extended, fully oriented polyethylene chains, which gives the fibers their outstanding strength. In fact, it is one of the world's strongest and lightest fibers, up to 40 % stronger than Kevlar fibers [8].

Solution spinning is the other major process for fiber formation. This method is adapted for the polymers that cannot be melt extruded (e.g. cellulosic fibers, polyacrylonitrile). Depending on the method by which the solvent is removed, solution spinning can be divided into two main groups, dry and wet spinning. In the dry spinning process, the solvent is removed through flows of warm gas suitably directed at the extruded filaments. In the wet spinning process, the solvent is removed from a polymer solution by coagulation of the polymer in another liquid, which behaves as a solvent towards the polymer solvent and a non-solvent towards the polymer itself [13].

Nowadays, spinning processes (melt, dry and wet spinning) typically result in fibers with diameters between 1 and 20 $\mu$m. Recently, interest in developing materials at the nanoscale has led to an increase in the activity to produce fibers with submicron diameters [22]. The main method for the production of nanofibers with these diameters is electrospinning [22-24]. In electrospinning a charged polymer solution is subjected to an electrical field as it flows through a metal orifice. Electrospinning can be used for synthetic and natural polymers, polymer alloys, and functional polymers. Due to the high surface area, high porosity and small pore size, the nanofibers are proposed for applications such as filtration, membranes, drug delivery, protective closing, optical sensors and tissue engineering [22].

## 1.1 Outline of the thesis

This study contains four main chapters. Each of these chapters contains an introduction, the respective theory, results and conclusion.

Chapter 2 describes the synthesis and molecular characterization of polystyrene with linear and comb architectures. All combs have well-defined backbone and side chain lengths, low dispersities, and a small amount of long or short chain branches. The length and number of branches was varied, but the total number of monomers in the side chains was kept constant. These model polymers were then used for rheological characterization and in fiber spinning processes.

In Chapter 3, the focus is on the rheological characterization of model polymers. The combs are investigated in the linear regime using the van Gurp-Palmen plot. The influence of length and number of branches was examined. The uniaxial extensional measurements were also investigated. These measurements were related to the melt spinning of model polymers.

Chapter 4 focuses on the melt spinning process. The knowledge from the correlation between the molecular architecture (Chapter 2) and the mechanical and rheological properties (Chapter 3) of the model polymers is of the utmost importance for the fiber spinning process. The fiber spinning setup used in this chapter was a capillary rheometer equipped with a Haul-off system. Well defined linear and comb samples were investigated under melt spinning conditions. The second part of this chapter concentrates on melt spinning and melt flow instabilities. The target of this part was the design of a round sharkskin die for melt spinning that is equipped with force transducers to detect instabilities inside of a round die.

Chapter 5 focuses on the electrospinning process. Here, the effect of molecular architecture on the morphology of electrospun thin fibers was investigated. The model systems based on linear and comb polystyrene are used for electrospinning. In this chapter, the effect of chain branching on important electrospinning properties was examined in a controlled way employing model systems. The results show that the effect of chain branching on electrospinning can be explained using rheological parameters that show the interrelationships between chain branching, solution viscosity and the morphology of the electrospun fibers. The influence of the polystyrene architecture (comb versus linear) was quantified. The morphological transitions from beads to beads free fibers, fiber diameter and surface morphology of the fibers during electrospinning were investigated.

Within chapter 5 is followed by an investigation of extensional properties of the electrospinning solutions with the improved capillary break-up extensional rheometer (CaBER). The improvement of the original CaBER setup to include the measurement of the axial force made it possible to determine the separation energy of a polymer solution between two parallel plates. With these measurements, we were able to correlate the critical concentration for the beads to fiber transition in solution electrospinning with the separation energy of the polymer solutions.

## 2. Synthesis of model linear and comb homopolymers

## 2.1 Anionic polymerization

Anionic polymerization is a powerful method for the synthesis of polymers with well-defined and complex architectures [25-27]. The high reactivity of the anionic species with oxygen and proton donating impurities dictate special techniques and apparatus design to avoid premature termination of the living polymer chains [25, 28] (see Appendix A).

Anionic polymerization is classified as a living polymerization reaction. Other type of living polymerization techniques are: living cationic polymerization [29, 30], living ring opening metathesis polymerization [31] and living radical polymerization [32]. The term living is used to described reactions in which the polymer active centers of a growing polymer chain retain their reactivity and are able to continue the propagation of the polymerization without termination or transfer reactions [33]. If additional monomer is added to these living polymers, it will add to the existing polymeric chains and increase their degree of polymerization until all monomer is consumed. High vacuum techniques were first used for anionic polymerization of vinyl monomers by Worsfold [34] and continued by Morton and Fetters [35, 36]. The basic principle of this technique is the use of either high vacuum ($10^{-5}$-$10^{-9}$ bar) or inert gas atmosphere (mostly argon or nitrogen) in glass apparatus for the removal of impurities, that can react with the growing macroanions [25].

## 2.2 General aspects of anionic polymerization

The concept of anionic polymerization of diene monomers with sodium metal was first developed by Ziegler and Schlenk in 1910 and was the start of using alkali metal containing aromatic hydrocarbon complexes to initiate various $\alpha$-olefins [33].
In 1956 Szwarc et al. reported the mechanism of the anionic polymerization of polystyrene in tetrahydrofurane (THF) with sodium naphtalenide as an initiator [37, 38]. Their work was the beginning of research activities and technologies of anionic polymerization. The later works on the anionic polymerization of styrene and dienes in hydrocarbons were based on alkyllithium initiators [39-41].

Anionic polymerization is a chain polymerization [42]. The active centers in this type of polymerization are anions in the form of free ions, paired ions or aggregate species. The initiation has to be rapid and quantitative. The polymerization kinetics are controlled by the propagation step. The molecular weight of the polymer can be controlled by the ratio of monomer and initiator. In the case of no termination reactions, the growth of a fixed number of living chains leads to a narrow Poisson molecular weight distribution (see Appendix B) described by the dispersity $Đ = M_W/M_n$ [36, 43, 44], with the number average molecular weight $M_n = (\sum n_i M_i)/n_i$ and the weight average molecular weight $M_w = (\sum n_i M_i^2)/(\sum n_i M_i)$ of the polymer. The term "narrow molecular weight distribution" is reserved for $Đ < 1.1$ [33, 45].

The chemistry of anionic polymerization of vinyl monomers is based on the fundamentals of carbanion chemistry. Carbanions are defined as the carbon atoms that carry a negative charge. Carbanions are the conjugate base of a hydrocarbon and they are derived from organic molecules by heterolytic fission of a carbon-hydrogen bond [46, 47]. The carbanions are associated with counterions, typically an alkali metal cation. These compounds form aggregates in the solid state. In solutions the degree of association is influenced by the nature of the solvent, the counterion, the solution concentration, and the temperature [28]. The stability and reactivity of a carbanionic species can be deduced from their corresponding $pK_a$ values. The conjugated acids with lower $pK_a$ values (more acidic) form more stable carbanionic species compared to conjugated acids with higher $pK_a$ values.

The polymerization is highly demanding in terms of solvent and monomer purity. It must be completely free from protic impurities such as water, halogenated solvents and other impurities that can react with the growing polymer chain, such as oxygen and carbon dioxide (see Figure 2.5).

### 2.2.1 Monomers

Two groups of monomers can be polymerized by anionic polymerizations. The monomers of the first group have to contain electron accepting groups like vinyl, diene and carbonyl type found in monomers containing one or more double bonds (Figure 2.1). The monomers of the second group are heterocyclic monomers, which can be opened by reaction with nucleophiels [42]. In the case of vinyl monomers, ($H_2C=CHX$), the X group needs to have an electron withdrawing character to stabilize

11

the resulting carbanion, either inductively or through resonance (e.g. Figure 2.3). Monomers that undergo living anionic polymerization include hydrocarbon monomers such as styrene and styrene derivatives (e.g. $\alpha$-methylstyrene, tert-butylstyrene, etc.), dienes (e.g. isoprene, butadiene, etc.), polar vinyl monomers such as 2- and 4-vinylpyridine, (meth)acrylates, vinyl ketones, acrylonitriles and cyclic monomers like epoxides , lactones and siloxanes. Generally, monomers containing acidic protons or strongly electrophilic functional groups, which can react with initiators or macroanions, must not be present or must be protected.
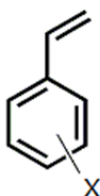
**Vinyl monomers:**

- **Ethylene [48, 49], vinylsilanes [50], acrylonitriles [51], vinyl aldehyds [52] and vinyl ketones [53]**
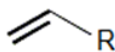


R: **H, Si(CH$_3$)$_3$, CN, COH and COCH$_3$**

- **Vinyl substituted aromatic compounds [54-63]**



X: **H, CH3, C(CH$_3$)$_3$, OCH$_3$, N(CH$_3$)$_2$, Cl and Br**
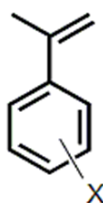


X: **H, 2,4,6-(CH$_3$)$_3$ and 4-Si(CH$_3$)$_3$**

- **Vinylpyridines [64-68]**
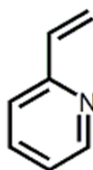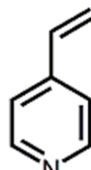


**2-Vinylpyridine      4-Vinylpyridine**

- **Alkyl methacrylates and acrylates [69-72]**



R: **alkyl group**

- **Conjugated dienes [73-76]**



Figure 2.1: Anionically polymerizable vinyl monomers.

## 2.2.2 Initiation

The monomer reacts with a strong base, which should have similar or slightly higher reactivity than the propagating macroanions. Too reactive initiators lead to side reactions between the initiator and monomer. If the reactivity is too little, the initiation is too slow or inefficient.
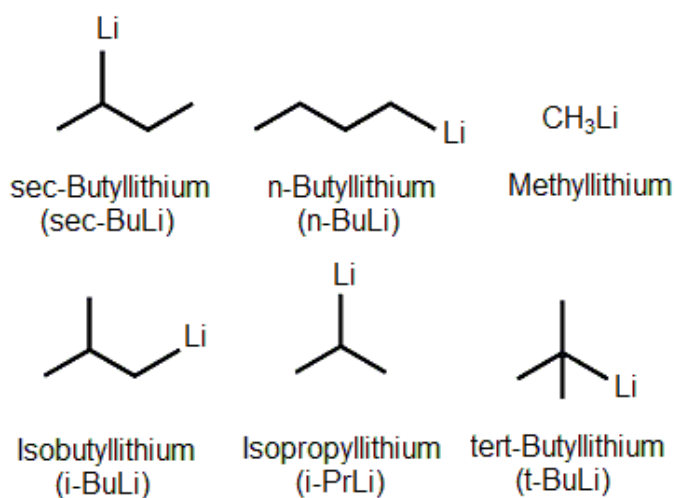


Figure 2.2: Alkyllithium compounds for the polymerization of styrene [42].

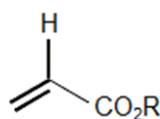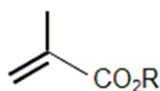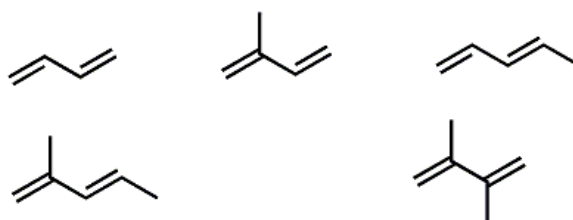A wide variety of initiating systems are used for anionic polymerizations, but alkyllithium compounds (Figure 2.2), especially the isomers of butyllithium (BuLi), are the most used and commercially available of this group. The carbon-Li bonds in these compounds include some covalent character and thus is called semi polar bond [77, 78]. Their reactivity is directly connected with their degree of association, means the higher the degree of association, the lower the reactivity of the initiators. For the polymerization of styrene the relative reactivity of the initiators linked to their average degree of associations (the number in parentheses) in hydrocarbon solution is shown below [79].

Methyllithium (2) > sec-BuLi (4) > i-PrLi (4-6) > i-BuLi > n-BuLi (6) > t-BuLi (4)

The reactivity of carbanion depends additionally on the solvent polarity. For the acceleration of the initiation step, addition of small amounts of Lewis bases such as ethers (e.g. THF) can be used. These Lewis bases decrease the degree of aggregation of the initiator and therefore accelerate rates of initiation. Some chain transfer reactions can occur especially at elevated temperatures and in presence of

Lewis bases. The importance of these reactions can be minimized by conducting anionic polymerization reactions at low temperature (e.g. -60 to -80 °C).

The initiation step for a well-controlled anionic polymerization is fast; therefore the kinetics of the polymerization is predominantly controlled by the propagation step. Figure 2.3 illustrates the initiation of styrene with the commercially available sec-BuLi, which is generally used in this study for the Initiation of monomers due to its reactivity.

$$I^- + M \xrightarrow{k_i} I - M^-$$
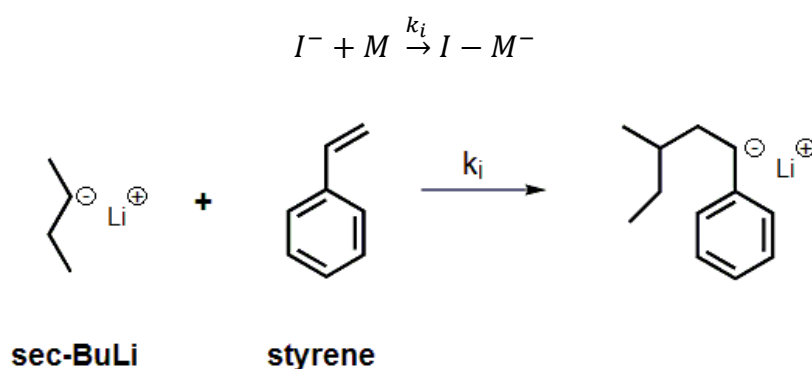


**sec-BuLi**          **styrene**

Figure 2.3: Initiation reaction of an anionic synthesis at the example of styrene with sec-BuLi. (I: Initiator, M: Monomer and $k_i$: Initiation rate constant)

### 2.2.3  Propagation

In the propagation step, the monomer molecules add to the reactive intermediates consecutively to produce an ever lengthening polymer chain. This step occurs with complete consumption of monomer to form living macroanions (Figure 2.4). After complete conversion of the monomers, the polymerization can be continued by the addition of further monomers. The initiation of styrene with sec-BuLi is very fast in comparison to the propagation step, thus even polymers with low molecular weights (10 – 15 kg/mol) can be prepared with a narrow molecular weight distributions ($Đ = \frac{M_w}{M_n} < 1.1$) [79].

$$I - M_i^- + M \xrightarrow{k_p} I - M_{i+1}^-$$
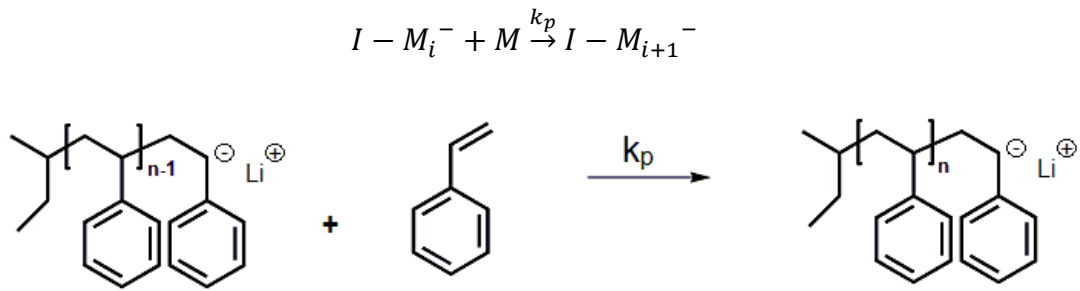


Figure 2.4: Propagation step for anionic polymerization using the example of polystyrene. ($k_p$: propagtion rate constant)

The following general rate equation would be applicable for anionic polymerization of all styrene and diene monomers that exhibit a pseudo first order kinetic dependence on monomer concentration:

$$[I]_0 = \sum_i [I - M_i^-] = const.$$

$$R_p = -\frac{d[M]}{dt} = k_p[M][I]_0$$

where $R_p$ is the rate of propagation, $[M]$ is the monomer concentration, $k_p$ is the polymerization rate constant, and $[I]_0$ is the initiator concentration, which is identical to the concentration of the propagating species in the case that no termination or transfer reaction occur.

The degree of polymerization $P_n$ can be calculated by following equation after all monomers have been consumed:

$$P_n = \frac{[M]}{[I]_0} \qquad (2.1)$$

In a living polymerization, all the polymer chains propagate at the same rate, leading to a narrow distribution of chain lengths, characterized by a Poisson distribution (see Appendix B for more detailed explanation) [79]. The final relationship between the dispersity and the degree of polymerization is:

$$Đ = \frac{M_w}{M_n} = 1 + \frac{P_n}{(1+P_n)^2} \approx 1 + \frac{1}{P_n} \qquad (2.2)$$

16

for $P_n \gg 1$. In this study the experimentally Đ values for anionically synthesized polystyrene samples as determined by size exclusion chromatography (SEC) are in the range of 1.02–1.19.

## 2.2.4 Termination

The anionic polymerization is conducted in the absence of reagents, which react with the anion of growing polymer chains. Traces of impurities like oxygen, carbon dioxide or protic agents (e.g. water or methanol) lead to the termination of macroanions (see Figure 2.5).
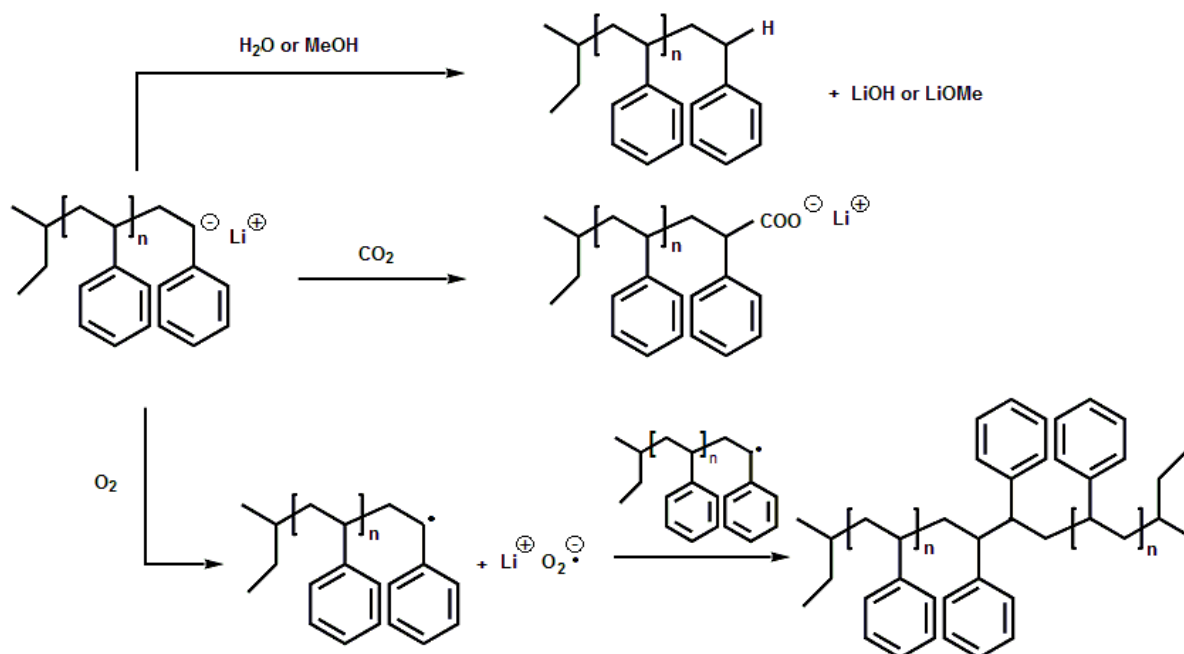


Figure 2.5: Termination reactions of the polystyrene macroanion with protic agents, carbon dioxide or oxygen.

After complete conversion of the monomers an addition of a small amount of degassed methanol is needed to obtain the final product. The termination with oxygen from the atmosphere or dissolved in methanol leads to polymer chains with double molecular weight, which can sometimes be observed as an unwanted side reaction in SEC measurements.

### 2.2.5 Solvents and solvent effects

The range of solvents in anionic polymerization is limited due to high reactivity of the initiators and the propagating carbanionic chain ends. For styrene and diene monomers, the solvents of choice are alkanes and cycloalkanes, aromatic hydrocarbons, and ethers. The relative initiation and propagation rates under equivalent conditions are faster in aromatic versus aliphatic non-polar solvents. However, chain transfer reactions can occur with alkylated aromatic solvents (e.g. toluene). In case of an aromatic non-polar solvent, t-butylbenzene is a good alternative. The solvent t-butylbenzene has no reactive benzylic hydrogens and has a freezing point of -58.1 °C, which makes it interesting for low temperature polymerization reactions. A wider range of solvents can be used for less reactive anionic chain ends (e.g. heterocyclic monomers). For example, dipolar aprotic solvents (e.g. dimethylsulfoxide, N,N-dimethylformamide and hexamethylphosphoramide) can be used for anionic polymerization of epoxies [76].

Typical kinetics of the initiation reaction of sec-BuLi with styrene in benzene exhibits a first-order dependence on the styrene concentration and approximately a one-forth-order dependence on the initiator concentration, since sec-BuLi is aggregated into tetramers. The experimentally observed one-half reaction order dependence on the poly(styryl)lithium concentration for the propagation step is consistent with the hypothesis that the macro anions exist as dimers in hydrocarbon solutions. These aggregations have been observed light scattering, and neutron scattering methods [76].

The rate of anionic polymerization of styrene with alkyllithium initiators is very fast in polar solvents (e.g. THF), because the solvent coordinates with the counterions. This leads to a breakup of the aggregations and thus leads to a higher initiation and propagation rate. Some chain transfer reactions can occur especially at elevated temperatures. These reactions can be minimized by working at low temperatures (e.g. -78 °C for acetone and dry ice mixture).

## 2.2.6 Synthesis strategy for combs

The synthesis methods for polystyrene comb polymers have been reported in several review articles [76, 79-84]. Generally, these methods are divided into three major categories: "grafting through", "grafting from" and "grafting onto", as outlined in Figure 2.6.

In "grafting from" the synthesis starts with the preparation of a backbone polymer (macroinitiator). The number of side chains can be theoretically controlled by the number of active centers (I) along the backbone. In next step grafting of macroinitiator followed by the addition of a monomer. The side chains grow away from the backbone by polymerization of monomers initiated from each active center.

The "grafting through", also called macromonomer method, involves the copolymerization of macromonomers with a comonomer to produce the graft copolymer. The macromonomer is a functional polymer with a polymerizable group at one chain end. Living polymerization is the ideal method to prepare well-defined macromonomers, which can be completely characterized prior to polymerization. The comonomer units dilute the density of the macromonomer units along the backbone, and can generally control the number of branches in grafted polymer.
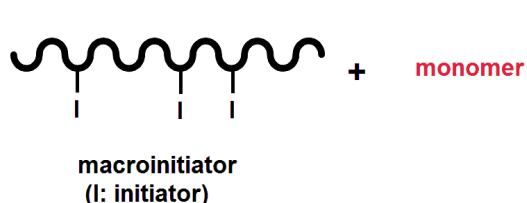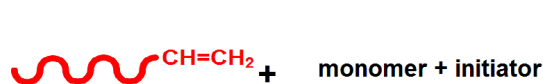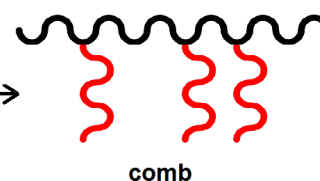


Figure 2.6: Three major strategies to construct comb polymers: a) grafting from, b) grafting through and c) grafting onto.

Compared to the "grafting from" strategy, the "grafting through" strategy has more control upon the grafting density and the length of the side arms. In the "grafting from" approch, information about the length and the number of side chains cannot be easily obtained. Hadjichristidis et al. [85, 86] synthesized styryl-functionalized polybutadiene by slow addition of living polymer chains to 4-(chlorodimethylsilyl)styrene (CDMSS), as shown in figure 2.7. The substitution reaction between the macroanion and CDMSS is more selective for silyl chloride than for the styrenic double bond.
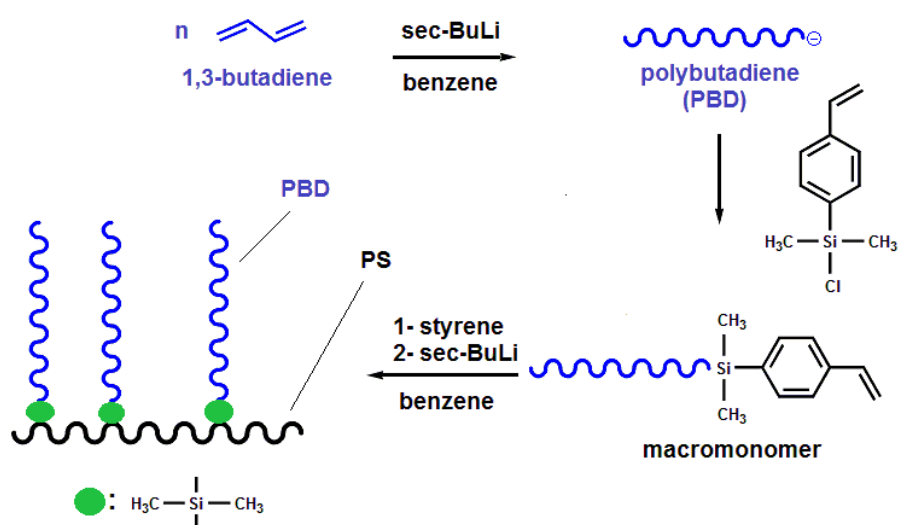


Figure 2.7: Preparation and copolymerization of macromonomer (grafting through) [25, 85, 86].

In the "grafting onto" strategy, which is the method of comb synthesis in this study, the backbone and side chains are synthesized independently. Thus prior to coupling reactions, both can be fully characterized. The backbone has statistically distributed functional groups X and the side chains have the end-functional groups Y (see Figure 2.6 c). The grafting is carried out via a coupling reaction between the functional groups X of the backbone and the end-functional groups Y of side chains. This method involves a nucleophilic attack of the living polymer side arms at the electrophilic sites (e.g. benzylic halides, anhydrides, and esters) of the backbone. A full occupation of all the reactive sites on the backbone can hardly be achieved by the "grafting onto" strategy [87]. With increasing grafting density, the diffusion of unreacted side arms to the reactive sites on the backbone slows down, because of an increasing steric hindrance. Additionally the attachment of side arms to the

backbone at a high grafting density becomes entropically unfavorable; because the grafted polymer must change from a random coil to a more stretched conformation once it is attached to the backbone.

Typically, the side chains are added in excess in order to achieve a relatively high conversion. However, the separation of the grafting product from unreacted side chains may become problematic.

## 2.3 Synthesis and characterization of polystyrene combs

### 2.3.1 Reaction overview and molecular characterization

The grafting onto is the method of choice for the synthesis of model comb polystyrene in this study. As shown in Figure 2.6 c, for the grafting onto strategy both backbone and side chains are prepared separately, which means a full characterization of the two polymers is possible. The final carbonyl functionalities are utilized due to the reaction with nucleophilic compounds, e.g. Grignard reagents and other reactive anions. The reaction steps for model PS combs are shown in Figure 2.9. The grafting of side chains onto the backbone via coupling reaction between pendant carbonyl groups along the backbone and the nucleophilic living side chains is our synthesis strategy, which was used earlier by Li et al. and Kempf et al. [88-90]. The backbone was synthesized by anionic polymerization of styrene. A small number of acetyl groups (< 4 mol%) were introduced in the PS backbone via Friedel-Crafts acylation (see Figure 2.8). Either an acyl halid or an acid anhydride can be used for acylation reaction.
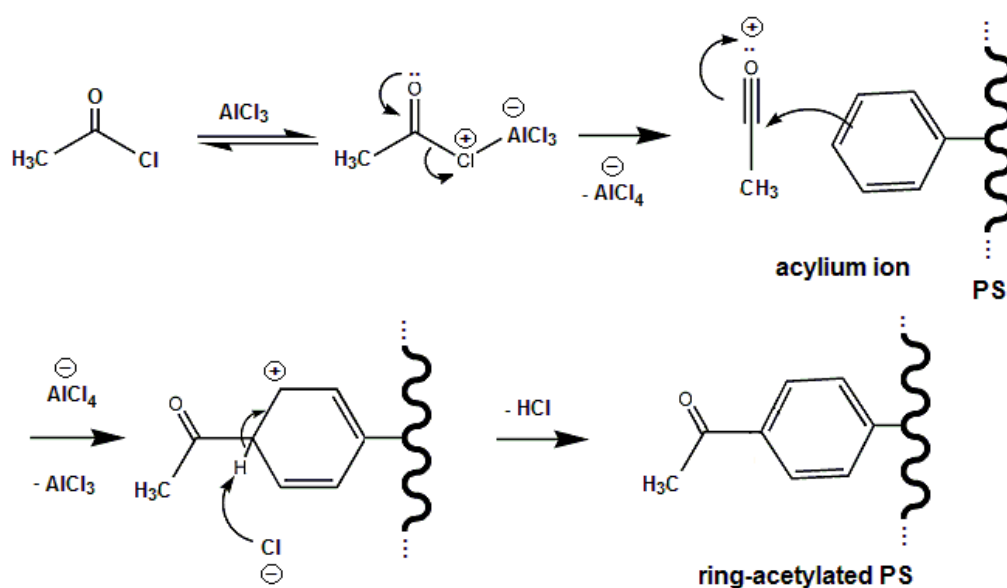


Figure 2.8: Ring acetylation of the PS backbone via a Friedel-Crafts reaction.

Because the product of a Friedel-Crafts acylation reaction contains a carbonyl group, that can complex with AlCl$_3$, the Friedel-Crafts acylation must be conducted with more than one equivalent of AlCl$_3$ [46, 91]. The reaction leads to a strong decrease of electron density at the benzyl ring, which prevents further acetylation [92]. The acetylation of the aromatic ring of the backbone can occur only in para position due to steric hindrance of the polymer backbone and the bulky acetylating complex [90]. PS side chains were synthesized separately via anionic polymerization. The coupling reaction takes place via nucleophilic attack of the living side chains to the carbonyl groups of the backbone.
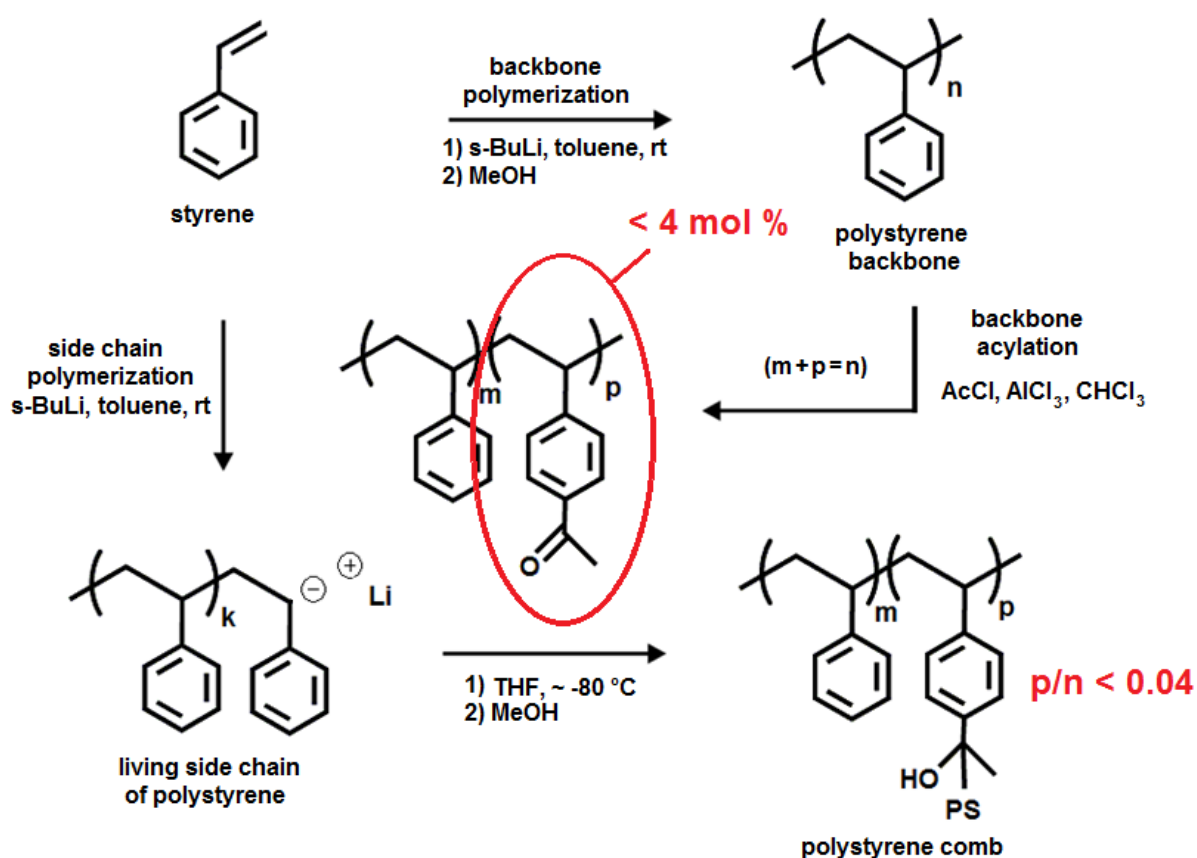


Figure 2.9: Synthetic scheme for the model PS combs. PS backbone(s) and side chains were separately synthesized via anionic polymerization. The grafting reaction at the carbonyl group of the partially acetylated backbone occurs via nucleophilic attack of the living side chains [88, 93].

The side chains are added in excess to the backbone (50 mol %) in order to achieve high conversion of the carbonyl groups located at the polymer backbone. The residual living side chains are protonated at the end of the reaction by the addition of

methanol. Unreacted side chains were separated from the PS combs by repeated precipitation/fractionation in a THF/methanol mixture.

The amount of THF/methanol is different for different combs. The polymer mixture (~ 100 g) was dissolved in about one liter of THF. Methanol was added dropwise to the solution until the first polymer with higher molecular weight (comb) started to precipitate. The precipitated polymer separated from solution. The precipitation/fractionation was repeated 4-5 times and each time, the product was controlled via SEC to verify the purification of comb polymer. The peak related to the side chains was weaker each time and at least disappeared from the SEC diagram.

The molecular characteristics of the model combs are described in Table 2.1. To ensure each synthesis step was performed correctly, the polymer backbone and side chains were separately characterized before they were bonded together. Four different PS combs were synthesized using the same polymer backbone and therefore all combs had a constant backbone molecular weight, $M_{n,bb} \approx 90$ kg/mol. In addition, the total molecular weight of the segments in the side chains was nearly identical for all combs, $N_{br} \cdot M_{n,sc} \approx 160$ kg/mol, where $N_{br}$ and $M_{n,sc}$ denote the average number of grafted branches per molecule of the backbone and the number average molar mass of the grafted chains, respectively. The number average mass fraction of the grafted side chains $\phi_{br}$ is given by:

$$\phi_{br} = \frac{N_{br} \cdot M_{n,sc}}{M_{n,bb} + N_{br} \cdot M_{n,sc}} = 1 - \frac{M_{n,bb}}{M_{n,comb}} \approx \frac{2}{3} \qquad (2.3)$$

where $M_{n,comb}$ is the number average molar mass of the grafted polymer [94]. Values for $\phi_{br}$ for all combs were between 0.61 and 0.65 (see Table 2.1). While the value for $\phi_{br}$ was nearly constant, each comb had a different number of side chains depending on the side chain length. The following nomenclature is used for the polystyrene combs: PS X-Y-Z, where X = $M_{n,bb}$ in kg/mol, Y = $N_{br}$ and Z = $M_{n,sc}$ in kg/mol (see Figure 2.10).

The characterization of branched polymers has been investigated by Zimm and Stockmayer [95, 96]. Their method is based by the fact that branching decreases the radius of gyration $R_g$ of a polymer chain in comparison to $R_g$ of a linear chain of the same molar mass. This contraction usually is expressed by the contraction factor $g$ and can be calculated as follows:

$$g = \left.\langle R_g^2 \rangle_{br} \middle/ \langle R_g^2 \rangle_l \right. \qquad (2.4)$$

where $\langle R_g^2 \rangle_{br}$ and $\langle R_g^2 \rangle_l$ are the mean squared radius of gyration of the branched and linear polymer at the same molar mass. For branched polymers, the parameter $g$ is always less than 1. Similarly, the decrease in the intrinsic viscosity (In dilute-solution of polymers, the limit of the ratio of specific viscosity to the concentration as the concentration approaches zero) of a branched molecule can be used to quantify the extent of branching. This is done using the contraction factor $g'$, which is defined as the ratio of the intrinsic viscosities of the branched polymer $[\eta]_{br}$ to that of a linear polymer $[\eta]_l$ with the same molar mass.

$$g' = \left. [\eta]_{br} \middle/ [\eta]_l \right. \qquad (2.5)$$

Table 2.1: Molecular characteristics of the synthesized linear and comb polymers.

| Sample | $^1M_{n,bb}$ [kg/mol] | $^1Đ_{bb}$ | $^1M_{n,sc}$ [kg/mol] | $^1Đ_{sc}$ | $^2N_{br}$ | $^3M_{n,comb}$ [kg/mol] | $^3M_{w,comb}$ [kg/mol] | $\phi_{br}$ | $g'$ |
|---|---|---|---|---|---|---|---|---|---|
| Comb PS | | | | | | | | | |
| PS90-32-5 | 90 | 1.05 | 5 | 1.15 | 31.7 | 249 | 287 | 0.65 | 0.29 |
| PS90-13-12 | 90 | 1.05 | 12 | 1.03 | 13.4 | 249 | 254 | 0.64 | 0.46 |
| PS90-5-30 | 90 | 1.05 | 30 | 1.03 | 4.6 | 248 | 253 | 0.61 | 0.59 |
| PS90-4-42 | 90 | 1.05 | 42 | 1.02 | 3.8 | 244 | 251 | 0.64 | 0.61 |
| Linear PS | | | | | | | | | |
| PS90 | $^1M_n$ = 90 kg/mol, $M_w$ = 95 kg/mol, $Đ$ = 1.05 | | | | | 97 | | 0 | 1.04 |
| PS207 | $^1M_n$ = 207 kg/mol, $M_w$ = 232 kg/mol, $Đ$ = 1.12 | | | | | - | | 0 | - |
| PS265 | $^1M_n$ = 265 kg/mol, $M_w$ = 292 kg/mol, $Đ$ = 1.10 | | | | | 297 | | 0 | 0.99 |
| PS344 | $^1M_n$ = 341 kg/mol, $M_w$ = 382 kg/mol, $Đ$ = 1.12 | | | | | - | | 0 | - |
| PS475 | $^1M_n$ = 455 kg/mol, $M_w$ = 542 kg/mol, $Đ$ = 1.19 | | | | | - | | 0 | - |

1: Determined via SEC, 2: determined via 400 MHz $^1$H-NMR, 3: determined via SEC-MALLS, $bb$ = backbone, $sc$ = side chain, $N_{br}$ = average number of branching per backbone, $\phi_{br}$ = number average mass fraction of side chain and $g'$ = contraction factor.
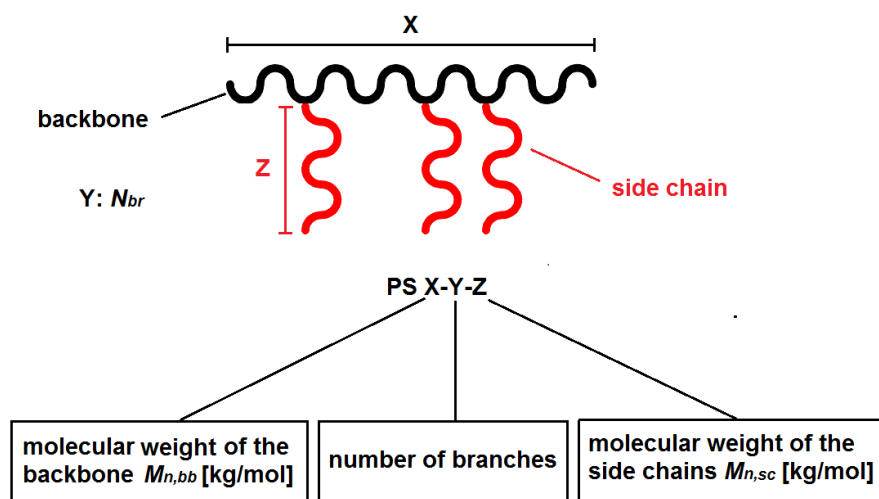
Figure 2.10: The nomenclature used for the polystyrene combs in this study.

Theoretical and experimental studies have shown, that the contraction factors $g$ and $g'$ are related via a scaling law as follows [95, 97]:

$$g' = g^b$$

where b is the solvent factor. Zimm predicted a value of b = 0.5 for star-shaped polymers, which has empirically values between 0.5 and 1.5 [95, 97]. There is a strong variation of b, depending on the chemical structure and molar mass for randomly branched polymers.

The number of branches connected to the PS backbone is well controlled by the acetylation of the backbone and was varied between 0.4-4 mol % acetylated monomer per backbone chain. The degree of acetylation (number of branching points) was quantified during the synthesis by 400 MHz ^{1}H-NMR, even for low amounts of functional groups *e.g.* 1024 scans for ^{1}H-NMR (see Figure 2.11). The ortho protons adjacent to the carbonyl group shift to a lower field (7.5 ppm < $\delta$ < 7.6 ppm) compared to the five aromatic protons located between 6 and 7.5 ppm for nonacetylated PS. For example, the calculated ratio of peak integrals (88:1) of the five aromatic protons to the $CH_3$ protons adjacent to the carbonyl group at $\delta$ = 2.45 ppm for functionalized PS (Figure 2.11b) resulted in a measurement of sixteen groups per backbone on average. As shown in Figure 2.11c, the ratio between these peak integrals was (1508:1) after the grafting reaction, which indicates that the conjunction of backbone and side arms did not proceed quantitatively. This

may be due to competition between the coupling reaction and termination of the macroanion, which can occur when the living PS attacks the acetyl functionality leading to enolate formation (see Figure 2.12) because the protic methyl group is adjacent to the carbonyl group [89]. It was found via ^{1}H-NMR spectroscopy, for the synthesis of PS90-13-12, that on average three carbonyl groups of the sixteen side arms per backbone did not react, resulting in a backbone with thirteen side arms.
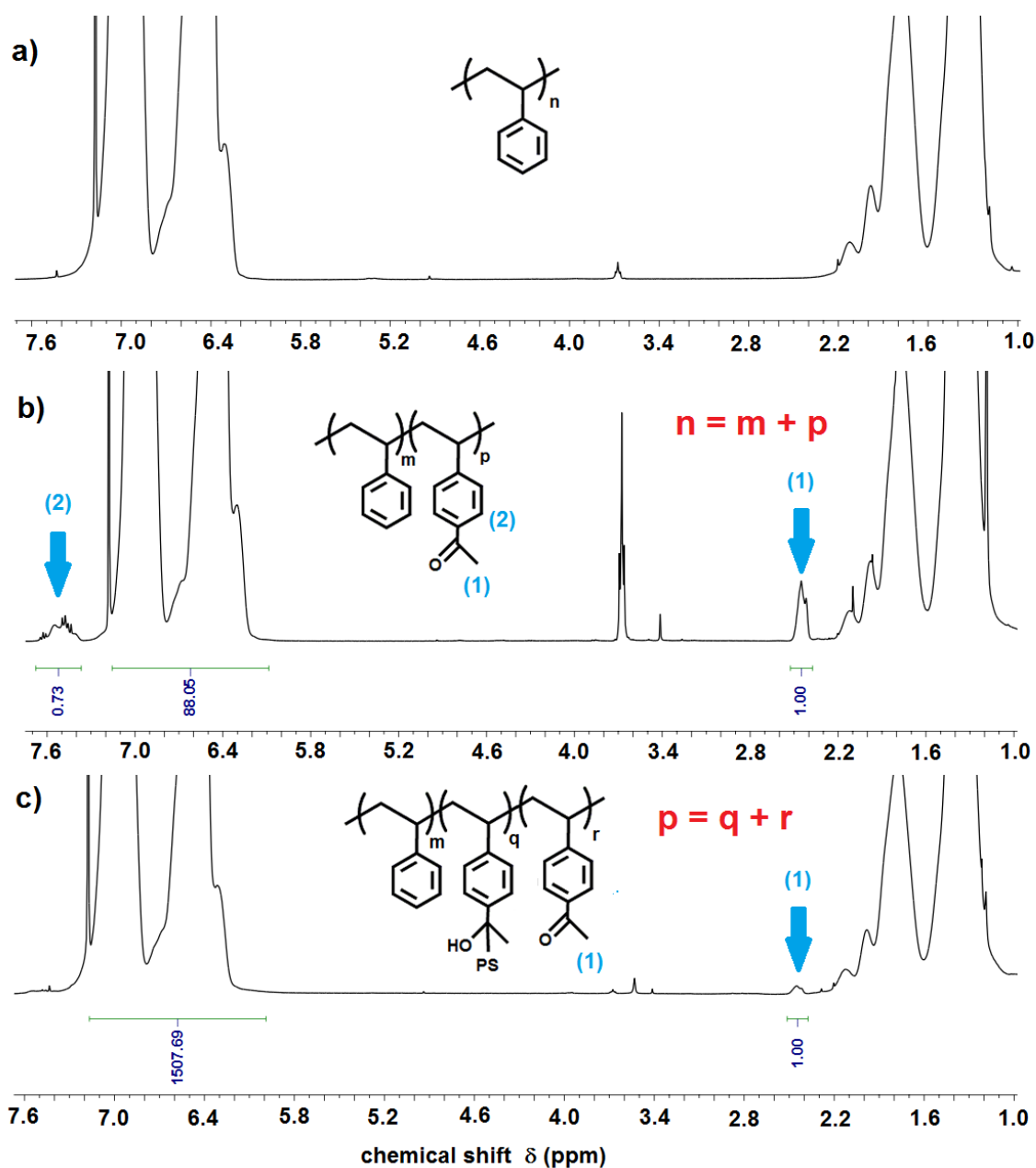


Figure 2.11: ^{1}H-NMR spectrum of a) PS90, b) partially ring-acetylated PS90 with an average number of functional groups per main chain of 16 and c) the coupling product PS90-13-12, all measured in CDCl$_3$ at 400 MHz with 1024 scans.

The molecular characterization of the final product (PS combs) was carried out by SEC-MALLS to give the absolute molecular weight of the combs. The $[\eta]_l$ and $[\eta]_{br}$ values were determined from a MALLS detector and a viscosity detector, respectively, that were coupled with an SEC column. The value of $[\eta]_{br}$ was measured directly using the viscosity detector, and $[\eta]_l$ was calculated using the Mark-Houwink-Kuhn-Sakurada (MHKS) relation, $[\eta]_l = KM_w^\alpha$ [98]. The MHKS parameters were determined via SEC for this investigation with 10 linear PS calibration standards ranging from $M_n$ = 50 kg/mol up to $M_n$ = 500 kg/mol in THF at 25 °C. They were determined to be K = 16.9x10$^{-5}$ dL/g and $\alpha$ = 0.76, respectively, and are in line with the literature values [98] (literature: K = 14.1x10$^{-5}$ dL/g and $\alpha$ = 0.70 at 25 °C).
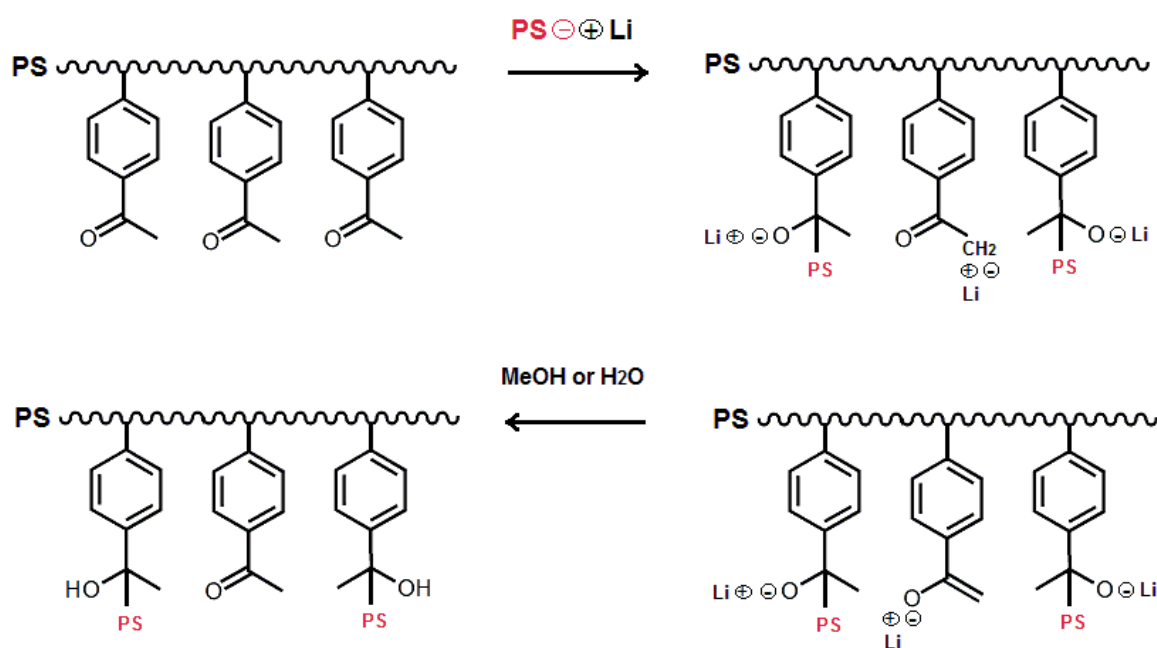


Figure 2.12: Grafting and competing enolate formation reaction [89].

The molar mass distribution of the various stages of the synthesis for comb PS90-13-12 are shown in Figure 2.13 where the side chain and backbone with $N_{br}$ = 13 were first separately synthesized before grafting to form the comb PS90-13-12. The comb is unimodal and has a narrow molecular-weight distribution (Đ = 1.02).
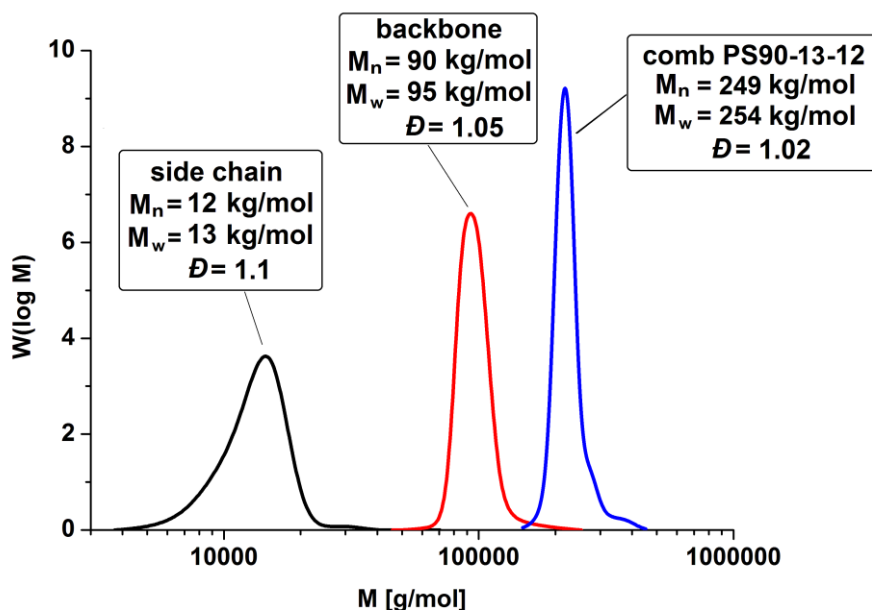
Figure 2.13: The molar mass distribution of the comb PS90-13-12, with $M_n$(backbone) = 90 kg/mol, $M_n$(side chain) = 12 kg/mol and number of branches per main chain $N_{br}$ = 13. Absolute $M_w$ of PS90-13-12 was determined via SEC-MALLS (THF, 25 °C).

With respect to the SEC-MALLS results, the weight average molecular weights measured for all the combs were similar with values near 250 kg/mol. The calculation of expected number averaged molar mass $M_n$ of the combs based on the $N_{br}$ determined by ^{1}H-NMR are in agreement with SEC-MALLS results. As the calculation was based on the SEC determined values for the $M_n$ of the linear backbone and the side chain and these values are accurate within 10-15 %, the deviation between the SEC-MALLS and NMR values is within the limit of reproducibility of those two methods.

The comparison of the g'-factor from the different PS combs in Table 2.1 shows that increasing the value of $N_{br}$, while keeping the total number of segments in the branches constant in all samples, decreases the g'-factor from ~ 0.6 for PS90-5-30 and PS90-4-42 to 0.46 for PS90-13-12 and 0.29 for PS90-32-5. This demonstrates that a comb PS with a higher number of branches is more compact and has a smaller radius of gyration than a comb PS with a low number of branches. The comparison of g' for PS90-4-42 and PS90-5-30 shows that when the number of branches is similar for two samples, the length of the branches does not have a large effect on the resulting radius of gyration of the two samples in solution (see Table 2.1).

### 2.3.2 Precipitation fractionation

Precipitation fractionation was used to remove non reacted polystyrene side chains from the comb polymer. The principle of the precipitation fractionation depends on the phase separation governed by a stepwise decrease in the solvent power of the system. The solvent power is conveniently expressed in terms of the polymer-solvent interaction coefficient $\chi$. A solvent for a given polymer should have a $\chi$ value below 0.5, whereas a liquid having a $\chi$ value over 0.5 belongs to the category of nonsolvents [99]. This coefficient depends on [100, 101] the types of solute and solvent and on temperature, but not on the concentration, nor considerable on the molecular weight of the polymer, provided it is high. In general, the precipitation fractionation can be implemented by three methods; addition of nonsolvent (precipitant), elimination of solvent by evaporation and decreasing the temperature of the system. In our study, we used the addition of a poor solvent to perform fractional precipitation. The general procedure of this method is described by Kotera [99]. The equipment for fractional precipitation is shown in Figure 2.14. The polymer is dissolved in a suitable solvent (e.g. THF for polystyrene) and an appropriate nonsolvent (e.g. methanol). The solution has to proceed with permanent agitation to prevent a precipitation gradient. After careful addition of a certain amount of precipitant (1-2 drops per second), addition of more drops causes turbidity, which is not disappearing quickly during stirring. At this point, the slow addition of nonsolvent is continued until the solution turns milky. Then the solution is allowed to phase separate for several days. The precipitated phase, which contains the fractionation of polymer with the highest molecular weight (e.g. comb polymer), can be easily collected and separated from the fractionation containing polymer with the lower molecular weight (e.g. not reacted side chains). This procedure is repeated several times. A successful fractionation can be confirmed by SEC of the fractionated and non-fractionated sample.
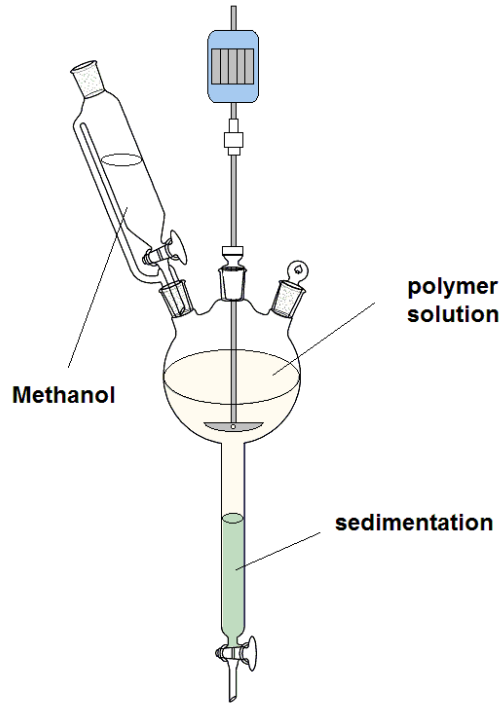
Figure 2.14: The experimental setup of fractional precipitation.

The Flory-Huggins equation can be expressed as follows [42, 99, 102]:

$$\frac{\Delta\mu_s}{RT} = ln\left(1 - \varphi_p\right) + \left(1 - \frac{1}{P_n}\right)\varphi_p + \chi\varphi_p^2 \qquad (2.6)$$

where $\Delta\mu_s$ is the change of chemical potential of the solvent in solution, $\varphi_p$ is the volume fraction of the dissolved polymer having a degree of polymerization of $P_n$ , R and T are the gas constant and the temperature, respectively [79, 99, 103]. For a polymer to be soluble $\Delta\mu_s \leq 0$. The critical value of the Flory-Huggins parameter $\chi_{crit}$ depends on the molecular weight of the dissolved polymer [99]:

$$\chi_{crit} = \frac{1}{2}\left(1 + \frac{1}{\sqrt{P_n}}\right)^2 \cong \frac{1}{2} + \frac{1}{\sqrt{P_n}};\ P_n \gg 1 \qquad (2.7)$$

which results in $\chi_{crit}$ = 0.5 for $P_n \gg 1$. A stepwise addition of nonsolvent increases the $\chi$ value of the system to exceed the $\chi_{crit}$ for each component, which means, the component with higher molecular weight starts to precipitate first from the polymer solution.

## 2.4 Conclusion

Five linear topologies and four model comb polymers were synthesized via anionic polymerization and characterized with $^1$H-NMR and SEC-MALLS in this chapter. The polymer combs consist of well-defined backbone and side chain lengths, low dispersities ($Đ < 1.1$) and a small amount of branches (ca. $4 - 32$ branches per backbone). These four combs were made with the same backbone ($M_{n,bb} \approx 90$ kg/mol) and had a nearly constant total number of monomer segments in the side chains ($M_{n,comb} \approx 250$ kg/mol).

## 3. Rheological characterization

Rheology is the science of deformation and flow of matter [104, 105]. In this chapter a short description of the basic principles of shear and extensional rheology is given. More details in every section can be found in rhelogical textbooks [104-109].

### 3.1 Shear rheology

Steady simple shear of a liquid is accomplished by confining the liquid between two parallel plates (Figure 3.1) [105, 108]. The upper plate moves at a constant velocity v and the lower plate is at rest. The velocity in the liquid is in the direction of $x_1$ and changes linearly in the $x_2$ direction. The area of the top plate is A and the force needed to move the upper plate is denoted F. A maximum flow speed v is found at the upper boundary.
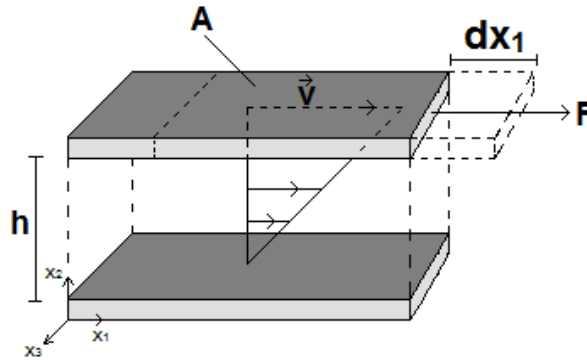


Figure 3.1: Two plate model for shear experiment. A fluid located between two parallel plates. The top plate with the (shear) area A is set in motion by the force F. The lower plate is stationary (v = 0). Between the plates there is the distance h.

The shear stress $\sigma_{21}$, strain $\gamma$ and shear rate $\dot{\gamma}$ can be defined as follows:

$$\sigma_{21} = \frac{F}{A} \qquad (3.1)$$

$$\gamma = \frac{dx_1}{h} \, ; \dot{\gamma} = \frac{1}{h} \cdot \frac{dx_1}{dt} = \frac{v}{h} \qquad (3.2)$$

A typical stress component is written as $\sigma_{ij}$. The first index indicates the type of surface on which the force acts and the second index indicates the direction in which it acts. The state of stress described by the stress tensor is given by:

$$\sigma_{ij} = \begin{bmatrix} \sigma_{11} & \sigma_{12} & 0 \\ \sigma_{21} & \sigma_{22} & 0 \\ 0 & 0 & \sigma_{33} \end{bmatrix} \qquad (3.3)$$

where the shear stresses are $\sigma_{12} = \sigma_{21}$ and $\sigma_{11}$, $\sigma_{22}$ and $\sigma_{33}$ are the normal stresses. There are two independent normal stress differences, called the first and second normal stress differences. These, along with the viscosity, are called the viscometric functions:

$$\eta(\dot{\gamma}) = \frac{\sigma_{21}}{\dot{\gamma}} \qquad (3.4)$$

$$N_1(\dot{\gamma}) = \sigma_{11} - \sigma_{22} \qquad (3.5)$$
$$N_2(\dot{\gamma}) = \sigma_{22} - \sigma_{33} \qquad (3.6)$$

The shear viscosity and $\eta$ the first and second normal stress differences $N_1$ and $N_2$ are functions of the shear rate $\dot{\gamma}$ and most of the rheological experiments measure quantities associated with them. Alternatively, both normal differences can be divided by the squared shear rate leading to the first and second normal stress coefficients:

$$\psi_1 = \frac{N_1}{\dot{\gamma}^2} \qquad (3.7)$$

$$\psi_2 = \frac{N_2}{\dot{\gamma}^2} \qquad (3.8)$$

There are several possible test geometries (see Figure 3.2) and deformations e.g. torsion between parallel plates, torsion between a cone and plate and rotation between two coaxial cylinders (Couette flow). The viscosity can be obtained from measurement of the angular velocity of the plate, cone or cylinder and the torque.

The main components of a rotational rheometer are the motor and the force measurement. There are two principles used in rotational rheometers [108, 110]. One operates at controlled angular or linear displacement, respective strain, and is used

in controlled strain rheometers. The other setup operates with a controlled torque or applied force, respective stress, on the sample, and is implemented in controlled stress rheometers.
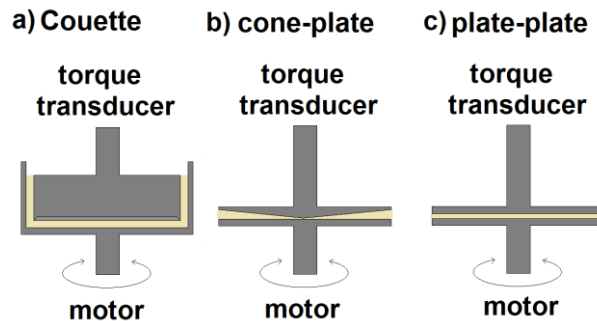


Figure 3.2: Various geometries in a controlled strain rheometer. a) concentric cylinders (Couette) for samples with very low to medium viscosities, b) cone and plate for samples with very low to high viscosities and c) parallel plates for samples with low viscosities up to soft solids.

Figure 3.2 shows the different geometries used in a controlled strain rheometer. The motor applies a defined deformation to the lower geometry and the mechanical response of the sample can be measured via a torque transducer connected to the upper geometry.

### 3.1.1  Phenomenological models

For a purely elastic material (spring) the relation between shear stress and strain is determined by Hooke's law:

$$\sigma_s = G \cdot \gamma \qquad (3.9)$$

where $G$ is the shear modulus and $\sigma_s$ is the shear stress in the spring. This law is restricted to small deformations. The spring element represents the ideal elastic behavior. For a purely viscous material, there is a linear dependence between the stress and the shear rate. For an ideal viscose material according to Newton's law:

$$\sigma_d = \eta \cdot \dot{\gamma} \qquad (3.10)$$

The Newtonian model is often represented using a dashpot ($\sigma_d$ is the shear stress in the dashpot). If a sinusoidal deformation with a constant angular frequency $\omega_1$ is applied to the sample, the resulting stress oscillates in phase with the same angular frequency for an ideal elastic element. For an ideal viscous element, hence the shear rate is the time derivative of the deformation, and the stress is shifted $\pi/2$ out of phase with respect to the strain wave:

$$\gamma(t) = \gamma_0 \sin(\omega_1 t) \qquad (3.11)$$

ideal elastic element:    $\sigma_s = G \cdot \gamma(t) = G \cdot \gamma_0 \sin(\omega_1 t)$    (3.12)

ideal viscous element:    $\sigma_d = \eta \cdot \dot\gamma = \eta\gamma_0\omega_1 \cos(\omega_1 t) = \eta\gamma_0\, \omega_1 \sin(\omega_1 t + \pi/2)$    (3.13)

Viscoelastic materials like polymers exhibit both viscous resistance to deformation and elasticity. As a first attempt to obtain a viscoelastic equation, a spring with a dashpot in series can be considered as seen in Figure 3.3. Such an element is called a Maxwell element.
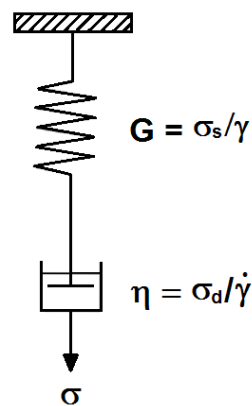


Figure 3.3: Scheme of the Maxwell model with an elastic spring and a viscous dashpot connected in series.

For the Maxwell model the stress is the same in both elements, but the deformation is equal to the sum of the individual deformations of the spring and dashpot. The stress and strain can be written as follows:

$$\frac{d\gamma}{dt} = \frac{d\gamma_s}{dt} + \frac{d\gamma_d}{dt} \qquad (3.14)$$

$$\frac{d\gamma}{dt} = \frac{1}{G_s} \cdot \left(\frac{d\sigma}{dt}\right) + \frac{\sigma}{\eta_d} \qquad (3.15)$$

Equation 3.15 is an ordinary differential equation and shows the relationship between stress and strain. At steady state ($d\sigma/dt \to 0$) the equation represents Newton's law of viscosity. In the case of a rapid motion at short times ($t \to 0$) the stress term can be neglected in favor of the time-derivative term, therefore Hooke's law for elastic solids is recovered.

In the case of constant deformation ($\frac{d\gamma}{dt} = 0$) the differential equation can be solved with the following function:

$$\sigma(t) = \sigma(0) \cdot \exp\left[-\frac{t}{\tau}\right] \qquad (3.16)$$

where $\tau = \frac{\eta_d}{G_s}$ is the relaxation time, $\sigma(0)$ and $\gamma(0)$ are the stress and deformation at $t = 0$, respectively.

If the sample deforms sinusoidally under harmonic stress $\sigma(t) = \sigma(0)\, e^{i\omega_1 t}$, this drives a harmonic strain of $\gamma(t) = \gamma(0)e^{i\omega_1(t+\delta)}$, where $\delta$ is the phase angle between the stress and the resulting strain, and the Maxwell equation can be written as follows:

$$\frac{d\gamma(t)}{dt} = i\omega_1\gamma(0)e^{i\omega_1(t+\delta)} = i\omega_1\gamma(t) \text{ and } \frac{d\sigma(t)}{dt} = i\omega_1\sigma(0)\, e^{i\omega_1 t} = \sigma(t)$$

$$i\omega_1\gamma(t) = \frac{1}{G_s} \cdot (i\omega_1\sigma(t)) + \frac{\sigma(t)}{\eta_d}$$

$$\sigma(t) = \frac{G_s\eta_d^2 i\omega_1}{G_s + i\omega_1\eta_d}\gamma(t) \Leftrightarrow \sigma(t) = \frac{G_s\eta_d^2\omega_1{}^2 + G_s{}^2 i\eta_d\omega_1}{G_s{}^2 + \omega_1{}^2\eta_d^2}\gamma(t)$$

$$\overset{\tau=\frac{\eta_d}{G_s}}{\Longleftrightarrow} \sigma(t) = G_s\frac{\tau^2\omega_1{}^2 + i\tau\omega_1}{1 + \tau^2\omega_1{}^2}\gamma(t) = G^* \cdot \gamma(t) \qquad (3.17)$$

where $G^*$ is the complex modulus. The real and imaginary part of $G^*$ can be written as follows:

$$G'(\omega_1) = G_s \frac{\tau^2 \omega_1^2}{1 + \tau^2 \omega_1^2} \text{ and } G''(\omega_1) = G_s \frac{\tau \omega_1}{1 + \tau^2 \omega_1^2} \qquad (3.18)$$

where $G'(\omega_1)$ and $G''(\omega_1)$ are called the storage and loss modulus, respectively. The relation between the viscoelastic moduli is called the loss factor:

$$\tan \delta = \frac{G''(\omega_1)}{G'(\omega_1)} \qquad (3.19)$$

The complex modulus and complex viscosity are related as follows:

$$\eta^* = \frac{G^*}{i \omega_1} \qquad (3.20)$$

This concept can be generalized with many Maxwell elements connected in parallel (see Figure 3.4), so the storage and loss moduli can be expressed in terms of the relaxation time spectrum $\tau_i$ and the frequency $\omega$ as follows:

$$G'(\omega_1) = \sum G_i \frac{\tau_i^2 \omega^2}{1 + \tau_i^2 \omega^2} \qquad (3.21)$$

$$G''(\omega_1) = \sum G_i \frac{\tau_i \omega}{1 + \tau_i^2 \omega^2} \qquad (3.22)$$



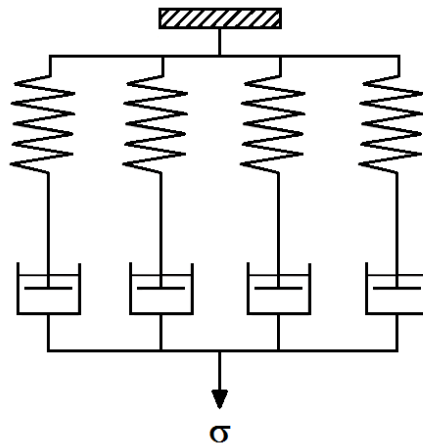Figure 3.4: Scheme of a multimode Maxwell model with Maxwell elements connected in parallel.

## 3.1.2 Time-temperature superposition (TTS) and the William-Landel-Ferry (WLF) equation

Every single rheological experiment at a defined temperature can provide data over only about 3 - 4 decades in time or frequency. By obtaining data at several temperatures, time-temperature superposition (TTS) can be used to generate master

curves to show the behavior at a reference temperature $T_{ref}$ over many decades of frequencies (up to 18 decades).

The time-temperature superposition principle can be introduced for themorheologically simple materials [104, 105]. Materials that do not follow the TTS principle are termed thermorheologically complex, and their behavior must be examined separately at every temperature and deformation rate of interest [106]. According to this semi-empirical method, a viscoelastic property (e.g. $G', G'', \tan\delta$) can be translated along the time (frequency) scale by changing the test temperature. It is important for TTS that the process involved in molecular relaxation or rearrangements occurs at accelerated rates at higher temperatures. Another important basis for TTS is that there is a direct equivalency between time (the frequency of measurement) and temperature. This means that the time over which the experiments are made, can be reduced by conducting the measurement at higher temperatures and shifting the resulting data to lower temperatures.

Quantities related to stress components, like $G'$ and $G''$, can be shifted by multiplying with a minor vertical (y-axis) shift factor $b_T$ and quantities related to time, like frequency or shear rate, can be shifted by multiplying with a substantial horizontal (x-axis) shift factor $a_T$. The result of this shifting is a "master curve" where the material property of interest at the specified end-use temperature can be predicted over a broad time scale. The equation of Williams-Landel-Ferry (WLF) [106] gives an estimation of the horizontal temperature shift factor $a_T$:

$$\log a_T = -\frac{C_1(T-T_{ref})}{C_2+(T-T_{ref})} \qquad (3.23)$$

where C1 and C2 are two polymer independent constants. For $T_{ref} = T_g$ the parameters have universal constant values $C_1$= 17.4 and $C_2$= 51.6 K for a large number of polymers [21, 111].

In the Rouse-Bueche [104] model for the linear viscoelasticity of unentangled polymer melts, the stress components, e.g. $G'$ and $G''$, are proportional to the product of density $\rho$ and temperature $T$, which implies:

$$b_T = \frac{T_{ref} \cdot \rho_{ref}}{T \cdot \rho} \qquad (3.23)$$

where $T$ and $\rho$ are the temperature and density, respectively. The vertical shift factor depends very weakly on temperature and the best practice is to set $b_T = 1$ if possible.

## 3.2 Entanglements and Tube model

In the Rouse-Bueche [104, 105] model for unentangled polymer melts the zero shear viscosity $\eta_0$ is proportional to the molecular weight, $\eta_0 \sim M_w^1$. This has been found to be valid for linear polymers at low molecular weights. At molecular weights above a critical molecular weight $M_c$ , the zero shear viscosity of the molten polymer depends upon $M_w$ to a power that is equal to about 3.4, $\eta_0 \sim M_w^{3.4}$, for polystyrene and 1,4-polybutadiene [105]. It approaches the Doi-Edward model, which predicts $\eta_0 \sim M_w^3$ [112]. The existence of two regimes in the molecular-weight dependence of the viscosity is due to polymer entanglements [106, 113]. At molecular weights below $M_c$, polymer chains are too short to knot up and entangle. Above $M_c$, the entanglements constrain the polymer chains meaning that the motion of polymer chains is significantly impeded by topological intermolecular constraints (see Figure 3.5a) causing the viscosity to increase dramatically compared to unentangled chains.

The reptation concept was first used to develop a model for polymer melts by Doi and Edward [112]. In this model, the polymer chain is trapped inside a tube (see Figure 3.5b) and can move only in a confined space. At very short times, the only relaxation process possible for the polymer chain is related to the redistribution of extensions among the segments between points where constraints are present. This rapid relaxation process has a characteristic time $\tau_e$ called the equilibration time, which has a value of e.g. $7 \cdot 10^{-9}$ s for polyethylene at 190 °C and 0.05 s for polystyrene at 150 °C [104, 105]. After this process is completed, the available relaxation mechanism is disengagement, i.e., reptation out of its tube. This process is relatively slow and has a characteristic time $\tau_d$, that depends strongly on the molecular mass.
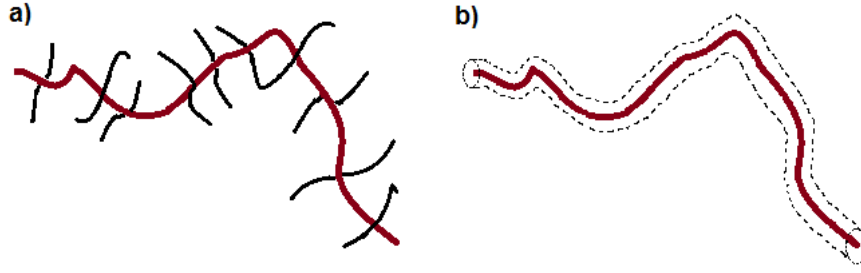
Figure 3.5: Schematic of a) a polymer chain showing the segments of the surrounding chains. The motion of the polymer chain is constrained by the surrounding chains, which restrict its motion in the direction normal to its length, b) the virtual tube to represent the restrictions of the surrounding chains on the polymer chain whose time evolution is being modeled.

The storage modulus of an entangled, monodisperse, melt polymer shows a plateau over a range of frequencies, which is referred to as the plateau modulus $G_N^0$. The plateau modulus of an entangled polymer melt is proportional to the density of entanglements and is a characteristic of the chemical structure of the monomer [105] as ca. 150 monomers are between two entanglements, in case the polymer backbone has freely rotating sp$^3$ hybridized carbones.

The plateau modulus $G_N^0$ can be estimating as the storage modulus at the frequency where $\tan(\delta)$ has its minimum value, as proposed by Wu [114]. An entangled polymer melt is similar to a rubber in which the crosslinked network is replaced by entanglements. The plateau modulus was used by Ferry [115] to define the average molecular weight between entanglements $M_e$.

$$M_e = \frac{\rho RT}{G_N^0} \qquad (3.24)$$

where $\rho$ is the polymer density, R is the ideal gas constant and T is the absolute temperature of the measurement. The later correction of Equation 3.24 resulted in a new definition of $M_e$ as 4/5 of the value defined by Equation 3.24. The reason for this correction is that, in stress relaxation, one fifth of the initial stress relaxes by fast Rouse modes before the entanglement network interrupts the process [104, 105]. The number of entanglements of a polymer can be defined as:

$$Z = \frac{M_w}{M_e} \qquad (3.25)$$

A master curve is used to obtain the full rheological characteristics of the polymer. Figure 3.6 shows the frequency dependent $G'$ and $G''$ measured from an oscillatory

shear test at a specific reference temperature. The Maxwell zone (viscose or terminal zone) is at low frequencies where $\omega \ll 1/\tau_d$ ($G' \sim \omega^2$ and $G'' \sim \omega$). The specific material behavior is dominated by its viscous fraction. In transition-to-flow zone, there is a change from a predominantly elastic region ($G' > G''$) to the region where flow behavior becomes significant ($G' < G''$). The crossover between $G'$ and $G''$ at $\omega = 1/\tau_d$ indicates the longest characteristic relaxation time $\tau_d$ and can be considered as the relaxation of a polymer chain via the reptation process [116]. Comparing two polymers with identical monomer units, same $M_n$ and different Đ, for the polymer with higher Đ, the crossover point occurs at a lower $G$-value (vertical shift of the crossover point depends on Đ). Comparing two polymers with identical monomer units, Đ and different $M_w$, for the polymer with higher $M_w$, the crossover point occurs at a lower frequency (longer molecules are less flexible and less mobile). Hence, a horizontal shift of the crossover point depends strongly on the value of $M_w$ [108].
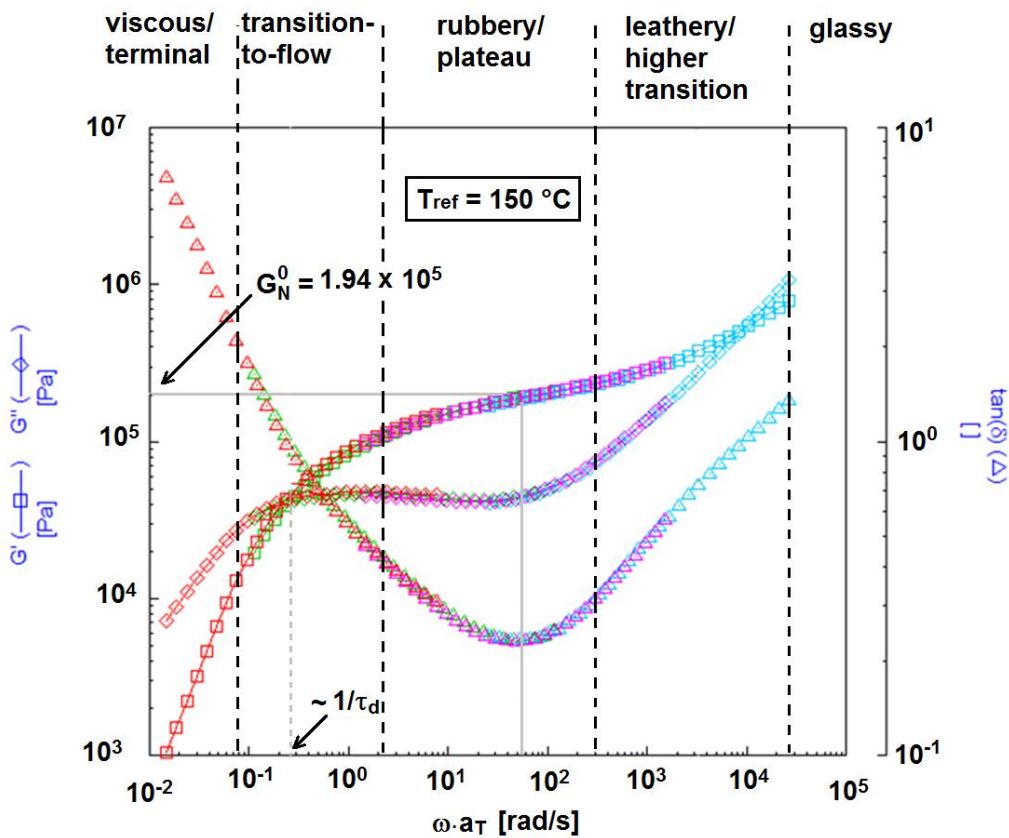


Figure 3.6: $G'(\omega)$ and $G''(\omega)$ of PS265 ($M_n$ = 265 kg/mol, $M_w$ = 292 kg/mol, Đ = 1.10) as a function of angular frequency at the reference temperature of 150 °C (~ $T_g$ + 50 °C).

In the range of higher frequencies ($\omega > 1/\tau_d$) the polymer chain dynamics are too slow to relax the original constraining tube within the investigated time scale and the entanglements, which build up the tube acts as a crosslinked network. The rubbery or plateau zone is the region where elastic behavior dominates. There is always a slight increase in $G'$ in this region, therefore a flat plateau appears. There is another crossover point at the leathery or higher transition zone. The value of $G''$ rises faster than $G'$ due to high-frequency relaxation and dissipation mechanisms [117]. At the highest frequencies, in the so called glassy region, $G''$ predominates and rises faster than $G'$.

## 3.3 Relaxation process of linear and comb polymers

The relaxation process of linear and comb samples can be investigated experimentally. Master curves for the frequency dependent dynamic melt moduli $G'(\omega)$ and $G''(\omega)$ are plotted in Figure 3.7 for a reference temperature of 150 °C using the time–temperature superposition principle for linear and comb PS samples. The linear samples PS90 and PS265 (see Table 2.1) show only one rubbery plateau, which is due to the physical entanglement of the linear polymer chains. The entanglement molecular weight of atactic PS is equal to $M_e$ = 18,100 g/mol [118], the average number of entanglements per chain is consequently ca. 5 for linear PS90 and ca. 16 for linear PS265 in the melt state. PS90 was used as the backbone for the combs. The investigated comb samples had side chains of differing lengths and the average number of entanglements of the side chains varied between 0.2 and 2 entanglements. Two relaxation processes were observed for the combs and were due to relaxation of the branches and backbone, respectively [119]. For PS combs (see Figure 2.10 and Table 2.1), the second rubbery plateau was not seen for samples that had less than 4 branches per backbone [88, 120]. Therefore, the relaxation behavior of PS90-4-42 resembled that of its linear backbone, but with an increase in its terminal relaxation time, $\tau_d$. PS90-5-30 showed instead two (slight) plateaus while these two regions were clearly distinguishable for PS90-13-12 and PS90-32-5.
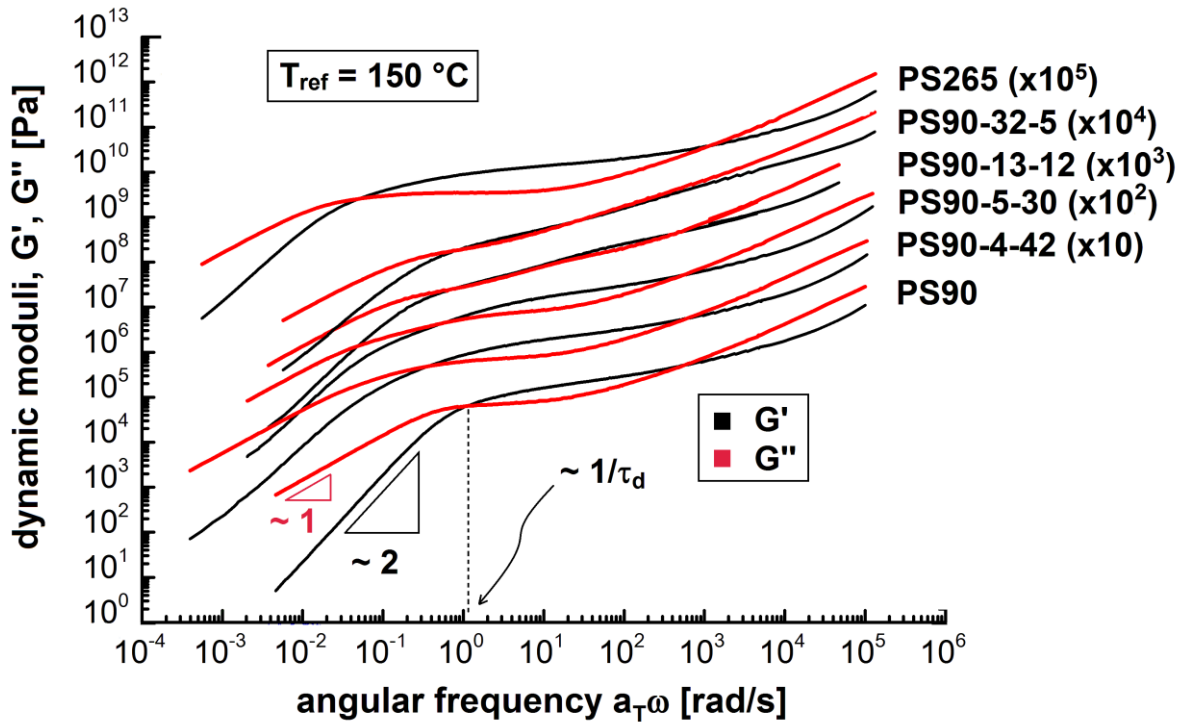
Figure 3.7: Linear viscoelastic master curves of linear and comb PS melts. For comb polymers, PS90-13-12 and PS90-32-5, two rubbery plateaus can be observed. The relaxation of the side arms occurred at higher frequencies. The backbone relaxed at lower frequencies, which is a result of the dynamic dilution caused by the relaxed side arms.

## 3.4 van Gurp-Palmen plot

The van Gurp-Palmen plot is another way of evaluating dynamic mechanical data [121]. This plot illustrates the phase angle $\delta = f_1(\omega)$ versus $|G^*| = f_2(\omega)$ leading to an elimination of the parameter $\omega$. For a thermorheologically simple material, van Gurp-Palmen plots at different temperatures fall on a master curve independent of molecular weight. Where TTS is valid, the quantities $\delta = f_1(\omega)$ and $|G^*| = f_2(\omega)$ become equal to $\delta = f_1(a_T\omega)$ and $|G^*| = f_2(a_T\omega)$ at other temperatures. After elimination of the parameter $a_T\omega$, the same curves are found. Figure 3.8 shows the van Gurp-Palmen curves for the investigated linear and comb PS samples. This type of replot of the data from Figure 3.7 is temperature and molecular weight invariant [104, 105] and is consequently the best way to determine branching effects. The main reason for the replot of the data is that the van Gurp-Palmen plot magnifies the distinctive effects of branching on the linear viscoelastic response [122-124]. The

degree of branching on the backbone increases the deviation from the results for the linear PS. This deviation is larger for the combs with a higher number of branches irrespective of the length of branches. However, the minimum $\delta$ value increased for PS90-13-12 and PS90-32-5, which both both $M_{n,sc}$ values that are lower than $M_e$ because of the effect of dynamic dilution on the backbone relaxation mechanism caused by the short side arms [88, 105]. Figure 3.8 shows that PS265 has a lower minimum value for $\delta$ relative to the samples with a backbone molecular weight of 90 kg/mol ($\sim$ 5 entanglements). This result means that the number of entanglements was not enough to superimpose the data for the two linear PS with $M_n$ = 90 and 265 kg/mol. For low branching degrees (e.g. PS90-4-42 and PS90-5-30) a second minimum can be observed as a slight deviation from the linear behavior of the entangled side chains.
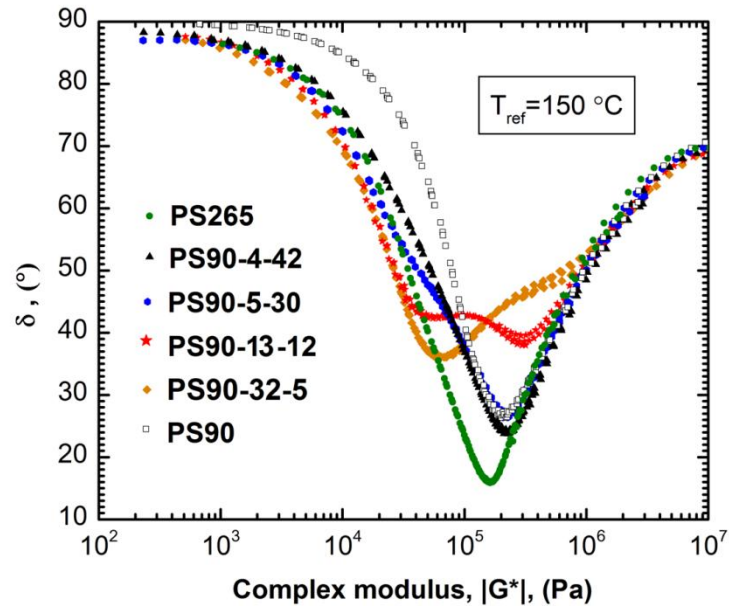


Figure 3.8: Van Gurp-Palmen plots for linear and comb PS samples. The data from the curves with higher values of $N_{br}$ show two characteristic minima, and are most prominent for PS90-13-12 and PS90-32-5.

## 3.5 Extensional rheology

### 3.5.1 Fundamentals

Elongational deformation plays a significant role in many processing operations, such as fiber spinning, blow molding and foam production [104, 121, 125]. The preferred test modes for the study of stretching deformations are those that generate only elongation at homogeneous strain and constant strain rate. Uniaxial extension, also

called simple extension, is an axisymmetric deformation in the direction of the axis of symmetry.
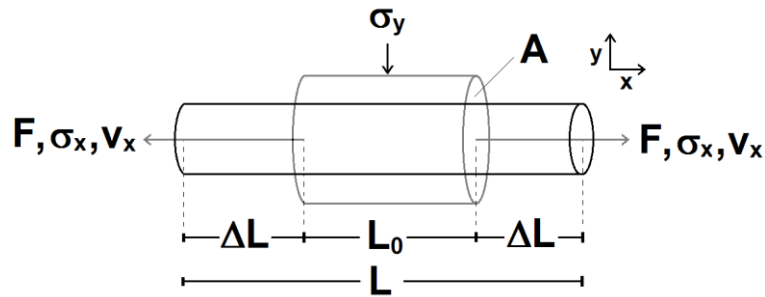


Figure 3.9: Deformation of a rod shape element in simple uniaxial extension.

Figure 3.9 shows uniaxial extension of a sample elongated at both ends with a constant velocity $v_x$ in the $x$ direction. In uniaxial extension molecules tend to be oriented in the axial direction. In extrudate flows with tensile stress (e.g. fiber spinning), extensional flow properties are very important. The extensional deformations are normally very long. The quantity $\varepsilon_H$ is called the Henckey strain and is defined by the change in the differential length $dL$ normalized to the actual length of the sample $L$.

$$d\varepsilon_H = \frac{dL}{L} = dlnL \qquad (3.26)$$

Simple extensional experiments on polymer melts, are often carried out at a constant Hencky strain rate, which is defined in terms of the length L of the sample as follows:

$$\dot{\varepsilon}_H = \frac{1}{L} \cdot \frac{dL}{dt} = \frac{dlnL}{dt} \qquad (3.27)$$

At a fixed distance of $x$, the velocity of the two ends is constant and proportional to the Hencky strain rate:

$$v_x = \dot{\varepsilon}_H \cdot x \qquad (3.28)$$

For an incompressible material the actual cross sectional area of a sample $A(t)$ can be calculated as follows:

$$A(t) = A_0 \cdot \exp(-\dot{\varepsilon}_H \cdot t); \; \pi R_0^2 L_0 = \pi R^2 L = const. \qquad (3.29)$$

Time dependent extensional stress $\sigma_{ext}(t)$ can be calculated from the force F(t) applied to the sample:

$$\sigma_{ext}(t) = \sigma_x(t) - \sigma_y(t) = \frac{F(t)}{A(t)} = \frac{F(t)}{A_0} \cdot \exp\left(\dot{\varepsilon}_H \cdot t\right) \qquad (3.30)$$

The material function usually reported is the tensile stress growth coefficient, which is also called the transient (i.e. time dependent) uniaxial extensional viscosity and is defined as

$$\eta_E^+(t, \dot{\varepsilon}_H) = \frac{\sigma_{ext}(t, \dot{\varepsilon}_H)}{\dot{\varepsilon}_H} \qquad (3.31)$$

According to the Boltzmann superposition principle and incompressibility, the following is valid in the linear viscoelastic (LVE) region (small strains or strain rates):

$$\lim_{\dot{\varepsilon}_H \to 0} \eta_E^+(t, \dot{\varepsilon}_H) = \eta_E^+(t) = 3\int_0^t G(s)ds = 3\eta^+(t) \qquad (3.32)$$

The linear relaxation modulus G(t) can be deduced from oscillatory shear data. In the case of steady extensional flow, the extensional viscosity can be determined as follows:

$$\lim_{t \to \infty} \eta_E^+(t, \dot{\varepsilon}_H) = \eta_E(\dot{\varepsilon}_H) \qquad (3.33)$$

and at small strain rates, the extensional viscosity becomes three times [106] the zero-shear viscosity:

$$\lim_{\dot{\varepsilon}_H \to 0} \eta_E(\dot{\varepsilon}_H) = 3\int_0^\infty G(s)ds = 3\eta_0 \qquad (3.34)$$

The extensional flow behavior of Newtonian fluids was first investigated by Trouton, and the quantity $\frac{\eta_E(\dot{\varepsilon}_H)}{\eta_0}$ is called the Trouton ratio. For an incompressible Newtonian fluid Trouton's ratio is 3.
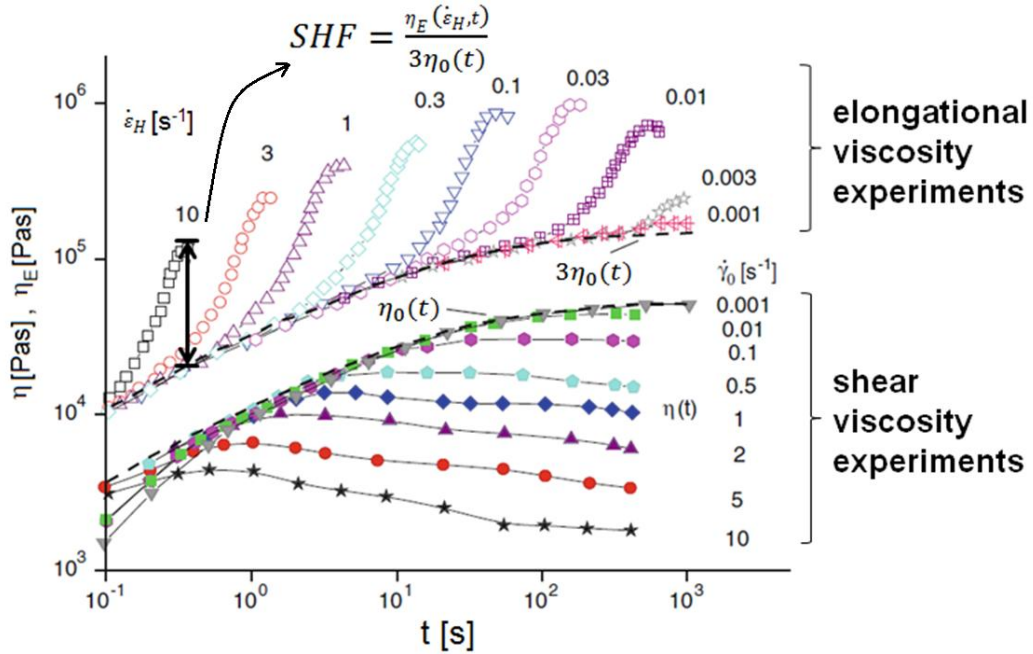


Figure 3.10: Time dependent elongational viscosity $\eta_E(\dot{\varepsilon}_H, t)$ and shear viscosity $\eta(\dot{\gamma}_0, t)$ for a LDPE sample at T = 150 °C. The elongational rates $\dot{\varepsilon}_H$ (open symbols) and shear rates $\dot{\gamma}_0$ (closed symbols) cover four decades from 0.001 to 10 s$^{-1}$ [121]. The strain hardening factor is indicated at $\dot{\varepsilon}_H$ = 10 s$^{-1}$.

Figure 3.10 shows elongational viscosity and shear viscosity experiments on a LDPE sample (IUPAC A) [121] as a function of time for constant elongational rates $\dot{\varepsilon}_H$ and constant shear rates $\dot{\gamma}_0$ from 0.001 to 10 s$^{-1}$, respectively [121]. At small elongational rates, all extensional measurements lie on the curve $3\eta_0$ indicating a linear viscoelastic behavior.

To quantify the increase in the elongational viscosity, the so called strain hardening factor is defined as (see Figure 3.10):

$$SHF = \frac{\eta_E^+(\dot{\varepsilon}_H, t)}{3\eta_0(t)} \qquad (3.35)$$

This parameter is relevant for the assessment of the processing behavior of polymeric materials. In elongation, the investigated LDPE exhibited strain hardening in the linear regime which was followed by strain thinning similar to that observed in the shear experiments.

### 3.7.2 Uniaxial extensional viscosity as determined from the Extensional Viscosity Fixture (EVF)

For uniaxial stretching of the samples, the Extensional Viscosity Fixture (EVF) from TA Instrument was employed. The design of EVF is based on the original Meissner concept [126] and is shown in figure 3.11. Instead of the rotary clamps, two cylinders are used to wind up the sample. One cylinder is rotating and the other one is fixed and measures the torque. In order to elongate the sample equally on both sides, the rotating cylinder moves on a circular orbit around the fixed cylinder, while rotating around its own axis at the same time. The sample is a small molded rectangular plaque that is clamped at each end to a rotating drum. The sample is small and thin, and all its surfaces are exposed to the oven atmosphere, where heating is very fast. The samples have widths from 3 to 12.7 mm and thicknesses from 0.2 to 0.8 mm [104].
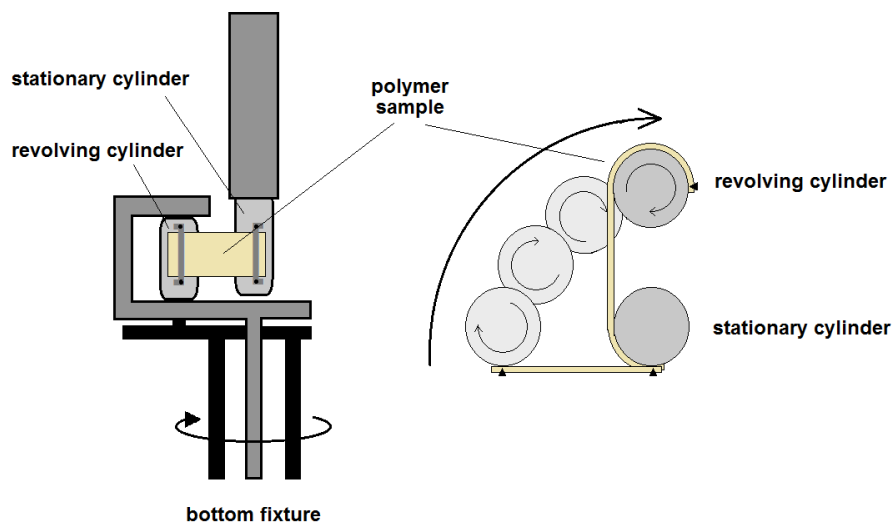


Figure 3.11: Schematic of an Elongational Viscosity Fixture (EVF).

Before the stretching experiment begins, the heated sample sags a bit after being clamped. Therefore, a pre-stretch is applied to the sample at a very low rate. The experiment can be started after the sample relaxes.

### 3.7.2.1 Extensional rheology of linear and comb polystyrene

An examination of the extensional flow characteristics of linear and comb PS was performed using an Advanced Rheometric Expansion System ARES-G2 from TA Instrument (Newcastle, USA) equipped with the EVF.
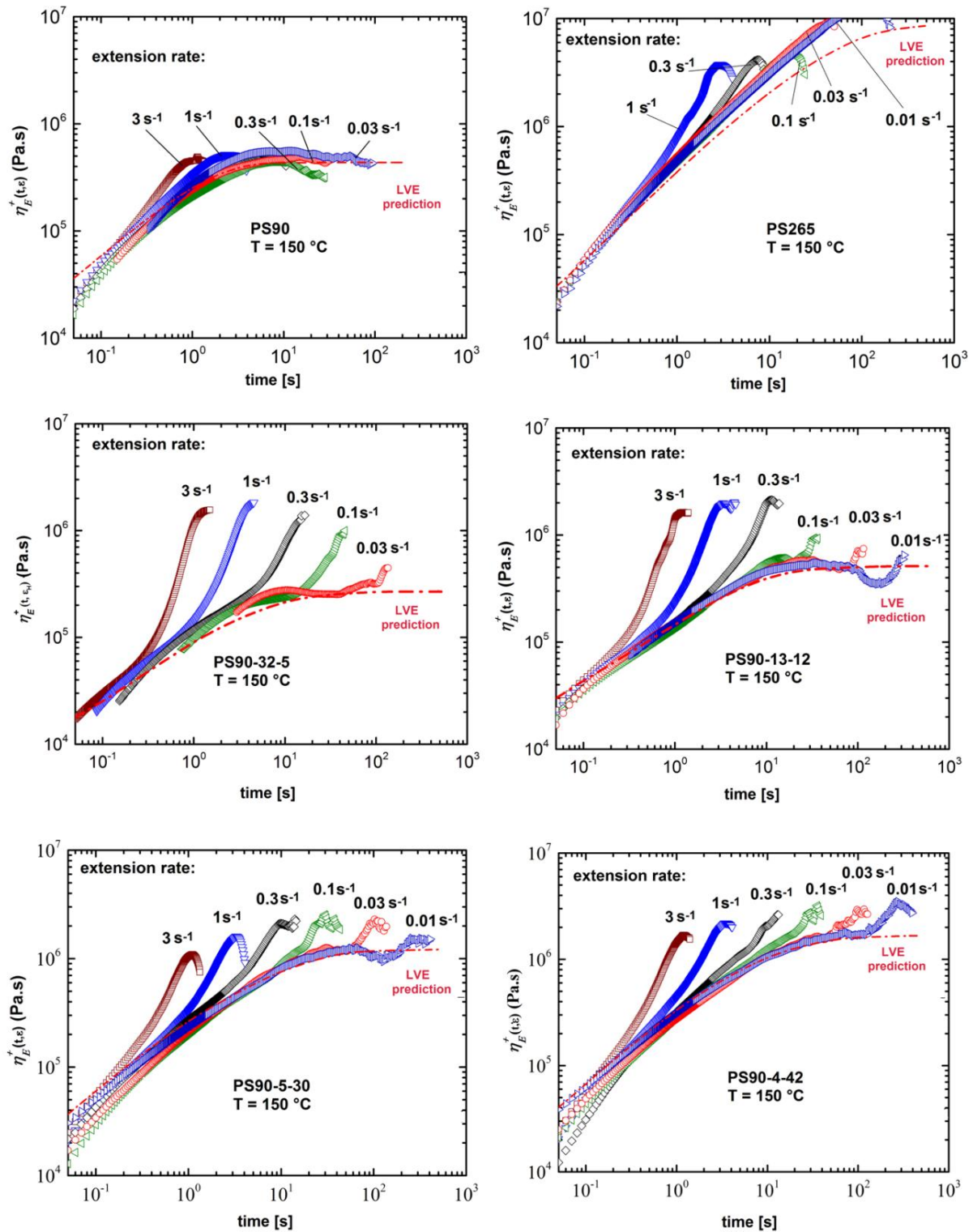
Figure 3.12: Extensional rheology measurements of linear and comb-PS. The polymer combs had the same backbone length, $M_{n,bb} \approx 90$ kg/mol and the same total molecular weight of the segments in the side chains, $N_{br} \cdot M_{n,sc} \approx 160$ kg/mol. The experiments were conducted at different extensional rates and T = 150 °C.

The influence of the number of branches $N_{br}$ and the length of the side arms $M_{n,sc}$ was investigated for four different PS combs. These combs had a constant backbone molecular weight, $M_{n,bb} \approx 90$ kg/mol and the total molecular weight of the segments in the side chains was nearly identical for all combs, $N_{br} \cdot M_{n,sc} \approx 160$ kg/mol. Figure 3.12 shows the experimental data of the tensile stress growth coefficient $\eta_E^+(\dot{\varepsilon}_H, t)$ versus time for different extensional rates at 150 °C for linear PS (PS90 and PS265) and comb PS (PS90-32-5, PS90-13-12, PS90-5-30 and PS90-4-42). For the linear PS, an increase in the molecular weight is accompanied by lower strain hardening at higher Hencky strain rates $\dot{\varepsilon}_H$. For the PS combs, all samples underwent strain hardening over the range of imposed extensional rates. In Figure 3.13 the strain hardening factors for combs as a function of the Hencky strain rate are presented. At higher Hencky strain rates, an increase in SHF can be observed with increasing number of side arms. The combs with entangled branches (PS90-5-30 and PS90-4-42) have higher SHF at lower Hencky strain rates.
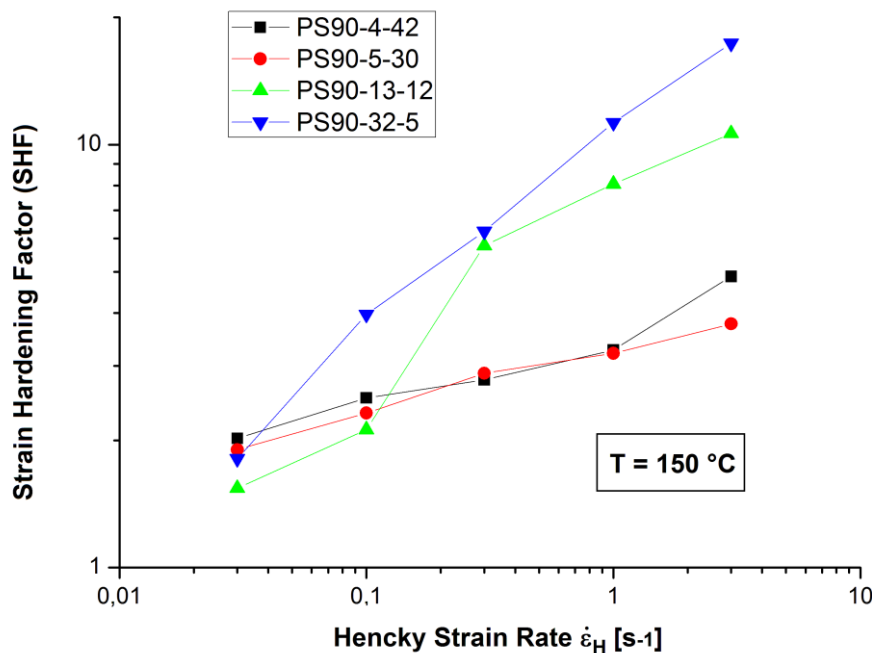


Figure 3.13: Strain hardening factor, $SHF = \eta_E^+(\dot{\varepsilon}_H, t)/3\eta_0(t)$ as a function of the extensional rate $\dot{\varepsilon}_H$ for combs where each have the same backbone and the same total molecular weight. At higher Hencky strain rates, an increase in SHF can be observed with increasing number of side arms. The combs with entangled branches showed only a slight increase in the SHF at lower Hencky strain rates.

## 3.8  Capillary and slit rheometery

Capillary and slit rheometers have extensively been used to determine the melt viscosity  at high shear rates where measurements with rotational rheometery become difficult [127]. The plunger-type capillary rheometer is very simple to design and operate. The polymer granules are put into the reservoir section of a capillary die, as shown in Figure 3.14, which is heated to melt the polymer sample to the desired experimental temperature.
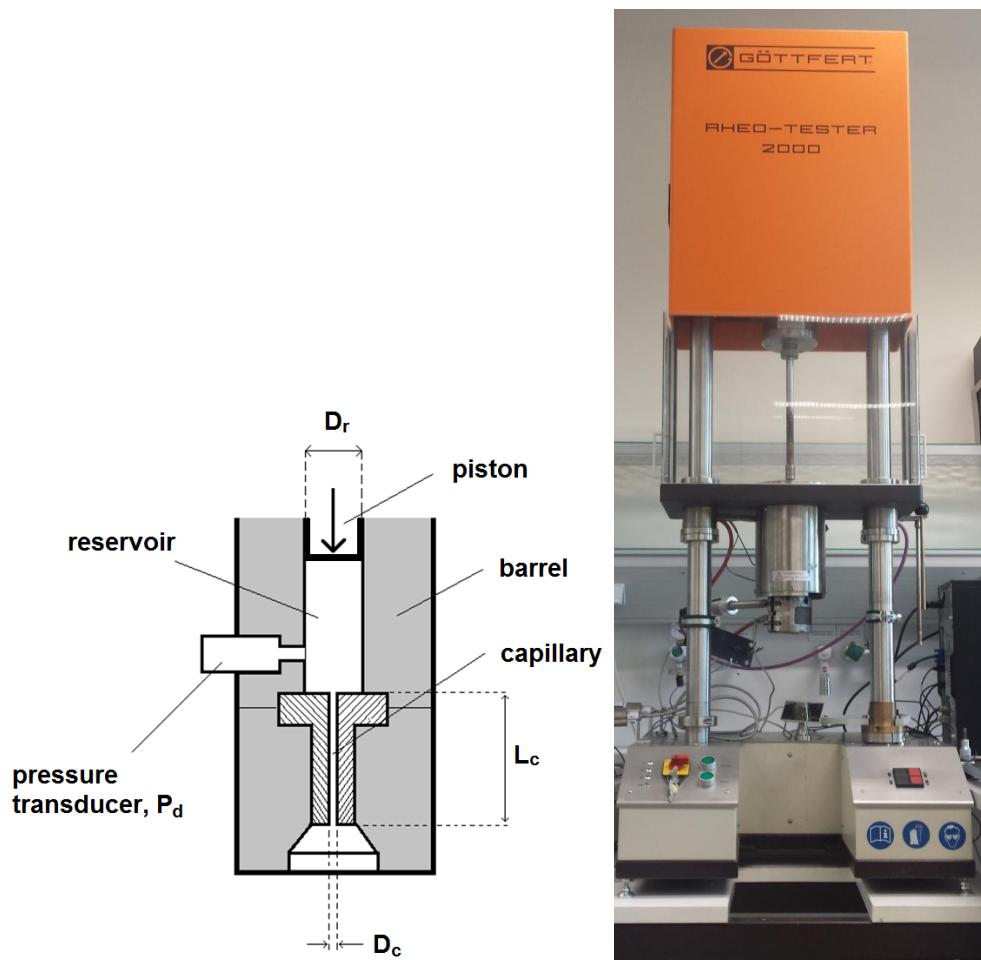


Figure 3.14: Left: Schematic of a piston type capillary rheometer cross section, Right: Göttfert Rheo-tester 2000, which was used in this study.

The plunger is placed at the top of the reservoir and then pushed down using a servomotor. The reservoir pressure $P_d$ is measured and corresponds to various volumetric flow rates $Q$ for each experiment.

In the case of a round capillary, the apparent wall shear stress $\sigma_{app}$ and apparent wall shear rate $\dot{\gamma}_{app}$ can be calculated as follows:

$$\sigma_{app} = \frac{P_d D_c}{4 L_c} \qquad (3.36)$$

$$\dot{\gamma}_{app} = \frac{32Q}{\pi D_c^3} \qquad (3.37)$$

where $D_c$ and $L_c$ are the diameter and the length of the capillary, respectively. The apparent viscosity can be calculated as follows:

$$\eta_{app} = \frac{\sigma_{app}}{\dot{\gamma}_{app}} = \frac{\pi P_d D_c^4}{128 Q L_c} \qquad (3.38)$$

The equation for the apparent shear stress ignores the entrance pressure drop and the equation for the apparent shear rate is only correct for a Newtonian fluid in the absence of wall slip [104]. Typically two main corrections are applied to both quantities to obtain a true viscosity-shear rate curve. These are the Bagley [128] and Weissenberg-Rabinowitsch [129, 130] corrections. The Bagley correction is based on a linear extrapolation of the pressure versus $L_c/R_c$ at a constant apparent shear rate $\dot{\gamma}_{app}$ ($R_c$ is the capillary radius). The Bagley correction for the wall shear stress $\sigma_w$ can be expressed as:

$$\sigma_w = \frac{P_d}{2(L_c/R_c + e)} \qquad (3.39)$$

where $e$ is a correction factor, called the Bagley end correction, and will vary with the shear rate. The correction factor $e$ can be found by extrapolation of the straight line to $P_d = 0$.

The shear rate at the wall $\dot{\gamma}_w$ can be corrected according to a power-law model by use of the Weissenberg-Rabinowitsch equation. The shear rate at the wall in capillary flow is given as:

$$\dot{\gamma}_w = \dot{\gamma}_{app} \left[ \frac{1}{4} \left( 3 + \frac{d \ln \dot{\gamma}_{app}}{d \ln \sigma_w} \right) \right] \qquad (3.40)$$

The quantity in square brackets is called the Weissenberg–Rabinowitsch correction. For Newtonian fluids the correction becomes 1. This correction allows calculation of the shear rate at the wall without assuming any form for the velocity profile. A value of 0.83 for the shift factor results in a viscosity error that is less than 2 % [104, 106].

In capillary rheometry with round dies, the relevant pressure difference cannot be measured inside the die. There are no pressure sensors small enough to be mounted into the small round capillaries [107]. The pressure is instead measured in the reservoir leading to the die and the ambient pressure at the die exit. The capillaries can also have slit cross sections. The flat flow channel makes it possible to install pressure sensors inside the die (see Figure 3.15). Therefore, the pressure drop $\Delta P$ experienced by the sample can be measured via two pressure sensors placed inside the die. The distance between the sensors is the capillary length of $\Delta L$ and the sensors are situated sufficiently far away from both the entrance and die exit to eliminate the introduction of non-laminar flow in the polymer melt.
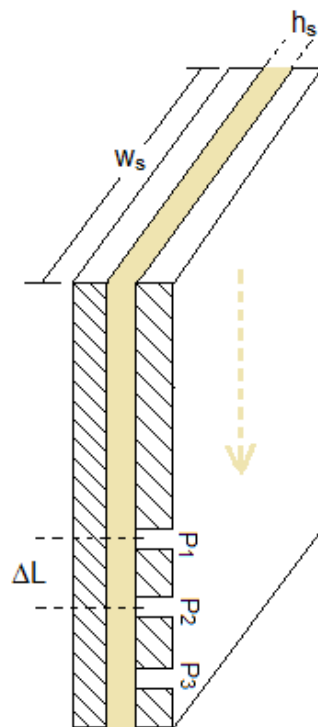


Figure 3.15: Sketch of a slit rheometer geometry.

The data consisting of the pressure drop $\Delta P$ at volumetric flow rates $Q$ can be used to calculate the wall shear stress $\sigma_w$ and the apparent wall shear rate $\dot{\gamma}_{app}$ as follows:

$$\sigma_w = \frac{h_s \Delta P}{2\Delta l} \qquad (3.41)$$

$$\dot{\gamma}_{app} = \frac{6Q}{w_s h_s^2} \qquad (3.42)$$

where $h_s$ and $w_s$ are the slit thickness and the slit width of the capillary ($h_s \ll w_s$), respectively [107, 130, 131]. The apparent viscosity can be calculated as follows:

$$\eta_{app} = \frac{\sigma_w}{\dot{\gamma}_{app}} = \frac{w_s h_s^3 \Delta P}{12\Delta l Q} \qquad (3.43)$$

The measurement of viscosity, both in the slit and capillary rheometer, is based on the assumption that both the density and the temperature of the polymer are constant inside the die. It has been estimated that the effect of the variable melt density on the temperature and pressure coefficients of polymer melts (e.g. LDPE) remains below 5 % [104, 132]. Therefore, the error with regard to the experimental accuracy of the coefficients based on the assumption of an incompressible melt is negligible [132].

### 3.8.1 Relation between dynamic mechanical and stressing experiments (Cox-Merz rule)

The form of the frequency dependence of the complex viscosity $|\eta^*(\omega)|$ for simple polymer (linear, mono disperse homopolymers) melts is often identical to that of the viscosity function $\eta(\dot{\gamma})$:

$$\eta(\dot{\gamma}) = \lim_{t\to\infty} \eta(\dot{\gamma}) \cong |\eta^*(\omega)| \quad \text{for } \dot{\gamma} \equiv \omega$$

This empirical correlation, called the Cox-Merz rule, was first reported by Cox and Merz for polystyrene samples [133]. The Cox-Merz rule has been confirmed experimentally for many polymer melts and solutions of several random-coil

polysaccharides [115, 134]. However, many exceptions have been found to the Cox-Merz rule, e.g. block copolymers, biopolymers and suspensions [107, 134-137].

The advantage of the Cox-Merz rule is that technically it is simpler to work with frequencies than with shear rates. Oscillatory shear measurements provide more precise data than capillary rheometry and require less sample quantities. For polymer melts and solutions in rotational rheometers with cone-plate or plate-plate geometries, the measurements at high shear rates ($\dot{\gamma} > 50$ s$^{-1}$) are limited via the Weissenberg effect (climbing-up of the sample from a rotating geometry) [107].

In Figure 3.16, the Cox-Merz rule for a sample of a commercial isotactic polypropylene (i-PP) is verified, which is shown to be valid over the range of shear rates and angular frequencies measured.
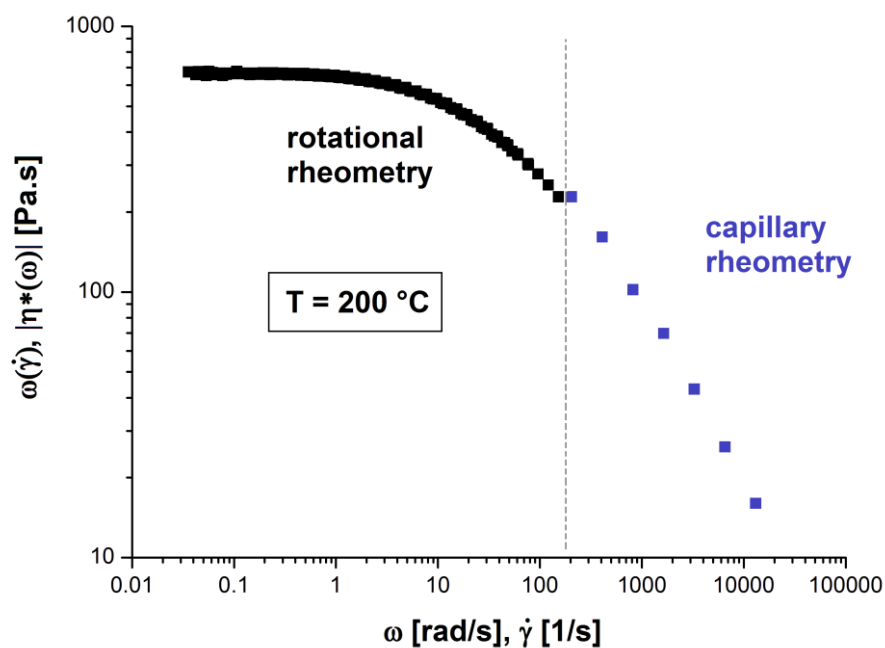


Figure 3.16: Rotational and capillary rheometry results superimposed for i-PP (Moplen HP561R, LyondellBasell, $M_w$ = 180 kg/mol, Đ = 2.3) at 200 °C.

Dynamic rheological measurements of this polymer were carried out in an ARES-G2 (TA Instruments) over the frequency range from 0.06 to 100 rad/s at temperatures ranging from 160 to 240 °C. Time temperature superposition was done according to a shift factor to a reference temperature of 200 °C. High pressure capillary measurements of the polymer were performed simultaneously on a capillary rheometer (see Figure 3.14) at 200°C. A round die with D = 0.3 mm diameter and a

length/diameter (L/D) ratio of 100 was used. The range of apparent shear rates was between 200 and 13,000 s$^{-1}$. The viscosity versus frequency measured on the ARES-G2 and the viscosity versus shear rate measured on the Göttfert Rheotester 2000 are shown in Figure 3.15. That Figure shows that the Cox-Merz transformation is satisfied.

## 3.9  Conclusion

The rheological characterization of model polymers was examined. The combs were investigated in the linear regime using the van Gurp-Palmen plot. The data from the curves with higher values of $N_{br}$ were showed two characteristic points, which correspond to the two minima in the plot and were most prominent for PS90-13-12 and PS90-32-5. The uniaxial extensional measurements were further investigated. These measurements were related to the melt spinning of model polymers. In the case of linear PS, an increase in the molecular weight was accompanied by a lower strain hardening at higher Hencky strain rates $\dot{\varepsilon}_H$. In the case of the PS combs, all samples underwent strain hardening over the range of the imposed extensional rate. At higher Hencky strain rates, an increase in SHF was observed with increasing number of side arms. The combs with entangled branches (PS90-5-30 and PS90-4-42) have slightly higher SHF at lower Hencky strain rates.

## 4. Fiber spinning

## 4.1 Introduction

The first man-made fibers were produced towards the end of the nineteenth century on the basis of natural polymers [13, 16, 138]. The purpose was to create fibers from cellulose or casein. Natural polymers do not melt and decompose at higher temperature. This simple fact dictated the first methods of fiber formation. Nitrocellulose is soluble in alcohol and ether and the solution can be extruded through fine holes. In the Chardonnet process (method of producing Chardonnet silk from a solution of nitrocellulose), the solvent evaporates in air and fibers are formed and reconverted to cellulose. This process was patented in 1885 and was the first artificial silk to be produced in a considerable quantity.

The process of making viscose rayon from waste cotton or wood pulps was discovered by Cross and Bevan in 1893 but took time to become established [16, 139]. In this process, the purified cellulose is treated with sodium hydroxide, which converts it into alkali cellulose. It is then treated with carbon disulfide to form sodium cellulose xanthate. This solution is then diluted and aged until it reached the correct viscosity for extrusion. It is then spun into an acid coagulating bath, which precipitates the cellulose in the form of a viscose filament.

With continuing progress in the area of synthetic macromolecules, thermoplastic polymers were considered for fiber formation [16, 140]. The big jump in commercial production of synthetic fibers came first in 1939 with the invention of polyamide 66 by Wallace Carothers, and this was followed in the 1950s by acrylic (polyacrylonitrile), polyesters, and many other synthetic fibers.

The thermoplastic nature of many polymers allows for the omission of solvents in fiber formation, but extrusion and further processing of the highly viscose melt creates new problems. These problems as they relate to fiber spinning became an important field of research in rheology [141, 142].

There are different fiber formation techniques [13, 16, 141]. To make a fiber in general, the polymer melt or solution is extruded from a fine hole and elongated by the application of a tensile external force. As the polymer melt or solution is pulled, it is cooled or precipitated to form a solid filament (see Figure 4.1). In solution spinning, polymers or their modifications are dissolved and, by subsequent removal of the

solvent, fibers are formed. In dry spinning, the solvent is removed through evaporation. In wet spinning the solvent is removed through extraction, with or without a chemical reaction taking place simultaneously. Melt spinning is the simplest extrusion process [3] and has the advantage that no costly solvents are required that have to be removed afterwards. Melt spinning is preferred for those polymers that can be melted without undergoing a thermal degradation [13, 143]. In melt spinning the polymer is melted and extruded through a spinneret and the liquid threadlines solidify while passing through a cooling medium. This method is used for producing polyamide (polyamide 66 and polyamide 6), polyethylene terephthalate (polyester) and polypropylene fibers [3]. Three conventional spinning processes are shown schematically in Figure 4.1.

In all of these fiber spinning methods, the main steps are drawing, which is unidirectional stretch of the filament into a semi-solid form, and heat-setting, which is crystallization to equilibrium [9, 141].
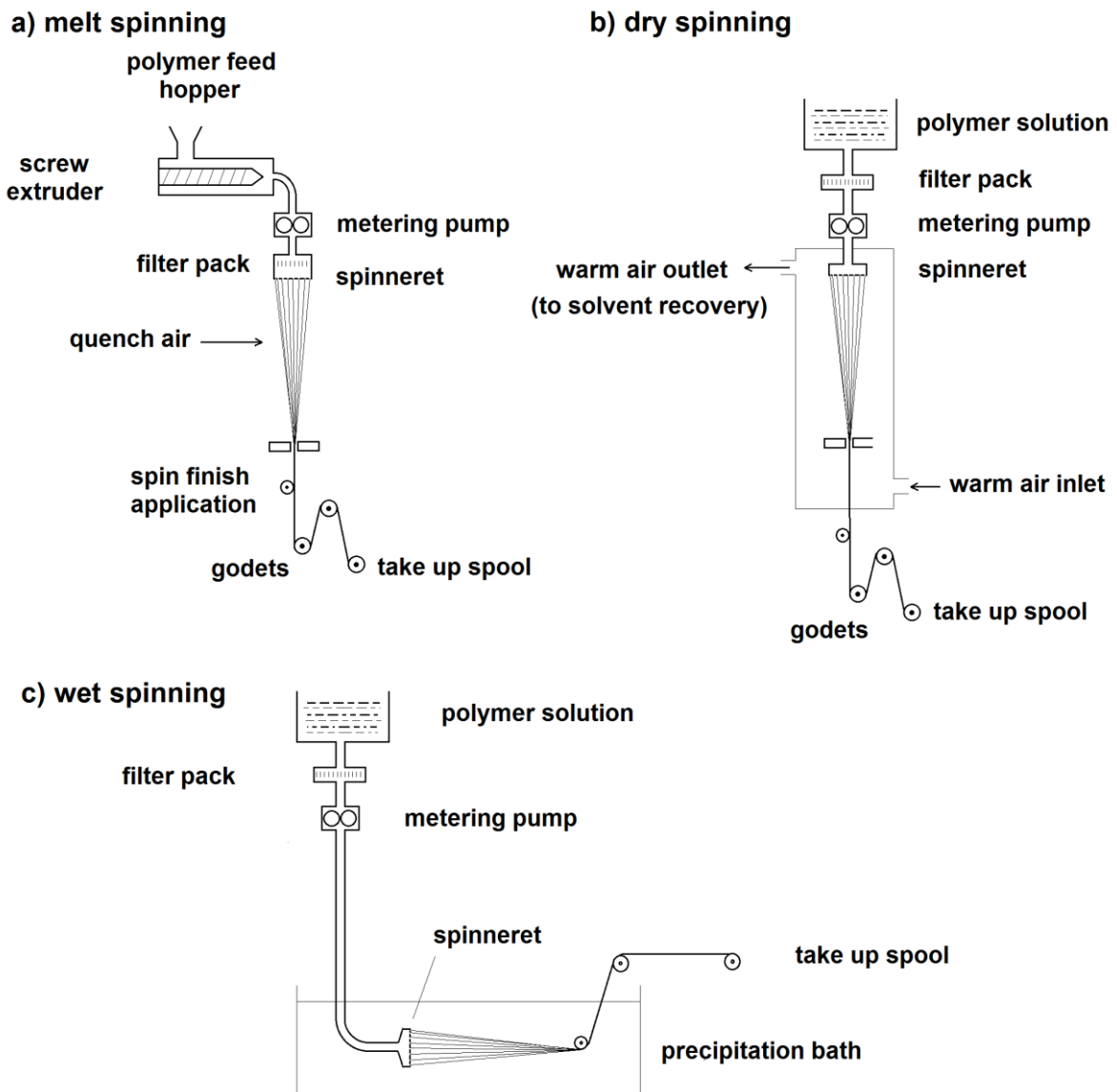
Figure 4.1: Schematic diagrams of the a) melt spinning, b) dry spinning, and c) wet spinning processes.

Fibers have high strength, high flexibility, high extensibility and show recoverability on deformation [8, 144]. These properties are observed in one direction, which is known as the axis of the fiber. The orientation of the polymer chains should be in the direction along the fiber axis. The more oriented the polymer chains are in this direction, the better mechanical properties the resulting fiber is considered to have.

Hermans has defined an optical orientation factor, $f$, as the ratio of the birefringence (see Equation 4.1) of the fiber to that of an ideal fiber in which the molecules are perfectly oriented parallel to the fiber axis [8]. He has used the average angle of inclination of the molecules, $\varphi$, which is defined as the angle of inclination in an imaginary fiber where all the molecules are arranged at the same angle and have the same birefringence as the actual fiber. He showed that:

$$f = \frac{n_\| - n_\perp}{n'_\| - n'_\perp} = 1 - \frac{3}{2} sin^2\varphi \qquad (4.1)$$

where $n_\|$ and $n_\perp$ are the refractive indices, parallel and perpendicular to the fiber axis, respectively and $n'_\|$ and $n'_\perp$ are the analogs for the ideally oriented fiber. For an ideally oriented fiber, $f = 1$ and $\varphi = 0$. For an isotropic fiber (no birefringence), $f = 0$, $sin^2\varphi = \frac{2}{3}$ and $\varphi$ is approximately 54.7°.


## 4.2 Melt spinning

Melt spinning was developed in the late 1930s to process polyamide 6 and polyamide 66 [16]. Afterwards other polymers were used, including polyester (PET) and polyolefins (polyethylene and polypropylene), which are all widely used in the textile industry. The main disadvantage of melt spinning is the risk of thermal decomposition of the molten polymer by oxidation during extrusion [3]. However, thermal oxidation usually includes radical chain reactions which can be prevented by adding antioxidants to the polymer or by spinning in a nitrogen atmosphere.

In the melt spinning process, the dried polymer pellets or granules are usually fed into an extruder (Figure 4.1 a). The polymeric melt is extruded and the screw action drives it towards a metering pump (usually a gear pump), which pushes a constant flow of molten polymer under pressure through the holes of the spinneret. Before molten polymer reaches the spinneret, a filter pack removes unwanted solid impurities. Within the spinneret the melt flow is channeled into a number of individual capillary holes.  Each hole is responsible for the formation of a single filament. The filaments are pulled and solidified through a cooling chamber and are collected into a fiber bundle that is finally wound up. Before the filaments reach the roller, they are treated with a liquid spin finish, which is a complex mixture of a wide range of

chemical components (lubricants, antistatic agents, antioxidants and emulsifiers). The primary functions of spin finish are to provide surface lubrication of the fiber (to reduce friction between filaments and metallic or ceramic parts of the spin line), improved antistatic properties and provide fiber-to fiber cohesion [145].

The take-up speed is much higher than the average extrusion velocity at the spinneret exit. The ratio between the spinning velocity $V_L$ (velocity at the godets) and the (average) extrusion velocity $V_0$ defines the draw down ratio (DDR):

$$DDR = \frac{V_L}{V_0} \qquad (4.2)$$

The take up velocity ($V_L$) is generally in the range of 1000-6000 m/min [13]. The stretching of the filaments in this steps results in a greater degree of alignment in the direction of the filament axis.

## 4.3 Drawing

The undrawn fibers have a low orientation of the polymer chains, which gives the fibers with poor mechanical performance [3, 9]. Between take up of the as-spun fiber and the final take-up rolls, an additional drawing procedure may be introduced. The drawing is typically achieved by means of godet pairs and it may consist of several stages. Important control parameters are the draw ratio (DR), draw temperatures, draw speed and the number of draw stages. Drawing takes place above the glass temperature $T_g$ of the polymer. Neck formation occurs at lower draw temperatures, higher draw speeds and higher orientations of the polymer chain in the undrawn filament.

The spinning speed can affect the structure and properties of the produced fibers [13, 146]. The take up speed should be between 1000 to 1800 m/min for polyester fibers (e.g. PET) to make undrawn low orientated yarn (LOY). Partially oriented yarn (POY) is spun at speeds between 2800 to 4000 m/min. The thread-line orientation is high enough to cause crystallization on cooling [8]. This enables the wind-up of POY, which is stable and suitable for supply to yarn texturing companies. It is possible to produce polyester yarns that can be used in textiles without further processing. Fully oriented yarn (FOY) is spun at speeds in excess of 6000 m/min.

## 4.4 Texturing

Drown multifilament yarn is textured for certain applications, to improve comfort and enhance thermal insulation [147]. The texturing process on fibers is not discussed in detail in this study, but due to its importance in the melt spinning process, a short summary of this processing step is necessary. Texturing confers a significantly larger volume to the yarn by increasing the number of bends and loops in the constituent filaments, so that there is considerable air space within the yarn. Textured yarns may be cut into staple fibers, typically 4-20 cm, and then packed into bales. They are sometimes mixed with a natural fiber and then converted into blend yarns. The bulked continuous filament (BCF) production can be converted into a one-step spinning–drawing–texturing process for carpet and other applications [148]. In this process, the yarn is generally spun at a take-up speed of about 2000 m/min, immediately drawn on panel at a draw ratio from 1.1 to 2.5, and then passed through a texturing device to develop a crimped fiber. The crimped fiber continues onto a perforated drum for cooling before it is wound up on a package. Alternatively, an undrawn yarn spun earlier can be used as a feeder yarn to be drawn and textured as above.

## 4.5 Spinnability

Spinnability is the capability of materials to form fibers during a spinning process. Some polymers (e.g. Polyamide 66, PET) are spinnable and can resist breakage of the filament at high take-up speeds, but other fibers formed from polymers like PP and HDPE are not able to withstand high take up speeds (8000 m/min). A spinnable polymer must meet these necessary conditions [9]:

- Attenuation and acceleration of the filaments, i.e. $DDR$ >1
- Steady state conditions, which means uniform filaments without any variation of properties during the production time and along the filament length

Spinnability is one of the fundamental questions to be considered in the process of fiber formation [149]. The theoretical and practical analysis of fiber spinning dynamics was first developed by Ziabicki [146, 150] and continiued by other scientists [10, 151-153]. Ziabicki stated six important parameters affecting spinnability in a melt spinning

process [150]. They are the processing temperature, dimension and number of spinneret holes, mass throughput, length of the spinning path, take-up speed and cooling conditions. The effects of these parameters on the spinnability of different polymers were investigated by many scientists, but it seems from the literature that there is no simple definition of spinnability that everyone can agree on [142].

However, the definition of the maximum draw-down ratio ($DDR_{max}$) is useful to compare the spinnability of two different polymers:

$$DDR_{max} = \frac{V_{L,max}}{V_0} \qquad (4.3)$$

where $V_{L,max}$ is the maximum take up speed at which spin-line breakdown occurs, and $V_0$ is the average velocity of the melt inside a spinneret hole. The $DDR_{max}$ parameter relates to all six important parameters identified by Ziabicki for the melt spinning process [9, 142, 150].

For a highly spinnable polymer, a $DDR$ value of several hundreds to one thousand can be reached in a high speed spinning process. Structural changes and phase transitions from the melt to solid state can possibly occur on the order of milliseconds [9].

## 4.6  Fiber spinning Instabilities

There are various filament instabilities possible in the process of fiber formation [154]. Capillarity failure is the first instability in the melt spinning process described by Ziabicki [150] and Ide and White [155]. This instability occurs because of the surface tension of the fluid, which results in the breakup of the fiber into droplets or ligaments. Another instability during the fiber spinning process is ductile failure caused by extension thinning of polymers due to the growth of a neck generated by high local stresses [156, 157]. Extension thickening of polymers can also cause instabilities. This is due to cohesive failure resulting from instantaneous reduction or breakage of a finite cross section of the filament [150]. This instability is called draw resonance and arises with an increase in the value of $DDR$.

The above mentioned instabilities are related to the spinnability of a polymer. A lack of spinnability leads to breakup of the filament during fiber formation.

Commercial polymer processing operations (e.g. fiber spinning, film blowing) suffer by the onset of flow instabilities. The study of polymer melt instabilities during the extrusion of polymer melts has received considerable interest in both industry and academic researches [154, 158, 159]. Melt fracture is often signaled by surface irregularities of the extrudate that develop with increasing shear rates. The onset of melt fracture is often a key limitation to the maximum output shear rate of an extrusion line [154].

For shear rates higher than a critical value, melt fracture occurs during the melt spinning process in a given spinneret at a given spinning temperature (see Figure 4.2).
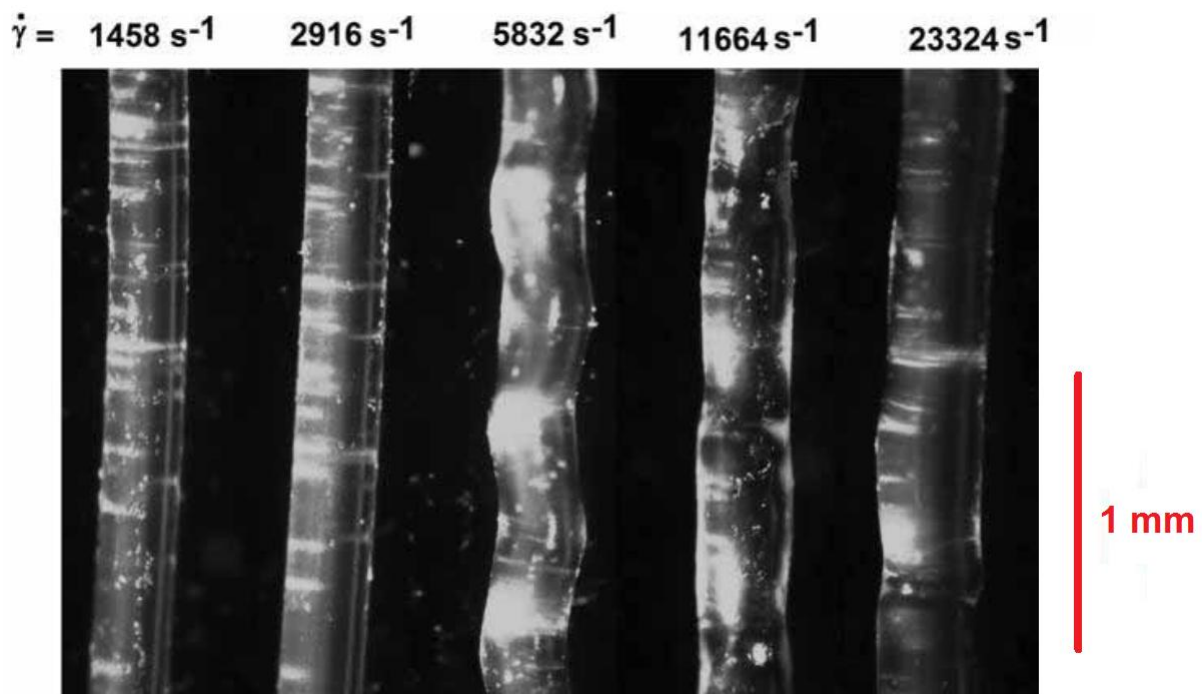


Figure 4.2: Microscopic images of the flow instabilities of a commercial iPP (Moplen HP561R, LyondellBasell, $M_w$ = 180 kg/mol, Đ = 2.3) from a round die (D = 0.3 mm, L = 5 mm, T = 180 °C) at various shear rates (without Haul-off).

The melt flow instabilities of a molten polymer can be split into three main categories: sharkskin, stick-slip and gross melt fracture. The sharkskin instability (see Figure 4.3 b) is the most commonly observed in the extrusion of polyethylene, polypropylene, polydimethylsiloxane (PDMS), and polyisobutylene (PIB) [154]. The sharkskin starts at high shear rates and is a small scale distortion on the surface of the extrudate with a small amplitude and wavelength with respect to the diameter of

the extrudate. The stick-slip instability (see Figure 4.3 c) is associated with pressure and extrudate flow rate oscillations. This is observed when the throughput is controlled. The oscillations result in alternating rough and relatively smooth regions on the surface of the extrudate. Gross melt fracture (GMF) occurs at higher shear rates (see Figure 4.3 d). This phenomenon affects the entire cross section of the extrudate. The amplitude of the instability in GMF is large in comparison to the thickness of the extrudate.
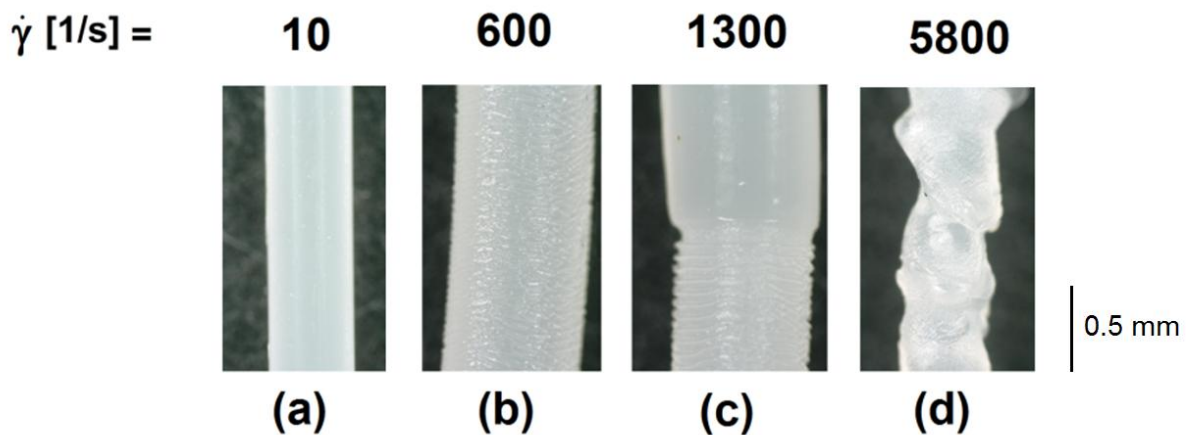


Figure 4.3: Typical extrudates of a commercial HDPE at different shear rates and T =170 °C showing (a) smooth surface, (b) shark skin, (c) stick-slip and (d) gross melt fracture (D = 0.5 mm, L = 15 mm).

The melt fracture phenomenon is known as an important instability that can limit the rate of production in the process of fiber formation. A brittle type of fracture due to crystallization induced by stretching and necking of a polymer, which is caused by capillary waves, is an instability related to the spinnability of a polymer.

## 4.7  Melt spinning of polymers- detection of mechanical instabilities

This section is focused on the development and improvement of experimental techniques to find the relationship between pressure fluctuations and melt flow instabilities in the die during fiber spinning processes in a commercial capillary rheometer. The experiments in this study were performed using a capillary rheometer equipped with a Haul-off system (0-600 m/min). The capillary rheometer uses a constant piston velocity (see Figure 4.4).
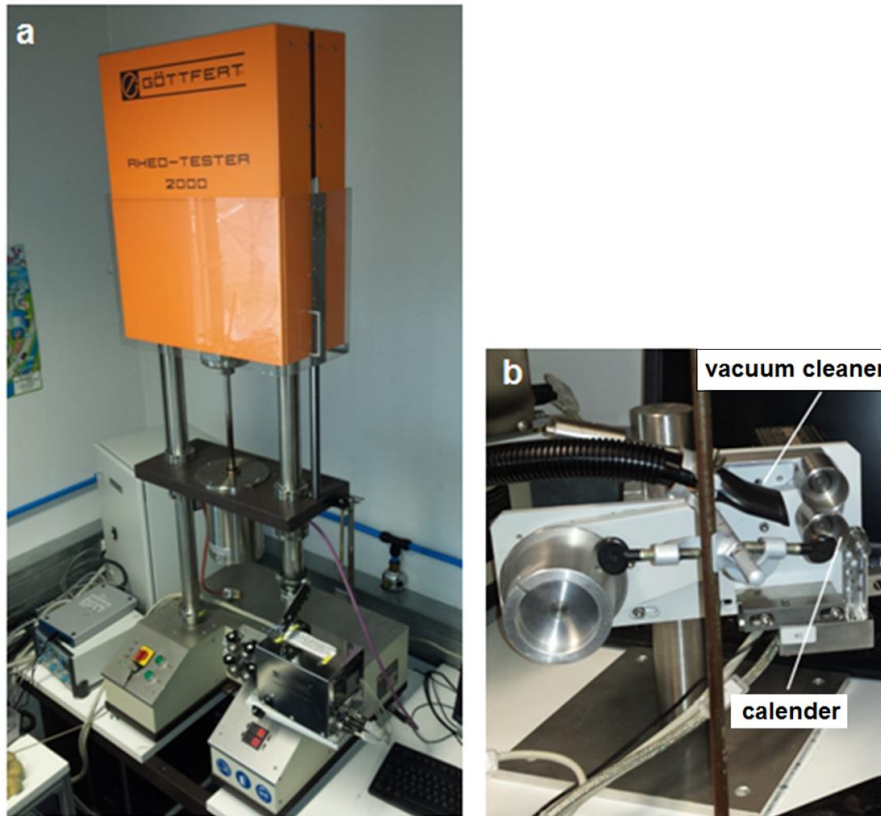
Figure 4.4: Picture of the experimental setup a) Rheo-tester 2000 and b) Haul-off system, both from the company Göttfert. In addition, a vacuum cleaner (a simple version of a Venturi gun typically used in fiber spinning) was used to collect the fibers.

In order to determine the model substances, a subset of polymers used commercially used in the textile industry were selected and examined. The focus was on polyamide (Ultramid B27) (BASF), poly (ethylene terephthalate) (PET) (V004) (Invista) and isotactic polypropelene (Moplen HP561R) (LyondellBasell). The most important parameters for the processing of these polymers are the extrusion temperature, the take-up speed and the cooling rate during fiber formation. It was observed that the polymer fibers of some samples were discolored and turned partially brown. The residence time of the polymer pellets in the capillary rheometer was about 1 h for heating, melting and temperature stabilization, which results in polymer degradation at higher temperatures. Rheological experiments showed that the viscosity of the polymer melt decreases continuously upon long exposure of the polymer to high temperatures under an air atmosphere (see Figure 4.5).
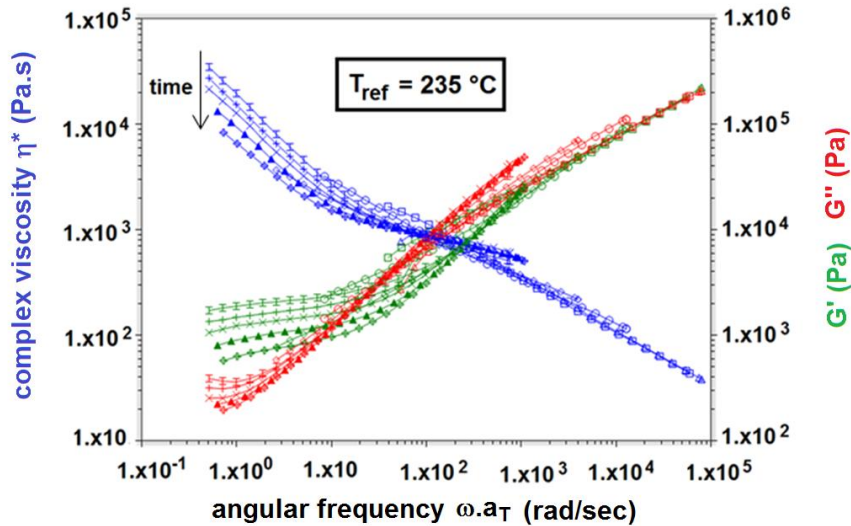
Figure 4.5: Master curve of PA6 (Ultramid B27). The measurements were performed over the temperature range between 222 and 250 °C. The viscosity decreases with a decreasing residence time of the polymer in the rheometer, particularly at lower frequencies.

Similar experiments were carried out with polypropylene (Moplen HP561R) at 200 °C. The results of the experiments in the capillary rheometer and the shear rheometer were consistent (Cox-Merz rule, see Figure 3.16).

The spinnability and the influence of the polymer topology on the melt spinning process were investigated for well defined polymers. The PS combs showed an increase in viscosity (Figure 3.12) during extension experiments (strain hardening). The polystyrene was spinnable [150], but the spun fibers were extremely brittle. This means that the fibers were not compatible with the Haul-off system. In order to have more flexible samples, blends of a triblock copolymer polystyrene-polyisoprene-polystyrene (PS-PI-PS, Kraton, PI = 90 wt%) and PS linear and PS combs were prepared for these fiber forming experiments using a mini-extruder (Minilab, Haake). For a blend of PS90/Kraton with a Kraton concentration of 5 wt%, the brittleness of the fibers was reduced enough that the fibers could be wound up with the Haul-off device.

Further spinning experiments were carried out with blends of polystyrene and Kraton using similar concentrations of the corresponding linear PS (PS90 and PS265) and comb PS (PS90-13-12 and PS90-4-42).

In order to compare the $DDR_{max}$ of these blends, the take-up speed was varied with a constant shear rate of 40 s$^{-1}$ ($D_{die}$ = 0.5 mm). The best results are provided by PS90-4-42 with a $DDR_{max}$ of 358 $\pm$ 61 (see Table 4.1). The linear PS samples were very instable during melt spinning process. In general, the PS combs are sown better spinning properties. The filaments of PS90-4-42 were very fine with the diameter of ~ 32 $\mu$m.

Table 4.1: The $DDR_{max}$ of various polymer blends with 5 wt% PS-PI-PS ($\dot{\gamma}$ = 40 s$^{-1}$). PS90-4-42 shows the highest ratio despite the lower temperature. The experiments were repeated five times and the mean values were reported.

|  | PS90 | PS265 | PS90-13-12 | PS90-13-12 | PS90-4-42 |
|---|---|---|---|---|---|
| T [°C] | 220 | 220 | 220 | 200 | 200 |
| $V_{max}/V_0$ | 28 $\pm$ 13 | 31 $\pm$ 15 | 103 $\pm$ 26 | 58 $\pm$ 19 | 358 $\pm$ 61 |

## 4.8  Detection of mechanical instabilities inside a die
### 4.8.1  Slit die

Capillary flow measurements were carried out in a capillary rheometer (Rheo-tester 2000, Göttfert) using a non-conventional slit die (0.2 x 2 x 20 mm$^3$)  (Figure 4.6 and 4.7) in order to realize the measurements in the range of the high shear rates used fiber spinning (e.g. the shear rates up to 9000 s$^{-1}$)
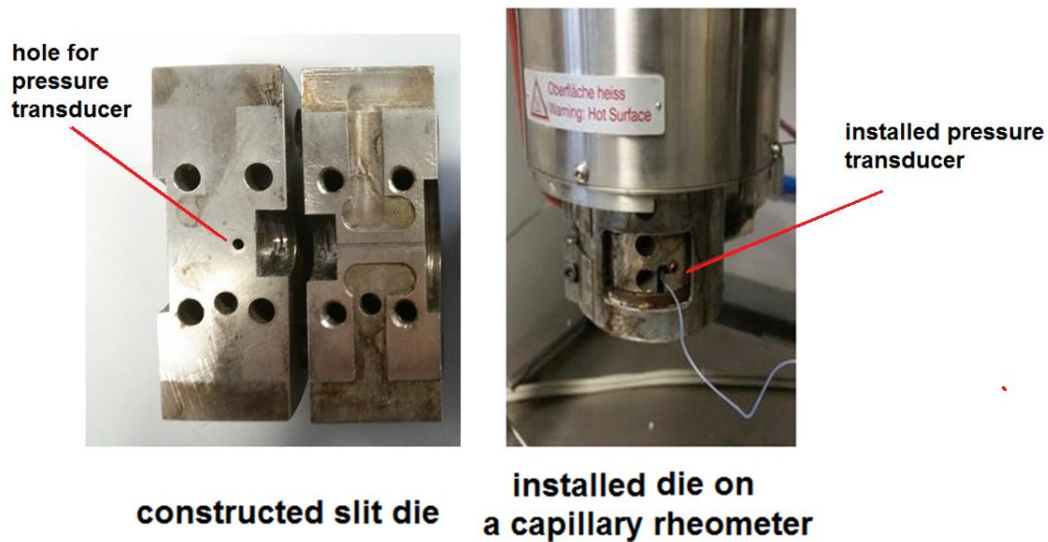
Figure 4.6: Left: cross section of slit die (0.2 x 2 x 20 mm$^3$) with a piezoelectric pressure sensor. Right: picture of a slit die with a pressure transducer (model 6183, KISTLER, Germany). The die installed in the capillary rheometer.
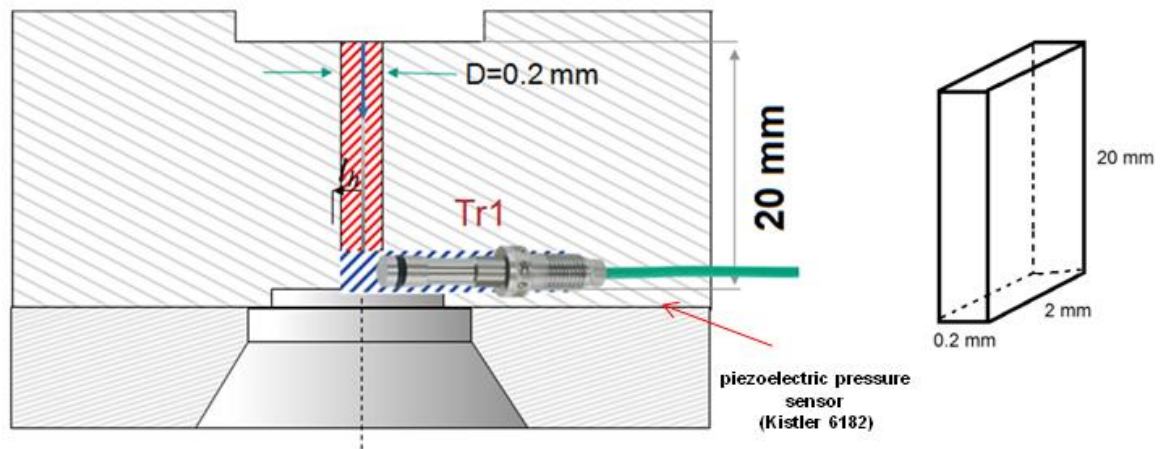


Figure 4.7: Technical design of a slit die 0.2 x 2 x 20 mm equipped with a piezoelectric transducer.

The die is equipped with a high sensitivity piezoelectric pressure transducer (model 6183, KISTLER, Germany) with a front diameter of 1.0 mm. The transducer is capable of delivering pressure resolution of 1 ms and 5x10$^{-3}$ bar at a nominal pressure of 2000 bar. By using this pressure sensor, we are able to measure local pressure fluctuations inside the constructed slit die. The Fourier analysis of the time dependent pressure data allows to find characteristic frequencies, which are the inverse of the related time scale of the instabilities [160, 161].

Different commercial polymers were studied in this section. The polymers with good spinnablity properties show no visible instabilities, even at higher shear rates (e.g. iPP, ~ 2000 s$^{-1}$, $D_{die}$ = 0.5 mm, T = 180 °C).

Two samples of elastomeric polyolefins, Engage 8100 ($M_n$ = 26.5 kg/mol, Đ = 1.85) and 8200 ($M_n$ = 21.6 kg/mol, Đ = 1.62) from DOW chemicals were investigated in this study. These two polymers show poor spinnability, and characteristic instabilities at moderate shear rates (~ 100 - 600 s$^{-1}$). Figure 4.8 shows the images of the instabilities of these two samples at different shear rates. The polymer Engage 8200 shows less instability compared to Engage 8100 at the same shear rate.
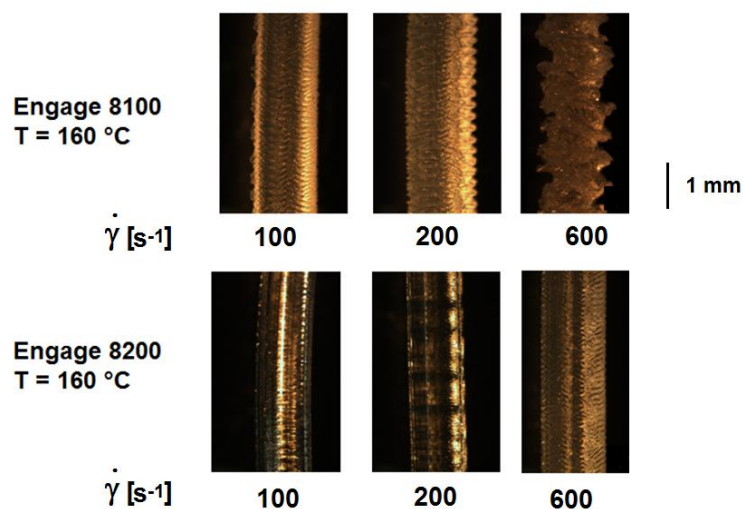


Figure 4.8: Images of the instabilities of Engage 8100 and 8200 at different shear rates and T = 160 °C. The polymer Engage 8200 shows less instabilities compared to Engage 8100 at the same shear rate.

The melt flow instabilities can also be analyzed by the Fourier transformation of the gray-scale intensities of the images of the extrudate. To confirm of the data analysis of the time-dependent pressure signal from the piezoelectric pressure transducer, the image analysis was performed using MATLAB. An example Figure 4.9 shows the image analysis and the Fourier transformation of the time-dependent pressure for a sample of Engage 8100 at 160 °C and a shear rate of 600 s$^{-1}$. The melt flow instabilities of the polymer extrudate from both image analysis (the peaks at 55, 67 and 141 Hz) and the Fourier transformation spectrum of the pressure fluctuations (the broad peaks at 35, 67 and 105 Hz) are shown in Figure 4.9.
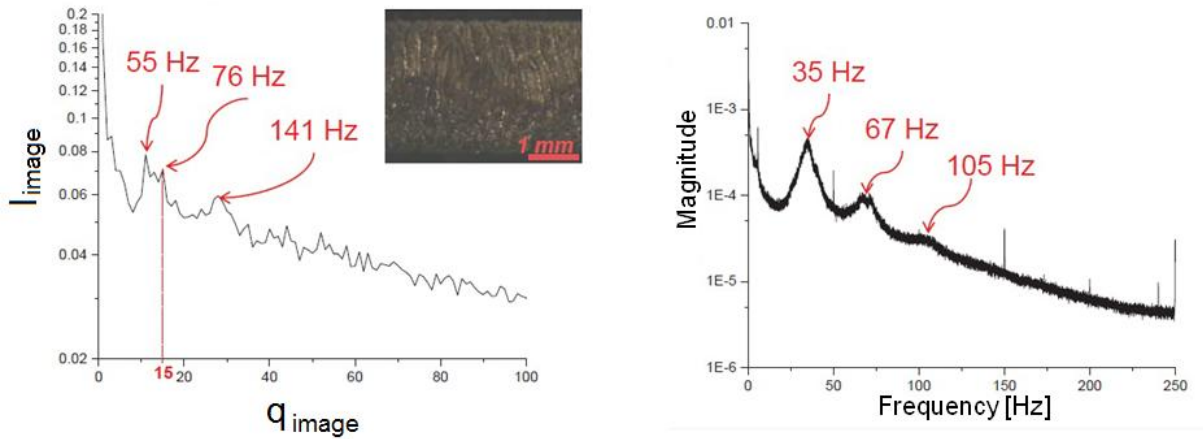
Figure 4.9: Left: Image analysis of the instabilities with MATLAB ($q_{image}$: number of waves), right: the data analysis of the time-dependent pressure from the piezoelectric pressure transducer inside the slit die for the sample Engage 8100 at 160 °C and a shear rate of 600 s$^{-1}$.

### 4.8.2 Round die

A new round die was designed and constructed for melt spinning purposes (Figure 4.10). The round die is equipped with the same piezoelectric force transducer to detect instabilities inside the die.
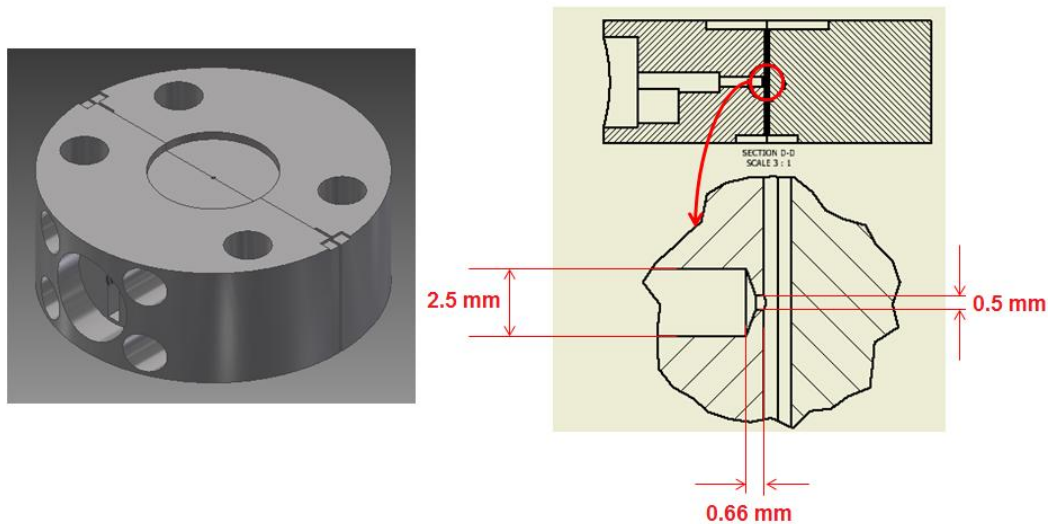


Figure 4.10: Sketch and technical design of a round die $D$ = 1 mm equipped with a piezoelectric transducer.

The spectra in Figure 4.11 shows the Fourier transformation analysis of the time-dependent pressure fluctuations of Engage 8100 at 160 °C and two shear rates of 200 and 600 $s^{-1}$.
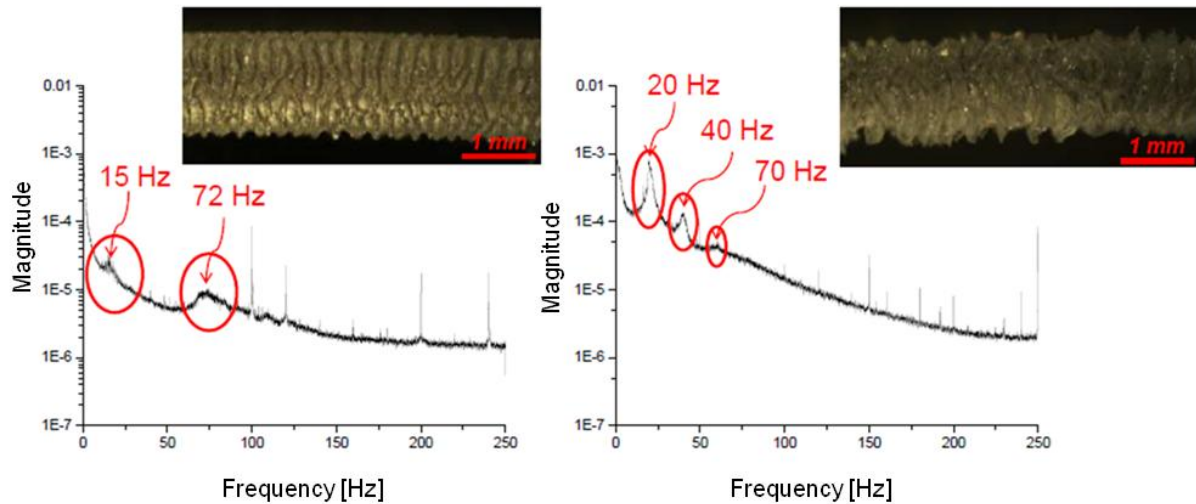


Figure 4.11: Fourier transformation analysis of the time-dependent pressure fluctuations and the corresponding images of Engage 8100 at 160 °C and two shear rates of 200 and 600 $s^{-1}$.

The broad peaks indicate the melt flow instabilities of the polymer at two different shear rates as directly determined via capillary flow.

## 4.9  Conclusions

In this chapter we used the definition of the maximum draw-down ratio ($DDR_{max}$) as a parameter to compare the spinnability of two different polymers (see Table 4.1). The well defined linear and comb PS samples were spun with a constant shear rate of 40 $s^{-1}$ and different take-up speeds.  In general, the PS combs show better spinning properties in the melt state than the linear samples. In the next step, two sharkskin dies were designed and constructed. Each of these dies was equipped with a piezoelectric pressure transducer to detect instabilities inside the die.

The melt flow instabilities were analyzed first by the Fourier transformation of the intensities of the images of the extrudate and then by the Fourier transformation of the signals of pressure transducer. The melt flow instabilities from both methods are in agreement with each other in number of instability related peaks.

# 5 Electrospinning of model polymers - Detection of instabilities

## 5.1. Electrospinning process and background

Several advanced techniques have been developed for the preparation of 1D nanostructures since the 1990s (e.g. electron-beam or focused-ion-beam writing, lithography, hydrothermal, chemical vapor deposition, electrospinning) [162, 163]. Among these methods, electrospinning, as the simplest and cheapest method to fabricate 1D nanostructures, attracts significant attention.

The process has its origin in the studies on electric fields initiated by Lord Rayleigh in the nineteenth century. Lord Rayleigh calculated the minimum charge for a drop to overcome its surface tension and create a liquid jet under an electric field [164]. Electrospinning from solution was first patented by J. F. Cooly in 1900 [165]. In 1934 there were further developments toward commercialization by A. Formals for the production of textile yarns [143]. Electrospinning from the melt was patented by C. L. Norton in 1936 [166]. The first technical application of electrospinning was suggested for the nonwoven industry. Before the 1990s electrospinning did not attract considerable scientific attention. In the early 1990s several research groups (notably Reneker [167, 168], who popularized the name of electrospinning for this process) demonstrated that many organic polymers could be electrospun into nanofibers. Since then, the number of research groups who entered the field of electrospinning quickly increased, which resulted in a dramatic increase in the number of publications (Figure 5.1).
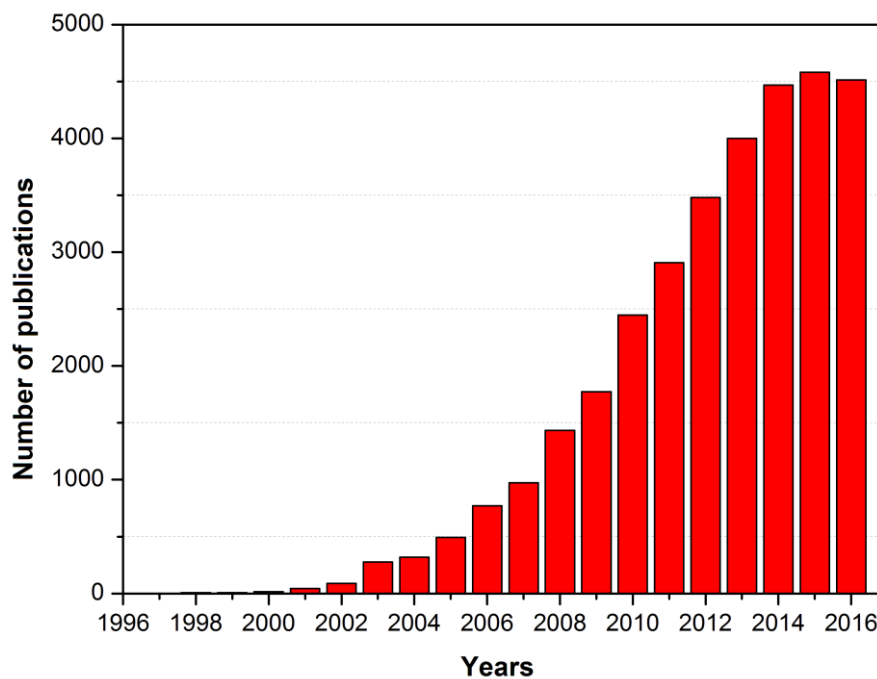
Figure 5.1: Number of scientific publications on electrospinning from 1996-2016, based on a SciFinder Scholar search using the keyword "electrospinning" (18.01.2017).

Nowadays, electrospinning is the most effective technique to process polymer solutions or melts into continuous fibers with an average diameter that ranges between 10 nm and 10 $\mu$m [22, 169]. This fiber spinning method has the advantage of using only minimum amounts of polymers and consequently is ideal for self synthesized well-defined systems.

Nanofibers are defined as one dimensional nonmaterials with diameters less than 1 $\mu m$, and aspect ratios (length/diameter) larger than 100. This special characteristic offers them a drastically increased surface to mass (or volume) ratio and makes nanofibers very useful in a wide range of advanced applications [170] such as filtration [171, 172], catalysis [173], protective clothing [174], sensors [175], drug delivery and tissue engineering [176-181]. The need for clean water and air is an ever growing challenge for modern societies. To solve this environmental problem, nanofibrous membranes were widely studied in the field of air and water filtration. Companies such as Donaldson and Freudenberg have been using electrospun nanofibers for the last two decades in their air filtration products [24].

Compared with other one dimensional nanostructures (e.g. nanotubes or nanorods), nanofibers have the advantages of lower fabrication costs and the possibility to

integrated the fibers into the final product in one step. Figure 5.2 shows SEM images of fibers produced from solutions of poly (methyl methacrylate) (PMMA) in DMF as an example of electrospun nanofibers compared to a normal human hair which typically has a diameter around 60 micrometers.
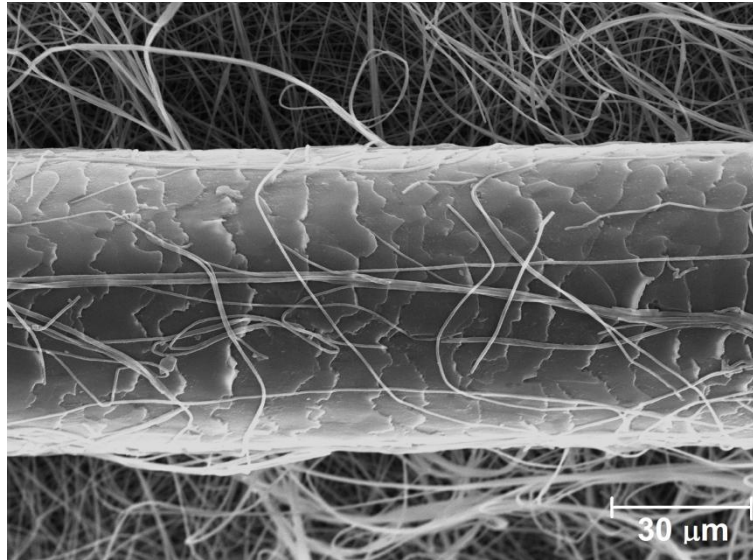


Figure 5.2: Size comparison of PMMA ($M_n$= 200 kg/mol, Đ = 1.2) nanofibers electrospun from DMF solution and a normal human hair.

## 5.2. Electrospinning setup

In electrospinning, an electrostatic force produced by a high voltage supply is used to drive the spinning process. The process can be conducted vertically or horizontally and the liquid may be a solution or a melt. The basic horizontal solution eletrospinning setup used in this work is shown in Figure 5.3. It consists of a holding container for the polymer solution, a metering pump, a high voltage power supply able to deliver about 5-30 kV (DC) with a required current, that is well below the microampere range [22, 163], a capillary tube or needle, and a collector (e.g. an aluminum foil) positioned opposite to the tip of the syringe at a distance of a few centimeters.
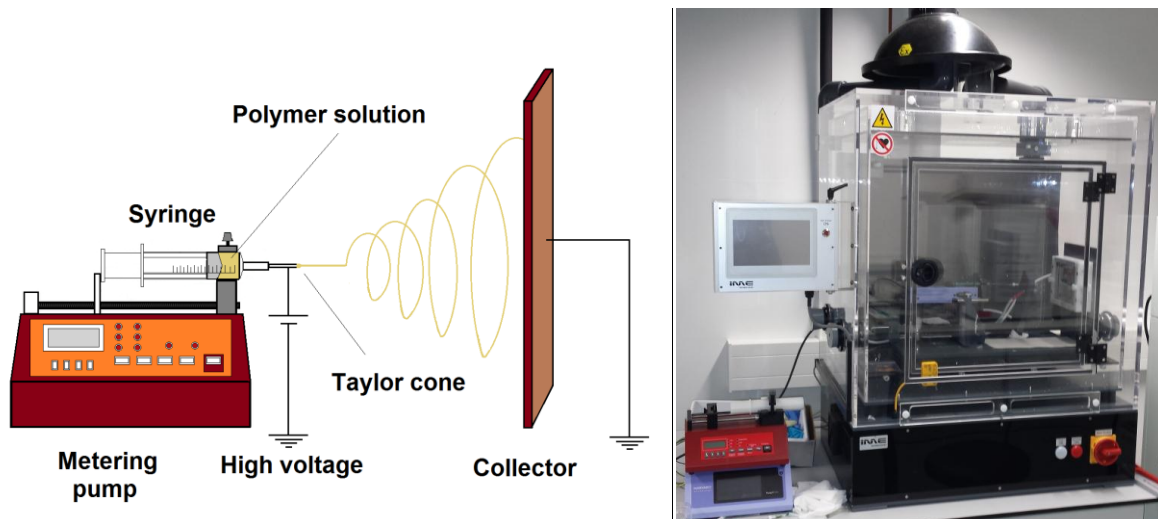
Figure 5.3: left: schematic diagram of a horizontal type electrospinning setup. right: electrospinning unit (KIT, Germany) used within this thesis.

The metering pump is normally a syringe driver, which is suitable for a small amount of fluid. The piston pushes against the syringe at a given velocity so that a specified volume is discharged per unit time. The capillary tube is normally the metal tip of a syringe connected to a high voltage potential. The collector is connected to the ground system as the counterelectrode. The applied electric field is typically in the range of 100 to 500 kV/m of direct current (DC). An alternating current (AC) generator can be used in electrospinning, but it is rarely chosen in the laboratory due to safety reasons. Electrospinning most commonly uses charged, moderately concentrated polymer solutions (*e.g.* 30-35 wt % solution of PS, $M_w$ = 190 kg/mol, in tetrahydrofuran) [182] or polymer melts [183, 184]. The applied voltage can cause the deformation of the droplet into a cone-shape protrusion (Taylor cone). With increasing voltage, the force acts in the opposite direction of the surface tension of the droplet, leading to its elongation. This tiny filament gives rise to evaporation of the solvent and fibers of small diameters.

Over 200 types of materials including natural and synthetic polymers can be electrospun into nanofibers [22]. Due to solubility problems, polymers like polyolefins, polyamides and polyethylene terephthalate are preferentially electrospun from the melt [185]. The previously majority of electrospun fibers are typically fabricated from polymer solutions. It was found that the morphology of electrospun fibers depends on three main groups of parameters [186, 187]. The first group of parameters is based on the solution properties, e.g. viscosity, concentration, conductivity, elasticity and

surface tension, where each of these properties depends on the choice of solvent and the molecular characteristics of the polymer under investigation including the monomer type, molecular weight, dispersity and molecular topology. The second group of parameters are the selected processing conditions in electrospinning, e.g. the applied voltage and the distance between the needle and collector and solution flow rate. The last group of parameters affecting the morphology of the electrospun fibers are the selected ambient conditions inside the electrospinning apparatus, which includes the temperature, humidity and atmospheric pressure (see for example [188-190]).

The process of jet formation in electrospinning relies on the entanglement of polymer chains [182, 191].  An increase in polymer concentration results in different morphologies of electrospun products: beads, beads and fibers (beads-on-string) and uniform bead-free fibers (Figure 5.4).
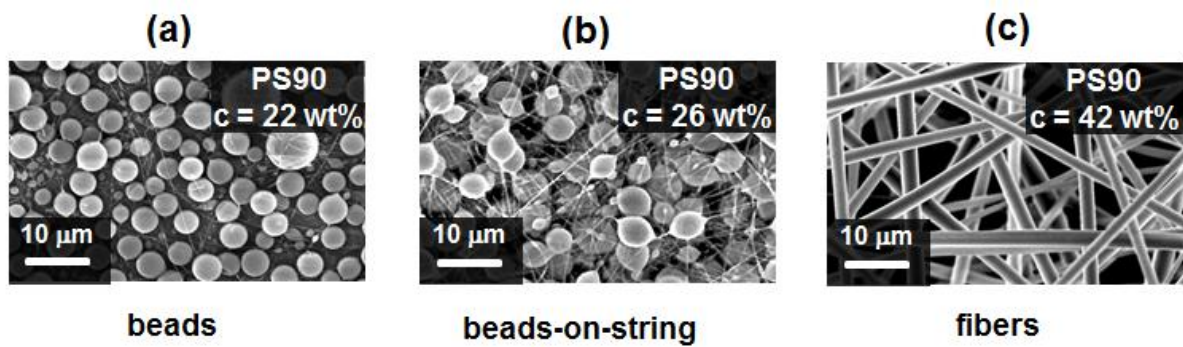


Figure 5.4: Scanning electron micrographs of electrospun linear PS ($M_w = 95$ kg/mol, $Đ = 1.05$) in DMF. As the concentration is increased, the morphology consists of: (a) beads, (b) beads-on-string and (c) uniform fibers. The corresponding solution concentrations are indicated.


## 5.3.    Control of fiber morphology and solution properties

A systematic approach to the electrospinning of polymer solutions at different concentration regimes is relevant to understanding the process of fiber formation. The Huggins equation describes the concentration dependency of the viscosity for a homogeneous linear polymer solution:

$$\eta_{sp}(c) = [\eta] \cdot c + k_H([\eta] \cdot c)^2 + \cdots \qquad (5.1)$$

$$\eta_{sp} = (\eta_0 - \eta_s)/\eta_s$$

where $[\eta]$ is the intrinsic viscosity, $\eta_{sp}(c)$ is the specific viscosity, c is the polymer concentration, $\eta_s$ is the solvent viscosity, , $\eta_0$ is the zero shear viscosity and $k_H$ is the

Huggins coefficient [187]. The dimensionless quantity $[\eta] \cdot c$ is referred to as the Berry number ($B_e$) [192]. In a dilute solution, polymer chains do not interact, and $B_e < 1$. For semi-dilute solutions, $B_e > 1$. As shown schematically in Figure 5.4 at the critical crossover concentration ($c^*$), polymer chains begin to overlap. The value of the critical chain overlap concentration $c^*$ can be experimentally determined from intrinsic viscosity measurements via equation 5.2 and depends on the chemical structure of the polymer, average molecular weight of polymer, temperature and the nature of the solvent.

$$c^* \sim \frac{1}{[\eta]} \qquad (5.2)$$

In dilute solutions, the solution viscosity is proportional to the concentration ($\eta \sim c$) for good solvents [193]. Based on the De Gennes scaling concept, the power law dependency of the predicted specific viscosity increases with increasing polymer concentration. For $c > c^*$ a power law dependence of the following form is expected [194, 195]:

$$\eta \sim \eta_s M^3 \left(\frac{c}{c^*}\right)^{3/(3v-1)} \qquad (5.3)$$

where $\eta_s$ is the solvent viscosity, $M$ is the molecular weight of the polymer and $v$ is the Flory exponent, which has a value of 0.5 for theta solvents and about 0.6 for good solvents.

Consequently in good solvents this single parameter scaling model predicts a concentration exponent of 3.75. Experimental studies revealed that the actual exponential dependence of the viscosity on the molecular weight varied slightly from the expected value of 3 ($\eta \sim M^{3.4}$), which leads to an overall exponent value of 4.5 for the viscosity dependence on concentration ($\eta \sim c^{4.5}$), which corresponds well to the experimentally measured value of 4.8 [187, 196].

Colby and coworkers presented two different power law dependencies for the viscosity on concentration within the semidilute concentration regime (Figure 5.5), which were semidilute unentanglened and semidilute entangled [196]. The crossover of concentration from semidilute unentangled to semidilute entangled is called the entanglement concentration $c_e$.

For a polymer in a good solvent the predicted concentration exponent for the semidilute unentangled regime is 1.25, i.e. $\eta \sim c^{1.25}$, which is in good agreement with experimental values that are within the range of 1.1-1.4 [187, 191]. All these values are with respect to linear polymers and at equal molecular weights; however branched polymers show a different type of behavior in solution.
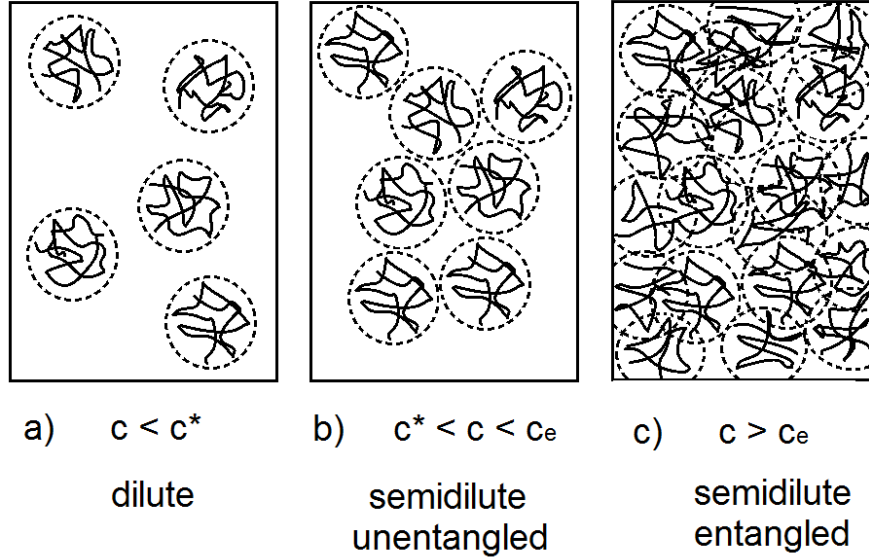


Figure 5.5: Three different concentration regimes a) dilute, b) semidilute unentangled and c) semidilute entangled for polymer solutions in a good solvent [187, 191].

Chain entanglements can significantly influence fiber formation during solution electrospinning. In the melt state at low molecular weights, there are no chain entanglements, $\eta_0 \sim M^1$. Above a critical molecular weight $M_c$ this relation changes to $\eta_0 \sim M^\alpha$, where $\alpha$ is usually in the range of $3.5 \pm 0.2$ [104, 113]. The ratio of $\frac{M_c}{M_e}$ corresponding to the number of entanglements $n_e$, has a theoretical value of 2, however, a number between 1.7 and 3 [113] was experimentally found. Shenoy et al. [182] defined the solution entanglement number $(n_e)_{soln}$ according to Equation 5.4:

$$(n_e)_{soln} = \frac{M_w}{(M_e)_{soln}} = \frac{(\phi_p M_w)}{M_e} \qquad (5.4)$$

where $M_w$ is the weight average molecular weight, $\phi_p$ is the polymer volume fraction and $(M_e)_{soln}$ is the entanglement molecular weight in solution.

Similar to the polymer melts, above a critical molecular weight $(M_c)_{soln}$ the zero shear viscosity shows a sharp upturn, when $(M_c)_{soln}/(M_e)_{soln}$, has the value of 2-3. This is reasonable because the solution concentration is well above the dilute solution regime.

For solution electrospinning, an increase in polymer concentration results in the following structure: (1) beads only, (2) beads and fibers (beads-on-string) and (3) uniform fibers. The beaded fibers (beads-on-string) formed at $(n_e)_{soln}$ values of 2 and for $(n_e)_{soln}$ values above 3.5, uniform fibers [182] were produced. Gupta et al. [187] reported the formation of fibers from PMMA solutions in DMF for polymers ranging from $M_w$= 13 to 366 kg/mol. Bead-free fibers were obtained from low dispersity PMMA (Đ = 1.03-1.35) were obtained, when normalized concentration c/c* had a value higher than 6, which is in the so-called semidilute entangled regime. For samples with a broader distribution (Đ = 1.62 and 2.12), bead-free fibers were obtained at values of c/c* that were over 10.

Solutions of branched polymers show scaling law concentration dependent transitions in viscosity. McKee et al. [191] studied the fiber morphology and solution rheological behavior of linear and branched poly(ethylene terphthalate-co-ethylene isophthalate), PET-co-PEI from a 70/30 w/w CHCl$_3$/DMF solution. They showed that the entanglement concentration, $c_e$, is the minimum concentration required for the formation of beaded fibers and that concentrations of at least 2 - 2.5 times the entanglement concentration (2 - 2.5 x $c_e$) were necessary for the formation of bead-free fibers. Below $c_e$ the polymer solutions yielded only droplets. However, McKee controlled the branching content and topology using three different branching agents with three functional groups and different concentrations of the branching agent. These branched samples had a broad dispersity (Đ = $M_w/M_n$ = 2.4) for polymers with low levels of branching and a very high dispersity of Đ = 10.7 for polymers made with a higher concentration of the branching agent. A common approach for characterization of branched polymers was first theoretically developed by Zimm and Stockmayer [97], and is based on the assumed contraction of the polymer chain relative to the size of their linear analogues of the same molecular weight. This contraction is expressed by the index of branching or contraction factor (see Table 2.1 and Equation 2.4 and Equation 2.5), $g = \langle R_g^2 \rangle_{br} / \langle R_g^2 \rangle_l$, which is the ratio of the mean squared radii of gyration of the branched and linear molecules where the linear

molecule has the same molecular weight. Analogous to this definition, the decrease in the intrinsic viscosity of a branched molecule can be used to quantify the level of branching. McKee et al. quantified the branching level using the rheological contraction factor [97, 191, 197-199], $g' = [\eta]_{br}/[\eta]_l$ where $[\eta]$ is the intrinsic viscosity and the indices $br$ and $l$ denote the branched polymer and the corresponding linear polymer of the same total molecular weight, respectively. This contraction factor was correlated with the entanglement concentration, $c_e$, in solution [191, 197].

The scaling relationship between viscosity and concentration in the semidilute regime for well defined model polymers was investigated. Solution rheology was used to characterize solutions of two linear and three comb PS samples over the concentration range suitable for electrospinning. The viscosities of the solutions under steady shear flow were investigated using steady shear rate sweeps between 1 and 2000 s$^{-1}$ at 25 °C. All solutions (linear and comb) showed nearly Newtonian behavior over this range of shear rates, although it is expected that shear thinning behavior will eventually occur for the more concentrated solutions at higher shear rates. Figure 5.6 shows the steady shear viscosity of PS90-4-42 solutions as a function of the shear rate for different concentrations.
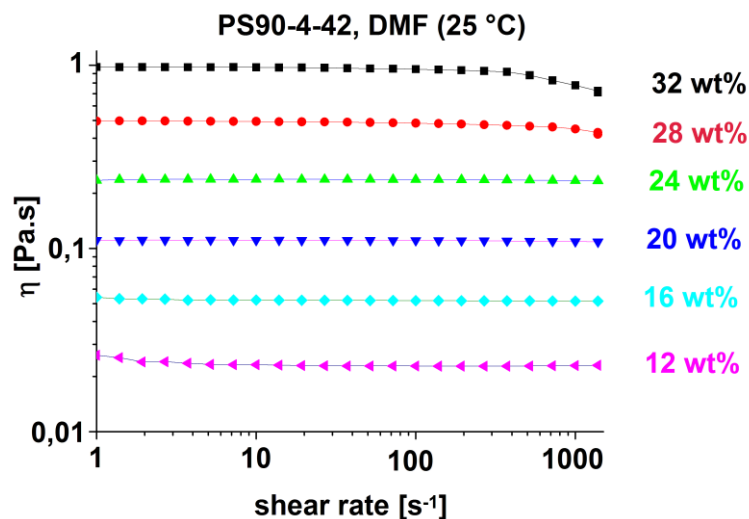


Figure 5.6: Viscosity of PS90-4-42 solutions in DMF as a function of the steady shear rate at 25 °C. The measurements were performed using ARES-G2 rheometer equipped with a Couette. The results were used in Figure 5.7.

Zero shear viscosities, $\eta_0$, were approximated from the flow curves using extrapolated values for shear rates between 10 and 100 s$^{-1}$. As expected, increasing the polymer concentration yielded solutions with higher zero shear viscosities. At a fixed concentration (wt %), the following trend was found: $\eta_0^{PS90} < \eta_0^{PS90-13-12} < \eta_0^{PS90-5-30} < \eta_0^{PS90-4-42} < \eta_0^{PS265}$. These values for $\eta_0$ were used to calculate the specific viscosity, $\eta_{sp} = (\eta_0 - \eta_s)/\eta_s$, where $\eta_s$ is the solvent viscosity ($\eta_s$ = 0.802 mPa.s for DMF at 25 °C) [200].

For a linear polymer in a good solvent, these dependencies are $\eta_{sp} \sim c^{1.0}$, $\eta_{sp} \sim c^{1.25}$ and $\eta_{sp} \sim c^{4.8}$ for the dilute, semi-dilute unentangled and semi-dilute entangled regimes, respectively [191]. The crossover concentration, $c_e$ (critical entanglement concentration), represents the minimum concentration required for electrospinning of beaded nanofibers [182, 191] and is the concentration where the polymer chains are entangled in the solution and form continuous fibers during electrospinning.

To determine these concentration regimes for the PS combs, the specific viscosity data were plotted as a function of the polymer concentration (Figure 5.7). Within the range of suitable concentrations for electrospinning, two different power law dependencies were found for the combs. At low concentrations, the scaling exponent was nearly 2.8 and, at high concentrations, the exponent reached the expected value of 4.8. Figure 5.7 shows that all the crossover concentrations, for the combs, $c_{e,comb}$, were lower than that for linear PS90 and that of all the combs PS90-4-42 had the lowest crossover concentration at $c_{e,comb} \approx 18$ wt %. These values were different from the theoretical values predicted for linear PS in DMF [201] because of the branched architecture of the combs. One important result is that the plots of the solution viscosity as a function of $c \cdot (\frac{M_w}{M_e})^{0.5}$ for both the linear PS samples, PS90 and PS265 collapse onto a single curve after appropriate rescaling via $(\frac{M_w}{M_e})^{0.5}$ (Figure 5.7d). This is in agreement with the Huggins-equation or its modification [202, 203], where the specific viscosity is a function of the dimensionless quantity $c \cdot [\eta]$:

$$\eta_{sp} = B_1 c[\eta] + B_2 (c[\eta])^2 + B_n (c[\eta])^n \qquad (5.5)$$

where $n = 3.4/\alpha$. With respect to the MHKS equation, $[\eta] = KM^\alpha$, and Equation 5.5, a mastercurve for $\eta_{sp}$ as a function of $c \cdot (\frac{M_w}{M_e})^\alpha$ is proposed. Here $\alpha$ was found to be

nearly 0.5 in the mastercurves for both PS90 and PS265 and the concentration dependency of $\eta_{sp}$ at high concentrations is nearly $n \approx 6$ (Figure 5.7d).
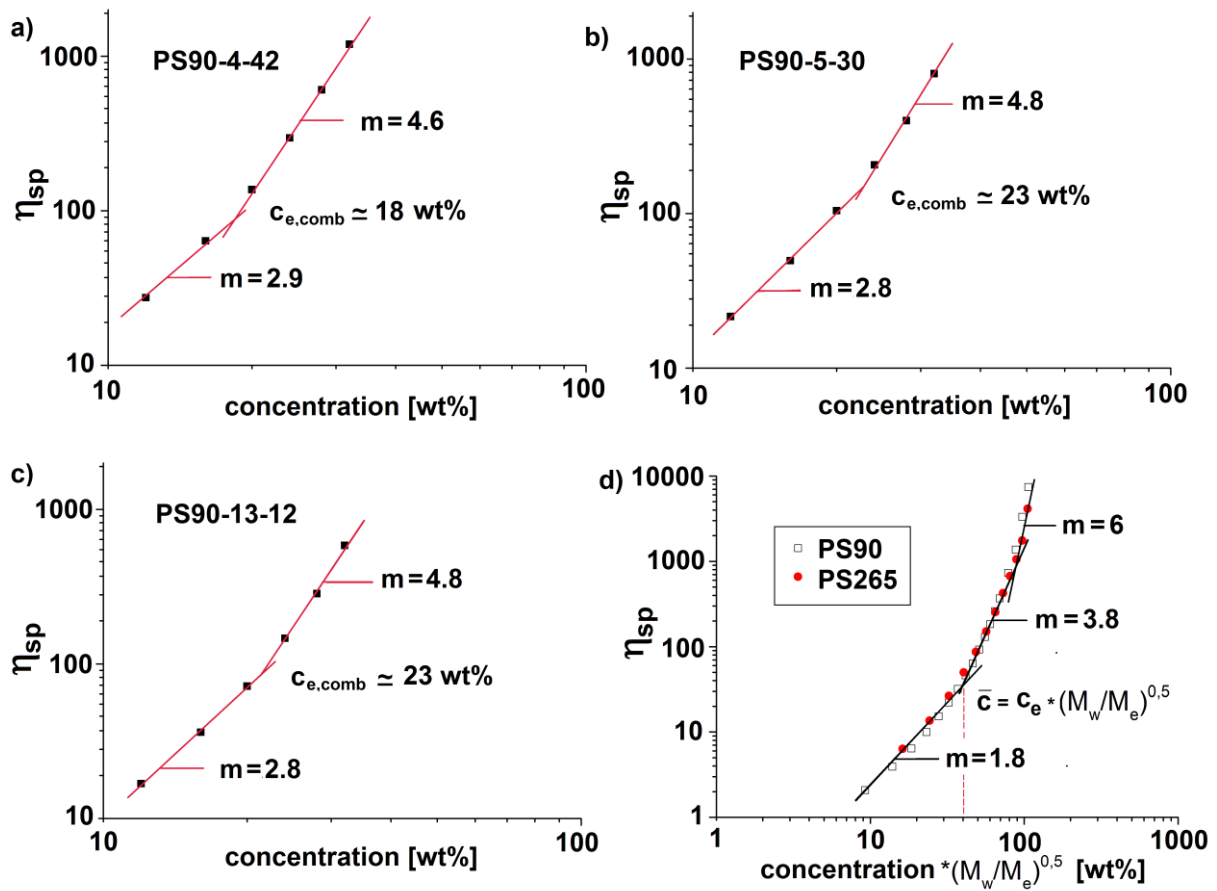


Figure 5.7: Specific viscosity of the polymer solutions as a function of concentration for three comb samples (a)-(c) and as a function of $c \cdot \left(\frac{M_w}{M_e}\right)^{0.5}$ for linear PS samples (d) in DMF. Note: $c_e$ is the entanglement concentration for the linear samples, which depends on the polymer molecular weight, and $c_{e,comb}$ is the onset of entanglement for the combs (adapted from [93]).

## 5.4. Electrospinning of linear and comb topologies

A series of linear and comb PS solutions were electrospun using the apparatus shown in Figure 5.3 at the conditions described in the experimental section in Chapter 6. Even though DMF is a poorer solvent for PS than THF, the PS/DMF solution could be readily electrospun due to its relatively high dielectric constant ($\varepsilon_r = 37.06$) compared to that of THF ($\varepsilon_r = 7.47$) [204]. The high dielectric constant of DMF increases the relative forces applied to the fibers [205]. Wang et al. [201] used a concentration-molecular weight diagram of the viscoelastic regimes for PS in DMF to

predict the different concentration regimes for any given $M_w$ (figure 5.8). This diagram is useful for predicting the electrospun features of linear PS at a given $M_w$. As an example, for the linear sample PS265 ($M_w = 297$ kg/mol), the minimum concentration to form beaded fibers is predicted to be about 13 vol % (~ 14 wt %), and smooth fibers should be obtained at a concentration of 23 vol % (~ 25 wt %). The prediction for the minimum concentration to prepare electrospun fibers for linear PS90 ($M_w = 95$ kg/mol) solutions is about 40 vol % (~ 42 wt %).
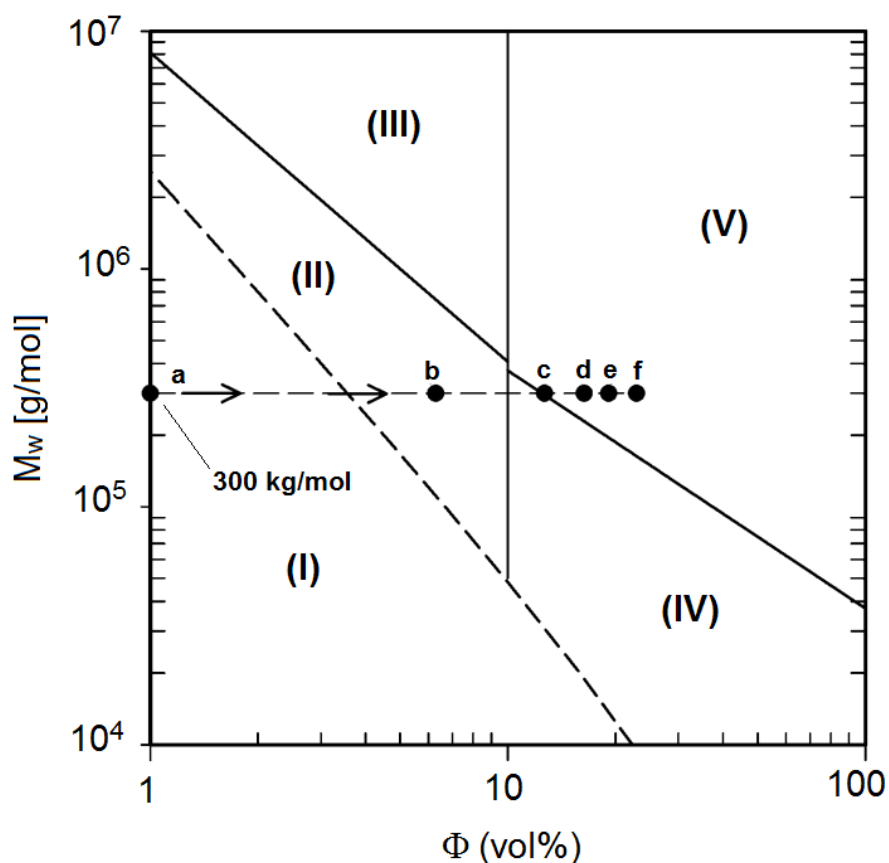


Figure 5.8: Concentration-molecular weight diagram of viscoelastic regimes for linear PS in DMF solvent. Several regimes can be identified: (I) dilute, (II) semidilute and not entangled, (III) semidiluted and entangled, (IV) concentrated and not entangled, and (V) concentrated and entangled. As an example, the concentration of a linear PS ($M_w = 300$ kg/mol) solution increases as shown by the arrow. The morphology of the electrospun product changes from beads (points a and b, 1-6 vol %), beaded fibers (points c-e, 13-19 vol %), and finally to smooth fibers (point f, 23 vol %) [201].

Our experimental results are in agreement with these predictions (see below). The beads to fiber transition for PS265 ($M_w = 297$ kg/mol, Đ = 1.1) and PS90 ($M_w = 95$ kg/mol, Đ = 1.05) is shown in Figure 5.9. At concentrations below 22 wt % for PS90

and 12 wt % for PS265, the amount of chain entanglement is negligible, and consequently only polymer droplets were formed. As the concentration was increased between 22 wt % and 26 wt % for PS90 and between 8 wt % and 12 wt % for PS265, beaded fibers with the average fiber diameter of ~ 150 nm for PS90 and ~ 100 nm for PS265 were seen. Uniform, defect-free fibers for linear PS90 and PS265 were electrospun at concentrations that were about a factor of two higher, specifically at 42 wt % for PS90 and 22 wt % for PS265.
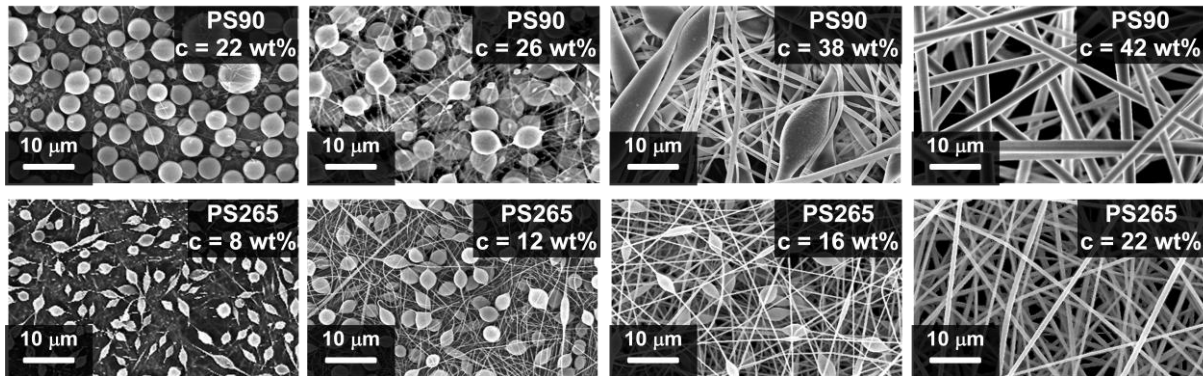


Figure 5.9: Scanning electron micrographs of electrospun linear PS90 ($M_w$ = 95 kg/mol, $Đ$ = 1.05) and PS265 ($M_w$ = 297 kg/mol, $Đ$ = 1.1) in DMF. The corresponding solution concentrations are indicated.

Solutions with a higher concentration of polymer yielded nanofibers with a larger average diameter. Figure 5.10 shows the dependence of the average fiber diameter for linear PS265 electrospun fibers on the zero shear viscosity $\eta_0$ of the corresponding solutions. The average fiber diameter increased with approximately the square root of the solution shear viscosity as indicated in Figure 5.10. It is interesting to note that this relationship holds for both the beaded fiber and fiber only regimes.
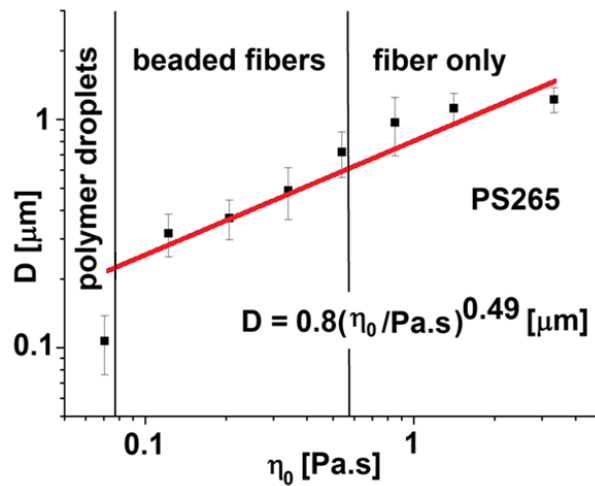
Figure 5.10: Dependence of the fiber diameter D on the zero shear viscosity $\eta_0$ for linear PS265 ($M_w$ = 297 kg/mol, $Đ$ = 1.1) where the three different regimes of fiber morphology are marked. The change for beaded fibers to fiber only cannot be determined via $D(\eta_0)$ (adapted from [93]).

The PS90-13-12, PS90-5-30 and PS90-4-42 combs all have a similar $M_w$. For a linear PS with a comparable $M_w$ (~ 250 kg/mol), the minimum concentration to have beaded fibers is predicted to be about 16 vol % (~ 17 wt %) and smooth bead-free fibers should appear at a concentration of 28 vol % (~ 30 wt %, which is 1.75 times the minimum concentration to form beaded fibers) [201].
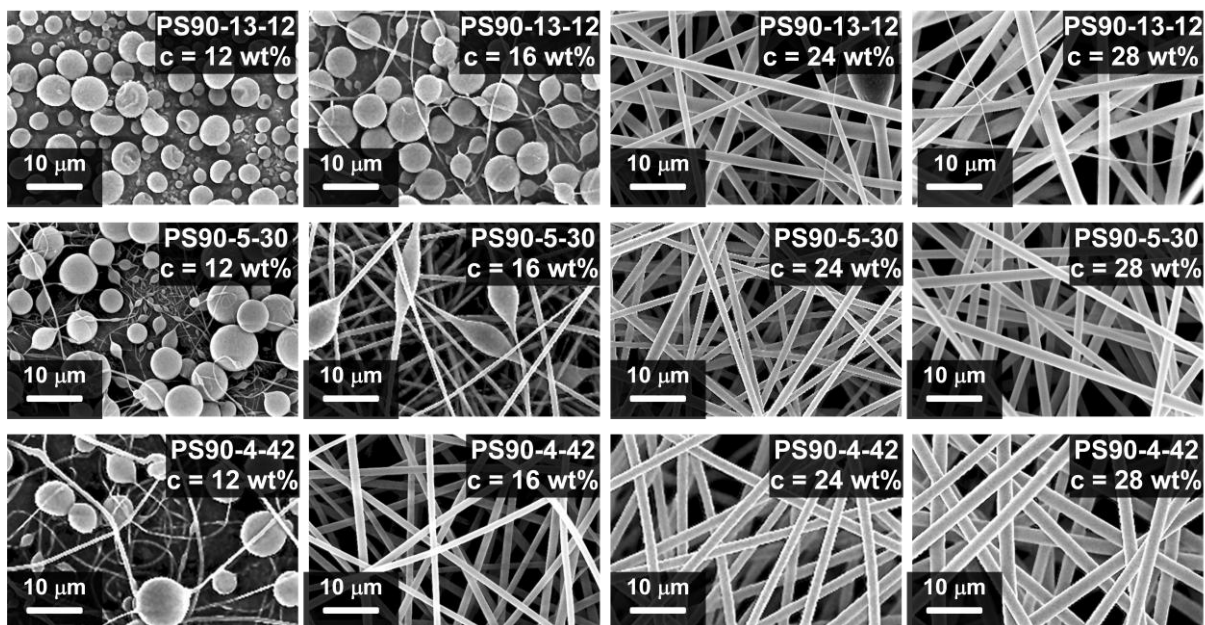


Figure 5.11: Scanning electron micrographs of electrospun PS90-13-12 ($M_w$ = 254 kg/mol), PS90-5-30 ($M_w$ = 253 kg/mol) and PS90-4-42 ($M_w$ = 251 kg/mol) combs in DMF. The corresponding solution concentrations are indicated.

Figure 5.11 shows images of fibers electrospun from 12 to 28 wt % solutions of the three different comb samples. PS90-13-12 ($g' = 0.46$, see Table 2.1), which has the highest number of branches ($N_{br} = 13$) and shortest side chains ($M_n = 12$ kg/mol, no physical entanglements per side chain in the melt state), showed morphological transitions at concentrations that were roughly similar to a linear PS with the same total $M_w$. For PS90-13-12, beaded fibers formed at a concentration of 16 wt % and bead-free fibers were obtained at 28 wt %. Fibers spun from solutions at concentrations equal to or higher than 28 wt % exhibited a bimodal distribution in the fiber diameter. For PS90-5-30 ($g' = 0.59$), the onset of beaded fibers occurred between 12 wt % < c < 16 wt % and bead-free fibers were formed when the concentration was greater than c = 24 wt %. For PS90-4-42 ($g' = 0.61$), which has the fewest branches ($N_{br} = 4$) and the longest side chains ($M_n = 42$ kg/mol, ~ 2 entanglements per side chain in melt state), beaded fibers started to form at a concentration of 12 wt % and bead-free fibers were obtained at 16 wt %. This was the lowest concentration investigated in this work. Table 5.1 summarizes the concentrations at which transitions from "beads only" to "beads-on-string" and "fiber only" morphologies formed for all electrospun linear and comb PS solutions [93].

Table 5.1: Summary of the beads-to-fiber transitions for all linear and comb PS samples. Bead-free fibers were even electrospun from a 16 wt% solution of PS90-4-42. Here it is important to note that the lowest concentration in this investigation for spinning fibers without beads was 16 wt% and this result is highlighted in yellow [93].

| Sample | molecular structure | $*M_w$ [kg/mol] | Beads only | Beaded fibers | Fiber only |
|---|---|---|---|---|---|
| PS 90-13-12 | comb | 254 | c < 20 wt % | 20 wt % < c < 28 wt % | c > 28 wt % |
| PS 90-5-30 | comb | 253 | c < 16 wt % | 16 wt % < c < 24 wt % | c > 24 wt % |
| PS 90-4-42 | comb | 251 | c < 12 wt % | 12 wt % < c < 16 wt % | c > 16 wt % |
| PS265 | linear | 297 | c < 8 wt % | 8 wt % < c < 22 wt % | c > 22 wt % |
| **PS90 | linear | 97 | c < 22 wt % | 18 wt % < c < 42 wt % | c > 42 wt % |

*Determined via SEC-MALLS, **PS90 used as the backbone for all comb samples

The dependence of the electrospun fiber diameter on the solution shear viscosity $\eta_0$ for comb samples is shown in Figure 5.12. In Figure 5.12, it can be seen that

electrospun fibers made from PS90-4-42 were more uniform (narrower standard deviation in the fiber diameter) than fibers made from other linear and comb samples. The diameter of the electrospun fibers increased as the viscosity increased according to a scaling law relationship, where the results for linear and comb samples are offset from each other, as shown in Figure 5.12d.
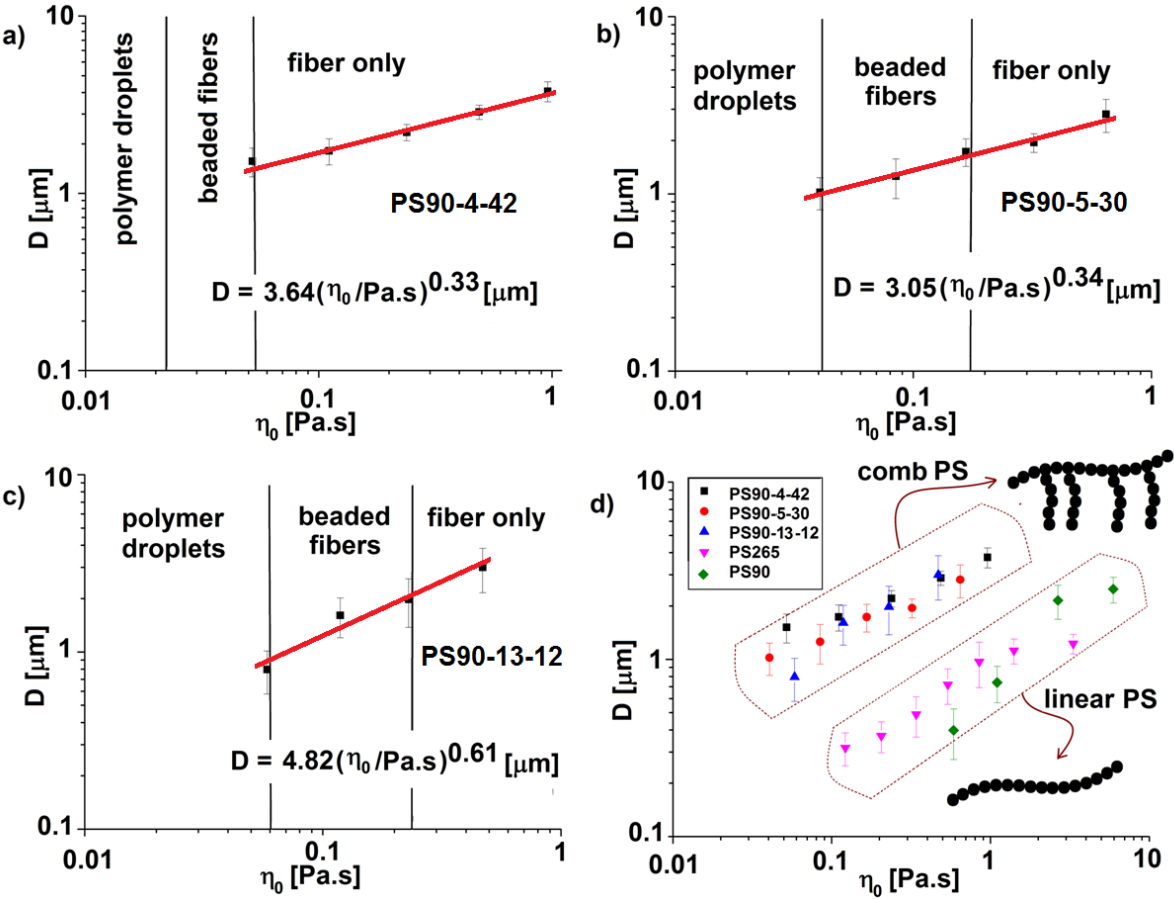


Figure 5.12: The dependence of the electrospun fiber diameter D on $\eta_0$ for solutions of PS comb samples a) PS90-4-42, b) PS90-5-30, c) PS90-13-12 and d) all PS samples together (linear and combs). The diameter of the electrospun fibers increased as the viscosity increased and the results for linear and comb samples as a function of viscosity are offset from each other (adapted from [93]).

Figure 5.13 shows the dependence of the average fiber diameter of the comb and linear electrospun PS samples on the shear viscosity $\eta_0$ at the minimum concentration at which bead-free fibers were first observed. This minimum concentration is important because the fiber diameter increases with the solution concentration. Comb polymers form bead-free fibers at lower viscosities and thus lower concentrations. For PS90-4-42, which had the longest side branches, there was a factor of 16 reduction in the viscosity and a factor of 1.4 reduction in the

concentration at which bead-free fibers formed relative to the linear PS265, which has the same total molecular weight as the comb.
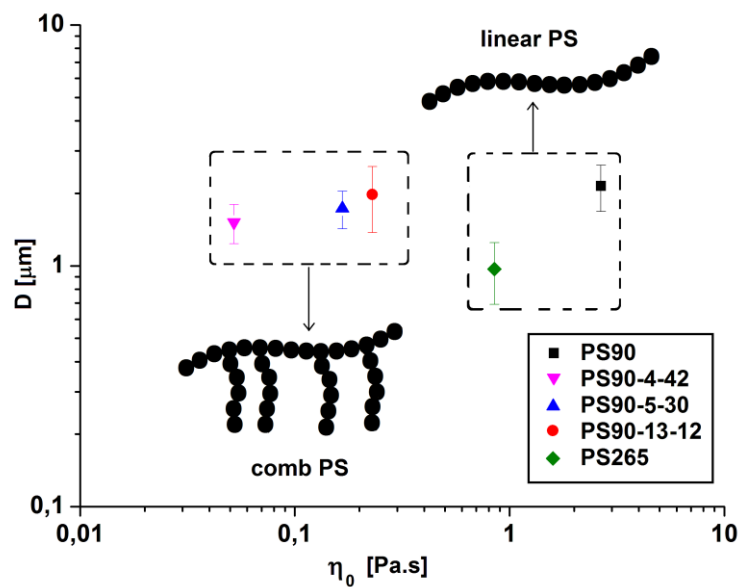


Figure 5.13: The dependence of the average fiber diameter of comb and linear electrospun PS samples on $\eta_0$ at the minimum concentration at which bead-free fibers are observed (adapted from [93]).

With respect to the effect of branch length on the morphological transitions, the reduction in viscosity for bead-free fiber formation with PS90-4-42 was an impressive factor of 41 lower relative to the viscosity at which this transition occurred for PS90. For combs with shorter branch lengths, the viscosity needed for bead-free fibers approached the same values as that for the linear polymers. All three combs generally formed fibers at lower viscosities and the fibers had larger diameters compared with the linear samples.
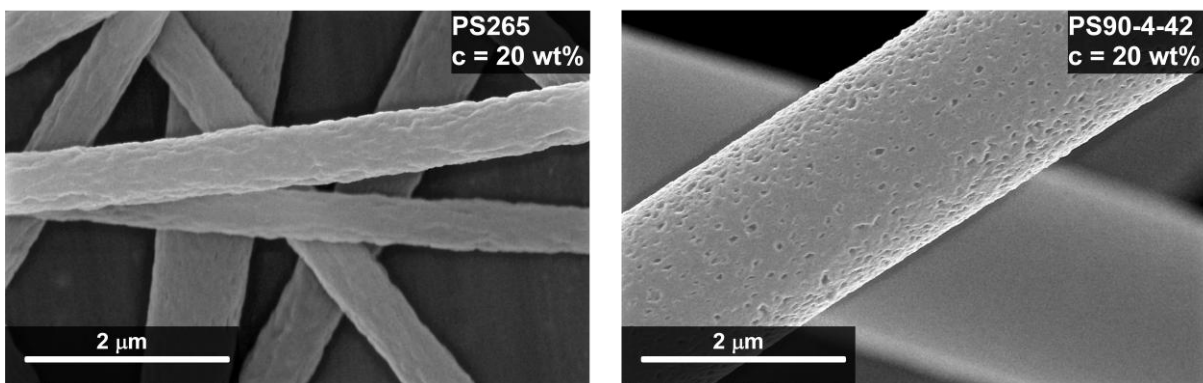


Figure 5.14: Scanning electron micrographs of electrospun PS265 and PS90-4-42.

Furthermore, comparing PS linear and comb fibers (Figure 5.14), the electrospun fibers made from linear PS265 were less uniform with more surface roughness and smaller fiber diameters. Fibers made from combs were more uniformly cylindrical and had smoother surfaces covered with small pores (Figure 5.14).

## 5.5 Capillary break-up extensional rheometry (CaBER) to predict spinnability

Extensional rheometry of polymeric solutions has been a subject of interest for many researchers for the last three decades. In the Capillary Break-up Extensional Rheometry (CaBER) experiment a very small amount of fluid (1-2 drops) is placed between two parallel plates (typically $D$ = 6 mm). The fluid is then exposed to a rapid, controlled extensional step strain. The upper plate moves in a fast, short (typically 20-100 ms) motion, thereby forming an "unstable" liquid bridge between the stationary lower plate and the upper plate (Figure 5.15). The mid-plane diameter of the filament, as the only measured quantity in this experiment, is determined via a laser sheet micrometer as a function of time, with the assumption that filament necking takes place mid-plane.
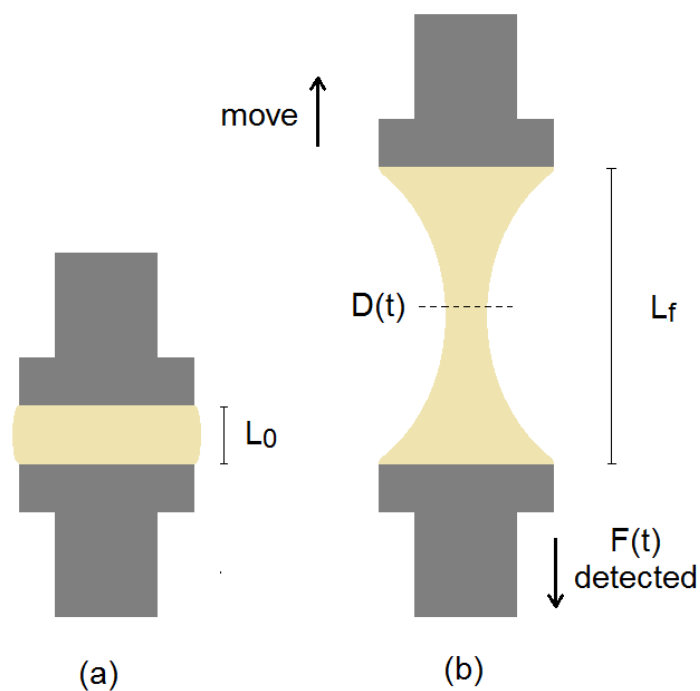


Figure 5.15: The steps of a CaBER experiment with a sample (a) before and (b) after stretching.

This allows for the determination of characteristic elongational flow properties such as the extensional relaxation time $\lambda_E$ and the apparent extensional viscosity $\eta_{E,app}$ [206].

The CaBER measurement starts after the upper plate has reached its final position $L_f$. The time evolution of the filament thinning for a viscoelastic fluid is controlled by the balance between capillary force, which trying to pinch off the filament and viscoelastic forces. For fluid samples the used final distance is normally in the range of 1 to 2 cm. The midpoint diameter, $D_{mid}(t)$, of the thinning filament can be described by the following model [207]:

$$D_{mid}(t) = D_0 \left(\frac{D_0 G}{4\gamma_{sol}}\right)^{1/3} e^{-t/3\tau_R} \qquad (5.6)$$

where $D_0$ is the midpoint diameter of the fluid filament immediately after imposition of a rapid step stretch in the axial direction, and $G$, $\gamma_{sol}$, and $\tau_R$ are the elastic modulus, surface tension, and viscoelastic relaxation time of the solution, respectively.

The Hencky strain, $\varepsilon$, the Hencky strain rate, $\dot{\varepsilon}$, and the apparent extensional viscosity of the solution, $\eta_{E,app}$, are defined as follows [206, 208, 209]:

$$\varepsilon(t) = 2ln\left(\frac{D_0}{D_{mid}(t)}\right) \qquad (5.7)$$

$$\dot{\varepsilon}(t) = 2\frac{dln\left(\frac{D_0}{D(t)}\right)}{dt} = \frac{-2}{D(t)}\left(\frac{dD(t)}{dt}\right) \qquad (5.8)$$

$$\eta_{E,app}(\dot{\varepsilon}, t) = \frac{\gamma_{sol}}{-\frac{d(D_{mid}(t))}{dt}} \qquad (5.9)$$

The important flow instabilities present in the electrospinning process, such as formation of beads, beads-on-string and fibers, can be followed during capillary thinning experiments performed on CaBER. An increase in the concentration of a polymer solution increases the characteristic relaxation time, due to the entanglement of the polymer chains in solution. There is a correlation between the characteristic relaxation time of the solution and the formation of beads or fibers during the electrospinning process [210]. Chen et al. [211] used the dimensionless Deborah number, $D_e$, which is defined as the ratio of the solution relaxation time over the

Rayleigh instability growth time. To characterize the spinabillity of cellulose acetate and poly(ethylene oxide) blends in DMF. It was found that uniform fibers were produced when of $D_e$ > 7. The formation of beads-on-string structures in the capillary thinning of filaments and jets has been investigated extensively and was reported to be primarily caused by either inertia or elasticity [212-215].

## 5.6 Measuring separation energy of a polymer solution with the CaBER

A CaBER instrument from Thermo Fisher Scientific was used to determine the extensional properties of fluids and solutions by measuring the diameter of a stretched fluid filament, which decreased the capillary force as a function of time. The characterization of fluids based on Equation 5.9 might be helpful, but for the determination of the true elongational viscosity from CaBER experiments, it is necessary to measure the time dependent axial force F during filament thinning accurately. Klein et al. [216] installed a highly sensitive commercial piezoelectric transducer (Kistler, type 9215) at the bottom plate of a CaBER device. An exchangeable geometry (e.g. diameter 6 or 8 mm) can be fixed on the force transducer. Due to oversampling of the force signal, a nominal sensitivity of 0.05 mN was reached, in combination with a time resolution of 0.2 ms, when it was connected to a charge amplifier (Kistler, type 5015). Forces can be measured over the range of $5 \times 10^{-5}$ to $2 \times 10^{2}$ N. This setup allows for simultaneously measurement of the normal force and filament diameter during extension.

A series of linear PS265 solutions with concentrations between 8 wt% and 30 wt% in DMF were prepared for the axial force measurements.
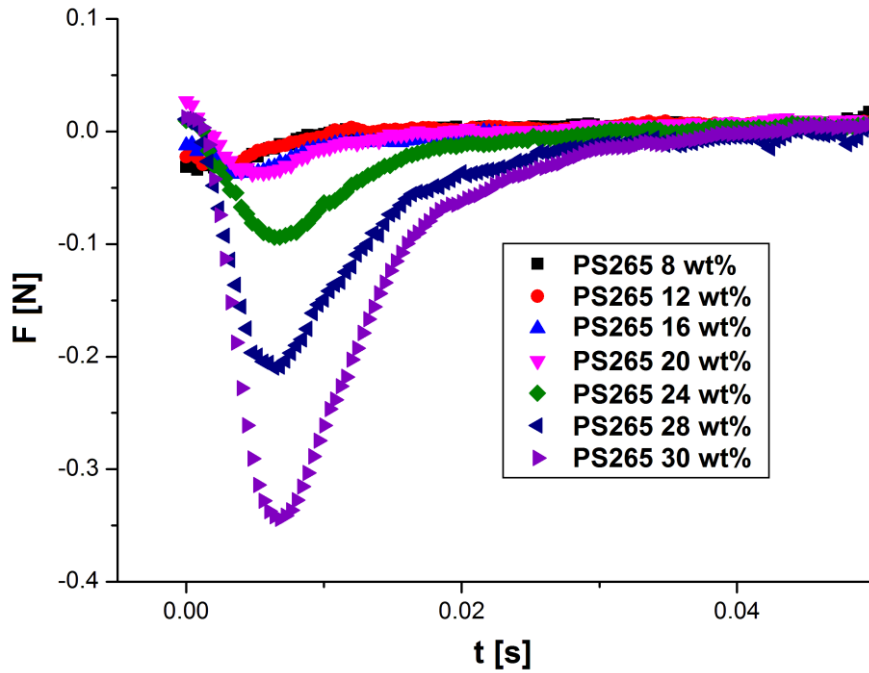
Figure 5.16: Plot of the axial force versus time for PS265 solutions in DMF and linear strike times of 50 ms at environmental temperature of T = 25 °C (see Figure 5.15).

All experiments were conducted under similar conditions, specially a constant plate diameter of 8 mm, a constant final length of $L_f$ = 12 mm, an initial gap size of 2 mm, a constant linear strike time of 50 ms and an environmental temperature of 25 °C.

An increase in concentration increases the normal force needed to break up the sample placed between two parallel plates due to entanglement of the polymer solution. With the measurement of the axial force it is possible to determine the separation energy of a polymer solution between two parallel plates. The idea behind this measurement is very close to a tack test [217-220]. In a tack experiment, an adhesive sample is brought in contact with a surface. A certain force is applied for a certain time to separate the adhesive from the surface. The quantity of tack is the work (in J) to separate surfaces per unit area (in m²) as follows:

$$W = \frac{1}{A} \int F(t) v \, dt \qquad (5.10)$$

where $A$ is the surface area (the area to be separated), $F(t)$ is the applied force during debonding of the adhesive and $v = \frac{dx}{dt}$ is the rate of separation.

A commercial device texture analyzer e.g. TA.XTplus (Stable Micro Systems, UK) exists for the tack measurements. This instrument can measure forces ranging from

± 500 N with a threshold of 1 mN. The modified CaBER with axial force geometry can measure forces between ± 200 N with a sensitivity of 0.05 mN.

For measuring the separation energy of a polymer solution on the modified CaBER, the sample was placed between two 8 mm parallel plates. The plates were separated at the velocity of $v$, which can be calculated for a linear strike from Equation 5.11:

$$v = \frac{L_f}{t_{strike}} \qquad (5.11)$$

The separation energy of a liquid is defined in a similar way as Equation 5.10, which is the integral over time of the time dependent force $F(t)$ and the separation velocity $v$ per unit area.

$$W_{sep} = \frac{1}{A} \int F(t)v dt \qquad (5.12)$$

The separation rate has a constant value for a linear strike. The constant value of the separation rate can be measured with the help of a high speed camera. A high speed FastCam–X 1024 PCI (Photron Inc., USA) camera with telecentric backlight illumination and telecentric objectives was used as shown in Figure 5.17. Analyzing the displacement of the upper geometry allows for a correct monitoring of the separation rate during a CaBER experiment.
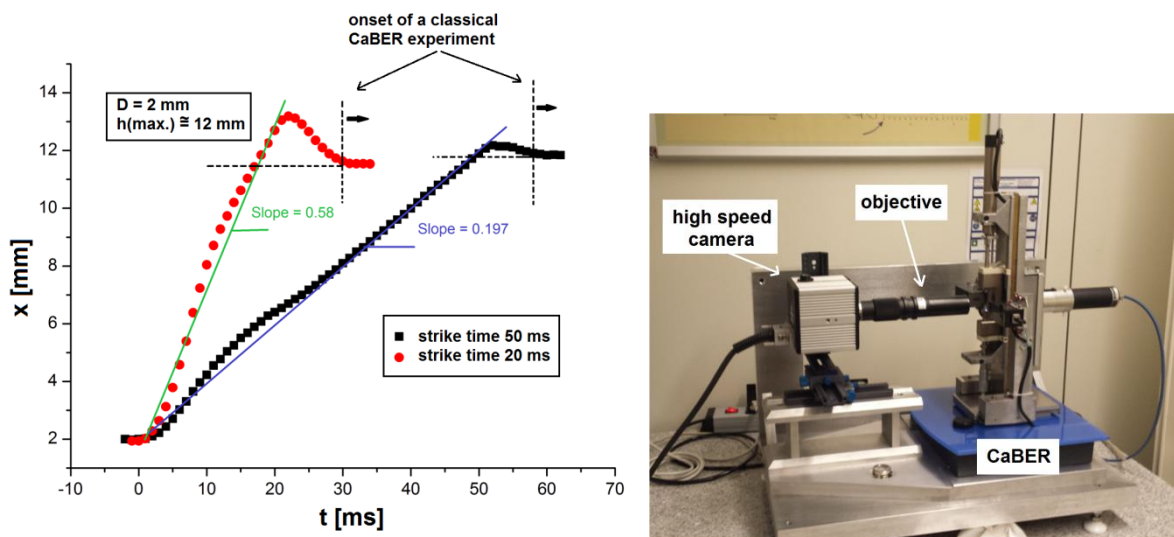


Figure 5.17: Right: setup of a high speed FastCam–X 1024 PCI (Photron Inc., USA) camera to measure the separation rate. Left: plot of distance versus time for a linear strike times of 20 and 50 ms.

The results of the experiments using high speed camera are shown in Figure 5.17. For the experiments with a linear strike and strike times lower than 50 ms, the separation rate was not linear anymore, but deviated by 16 %.

A new geometry was developed for the determination of the displacement of the upper plate as a function of time during a CaBER measurement. The geometry was a right circular cone with a half-opening angle of 9.728° as measured via a stereo microscope (Figure 5.18).
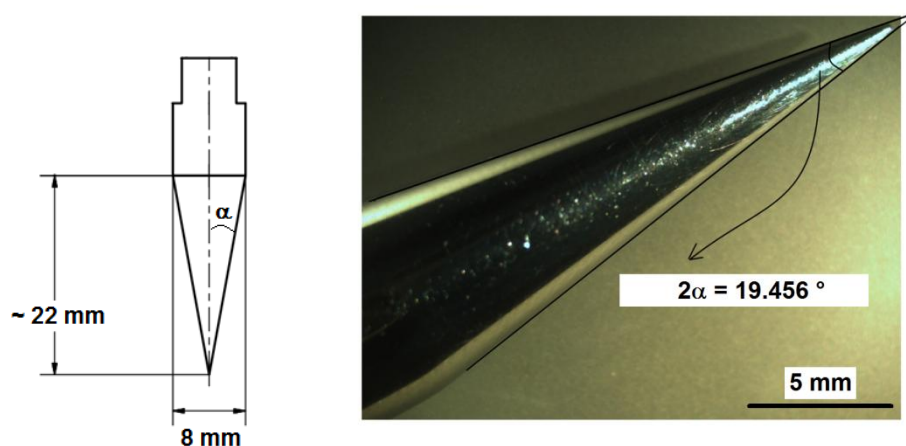


Figure 5.18: A cone geometry with a half-opening angle of 9.728° for the measurement of the displacement of the upper plate versus time for the CaBER.

The measurement started with two parallel plates. The time of strike for the elevation of the upper geometry was adjusted to 20 ms for a linear strike with a final length of 12 mm. After the Caber was run with two parallel plates, the upper geometry was replaced by the cone geometry. The lower plate was removed to avoid any collision of the cone geometry with the lower plate (Figure 5.19). The laser micrometer of CaBER was able to scan the geometry throughout the calibration experiment. Any section parallel to the base of the cone geometry is a circle whose center is on the axis of the cone. The laser micrometer can measure the diameter ($D_i$) of these circles within a time resolution of 0.4 ms.
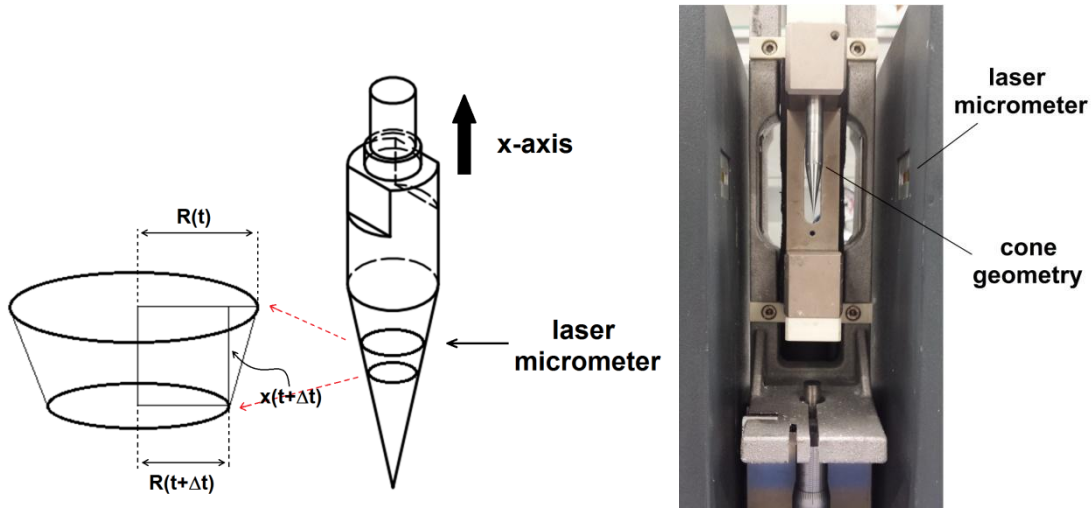
Figure 5.19: Schematic and picture of the cone geometry, which is placed in front of the laser micrometer in the CaBER. The lower plate was removed to avoid any collision of the cone geometry with the lower plate. The cone was scanned by a laser micrometer throughout the measurement.

The displacement $x_i(t + \Delta t)$ of the geometry can be calculated for every time difference of $\Delta t$ = 0.4 ms by Equation 5.13.

$$x_i(t + \Delta t) = x_{i-1}(t) + \left(\frac{D_i(t) - D_{i+1}(t + \Delta t)}{2tan(9.728°)}\right) \quad \text{for } i \in \mathbb{N} \text{ and } x_0(t) = 0 \qquad (5.13)$$

Figure 5.20 shows the plot of the displacement as a function of time as measured with the cone geometry along with the results from the high speed camera. The measurement was performed for a linear strike and a final length of 12 mm. The data from the cone geometry is similar to those from the high speed camera. The cone geometry measurements were reproducible and can be used for the calibration of any type of stretch profile (e.g. linear, exponential and cushioned strike).
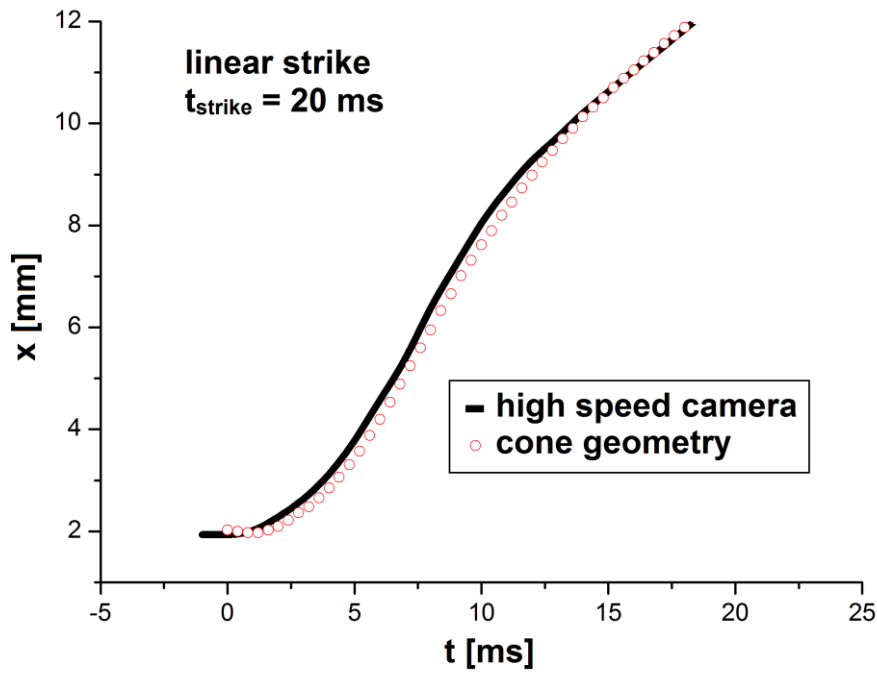
Figure 5.20: Comparison of the measurements of displacement as a function of time for a linear strike with a strike time of 20 ms from two different methods: cone geometry and high speed camera.

With the measurement of the axial force and the displacement it is now possible to determine the separation energy of electrospinning solutions as follows:

$$W_{sep} = \frac{1}{A} \int F(x)dx \qquad (5.14)$$

The goal of these experiments is the investigation of the separation energy as a function of the polymer concentration for all electrospinning solutions. The experiments were conducted at similar conditions, including using parallel plate geometries with a constant plate diameter of $D$ = 8 mm, an initial gap size of $L$ = 2 mm and a constant final length of $L_f$ = 12 mm. All experiments were conducted at an environment temperature of 25 °C. Each experiment was done at least ten times and a mean value of the calculated separation energy $W_{sep}$ is reported for all experiments. Figure 5.21 shows the plot of the axial force as a function of the geometry displacement for a 38 wt% solution of PS90 in DMF at different linear strike times.
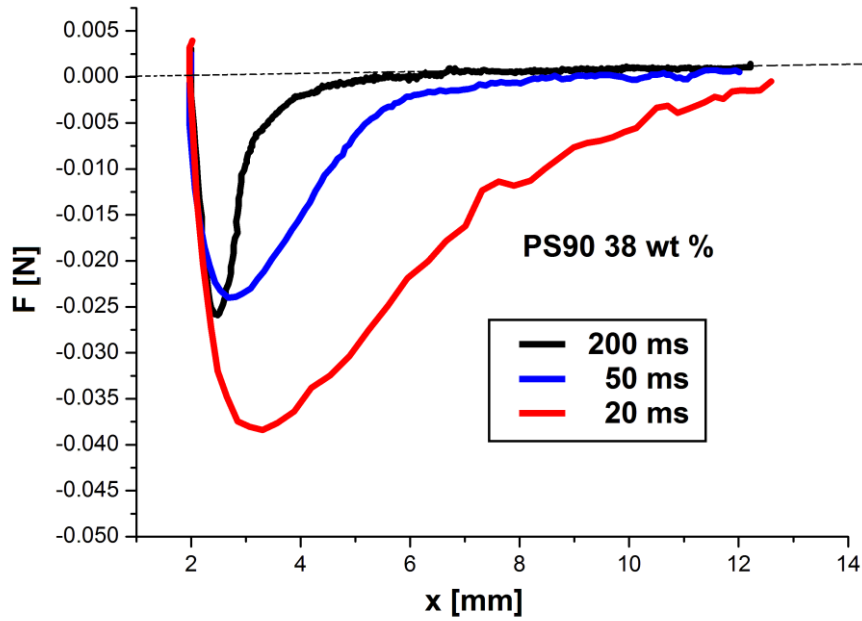
Figure 5.21: Plot of the axial force versus geometry displacement for a 38 wt% solution of PS90 in DMF at different linear strike times, $t_{strike}$ = 20, 50 and 200 ms.

The separation energy $W_{sep}$ is the area of each curve in Figure 5.21. The separation energies for a 38 wt% solution of PS90 in DMF at different strike times are given in table 5.1.

Table 5.1: Separation energies $W_{sep}$ for a 38 wt% PS90 solution in DMF at different strike times.

| Strike time [ms] | 200 | 50 | 20 |
|:---:|:---:|:---:|:---:|
| $W_{sep}$ [J/m$^2$] | $0.36 \pm 0.01$ | $1.16 \pm 0.01$ | $4.22 \pm 0.02$ |

The results in Table 5.1 show that the separation energy $W_{sep}$ is inversely proportional to the strike time for this PS90 solution. The highest values for the separation energy and the normal force were found at the fastest filament stretch ($t_{strike}$ = 20 ms). For a comparison of the separation energy for different solutions, especially solutions with lower concentrations, a fast filament stretching is recommended due to the higher sensitivity and reproducibility of the experiments. The linear stretch profile with a strike time $t_{strike}$ < 50 ms was not linear (Figure 5.17) and showed deviations from the desired stretch profile.
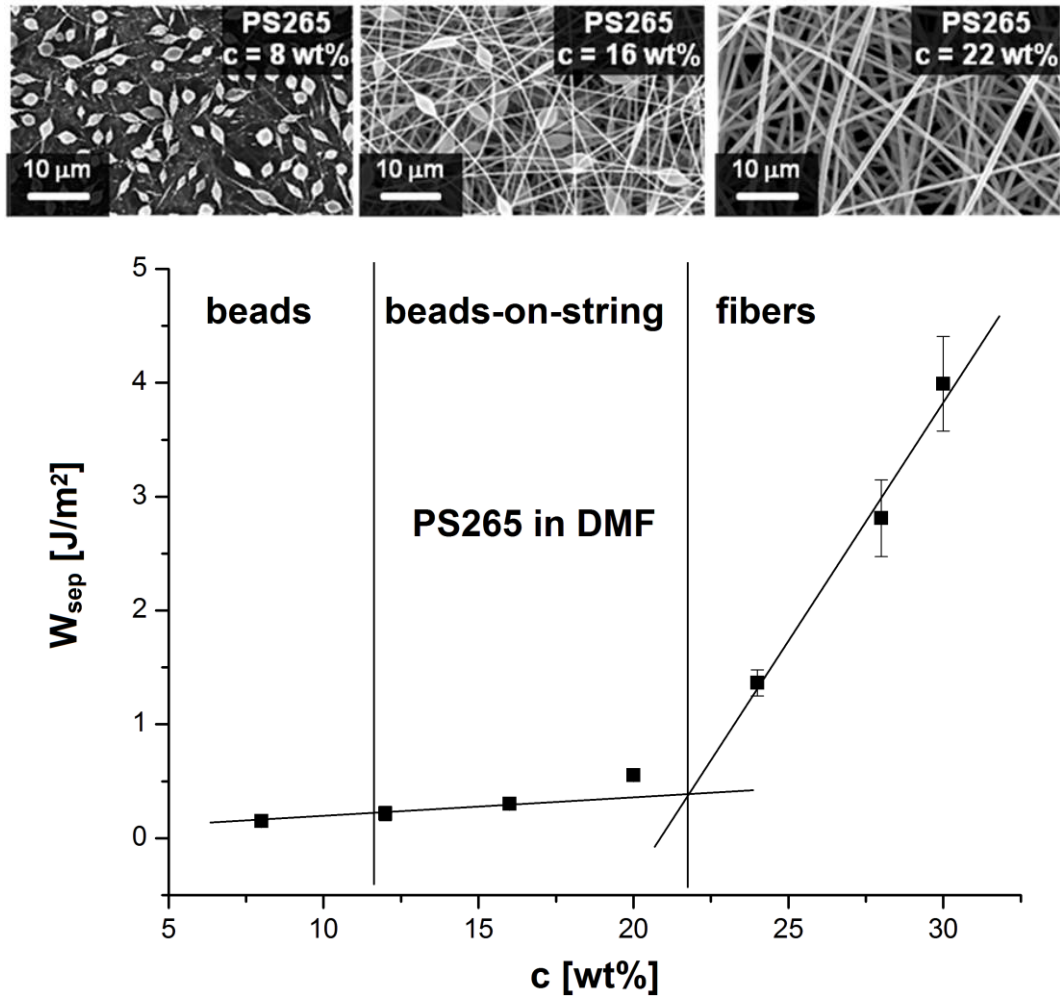
Figure 5.22: Plot of the separation energy $W_{sep}$ at a linear strike time of 50 ms, as a function of the solution concentration for linear PS ($M_n = 265$ kg/mol, $Đ = 1.1$) in DMF. The scanning electron micrographs of electrospun fibers are shown above the related morphology regions (beads, beads-on-string and uniform fibers).

Solutions of different linear and comb PS were studied in this work. All experiments were performed with the same linear stretching profile and a strike time of 50 ms. Figure 5.22 shows the separation energies $W_{sep}$ of linear PS265 solutions in DMF as a function of concentration. The concentration transitions from beads to beads-on-string and fibers were determined from the electrospinning experiments. At lower concentrations, the value of the separation energy $W_{sep}$ was low and showed no considerable changes. That means there was no significant entanglement at these concentrations. Above a critical concentration of c ~ 22 wt%, the values of the separation energy $W_{sep}$ started to show a significant change. This concentration was shown to be the minimum concentration at which continuous bead free fibers could

be electrospun. The results of the experiments with other linear PS samples are shown in Figure 5.23a and Figure 5.23b. The related concentration transition regimes are specified from the electrospinning experiments.
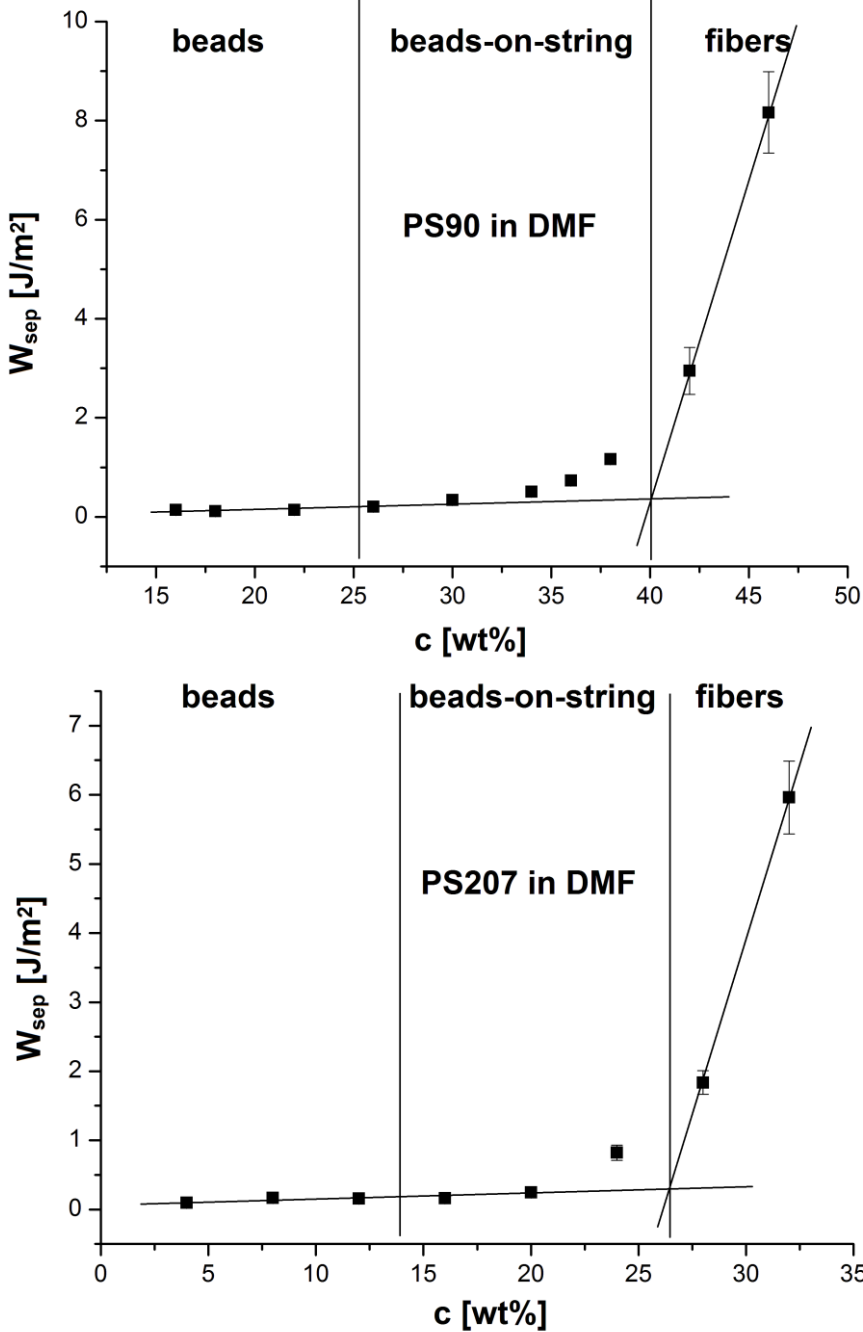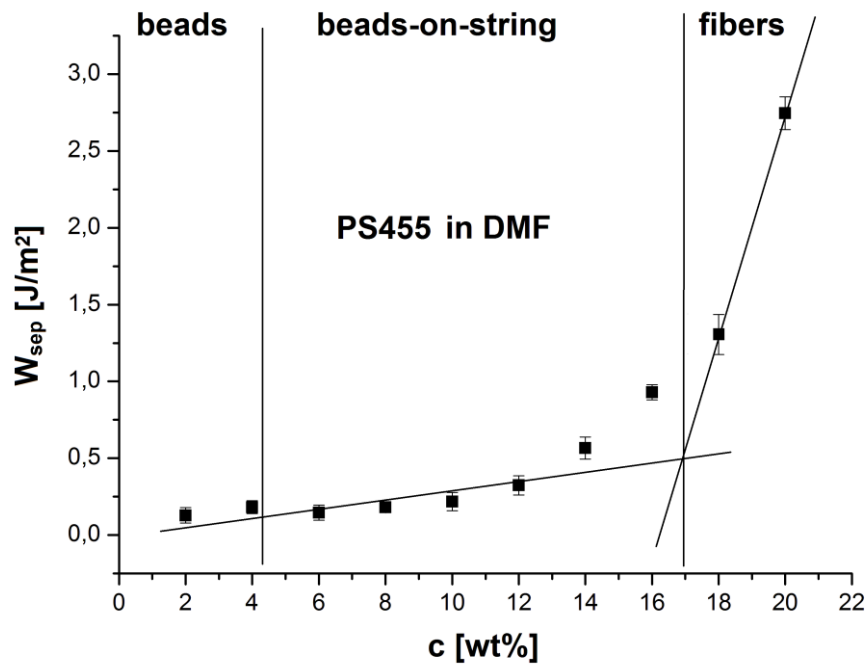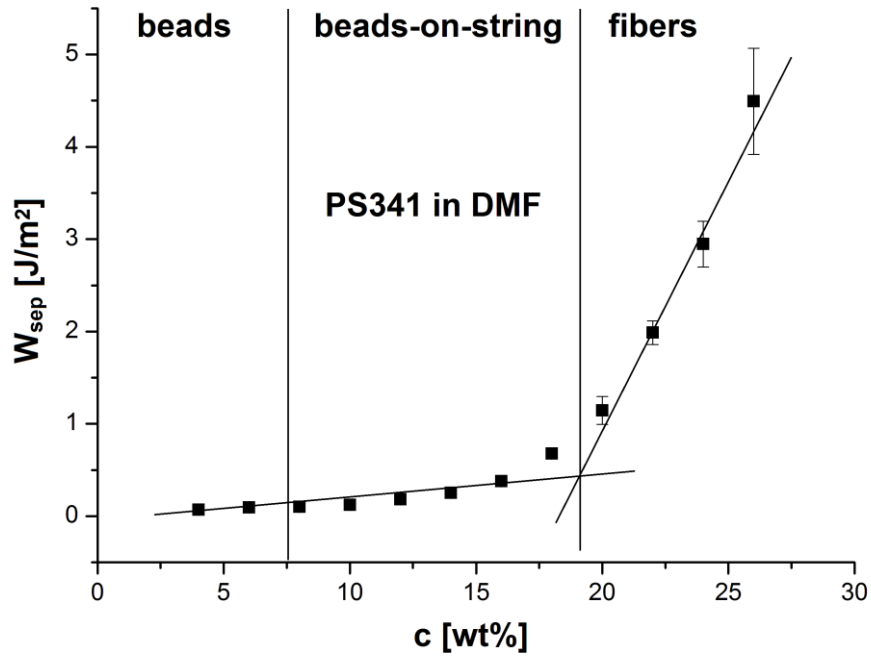


Figure 5.23a: Plots of the separation energy $W_{sep}$ at a linear strike time of 50 ms, as a function of the solution concentration for linear PS ($M_n$ = 90 kg/mol, $Đ$ = 1.05, $M_n$ = 207 kg/mol) in DMF. The related morphology regions were determined in the electrospinning process.

Figure 5.23b: Plots of the separation energy $W_{sep}$ at a linear strike time of 50 ms, as a function of the solution concentration for linear PS ($M_n = 341$ kg/mol, $Đ = 1.12$, $M_n = 455$ kg/mol, $Đ = 1.19$) in DMF. The related morphology regions were determined in the electrospinning process.

One can predict the critical concentration for fiber spinning from the plots in Figures 5.22 and 5.23. The critical concentration could be determined from the intersection of two asymptotic lines at higher and lower separation energies $W_{sep}$.

Figures 5.24 to 5.26 show the separation energies $W_{sep}$ of comb PS solutions (PS90-13-12, PS90-5-30 and PS90-4-42) in DMF as a function of the concentration. There

were no discontinuities in the plots of separation energies for the solutions of comb polymers.
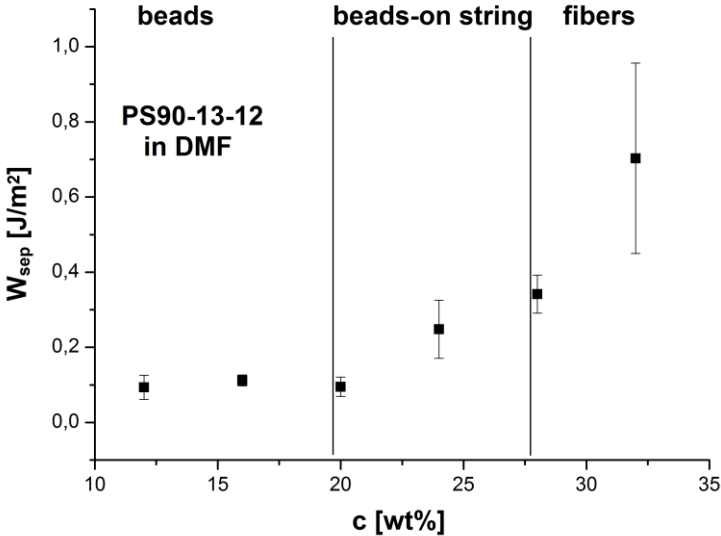


Figure 5.24: Plot of the separation energy $W_{sep}$ at a linear strike time of 50 ms, as a function of solution concentration for comb PS90-13-12 in DMF.
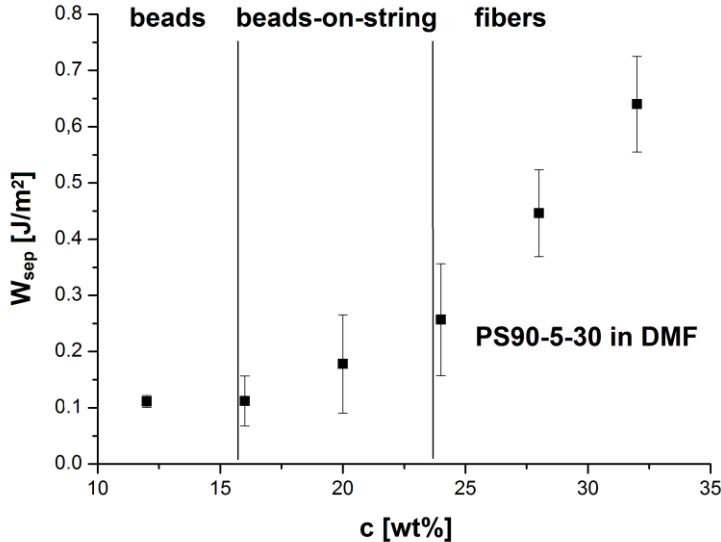


Figure 5.25: Plot of the separation energy $W_{sep}$ at a linear strike time of 50 ms, as a function of solution concentration for comb PS90-5-30 in DMF.
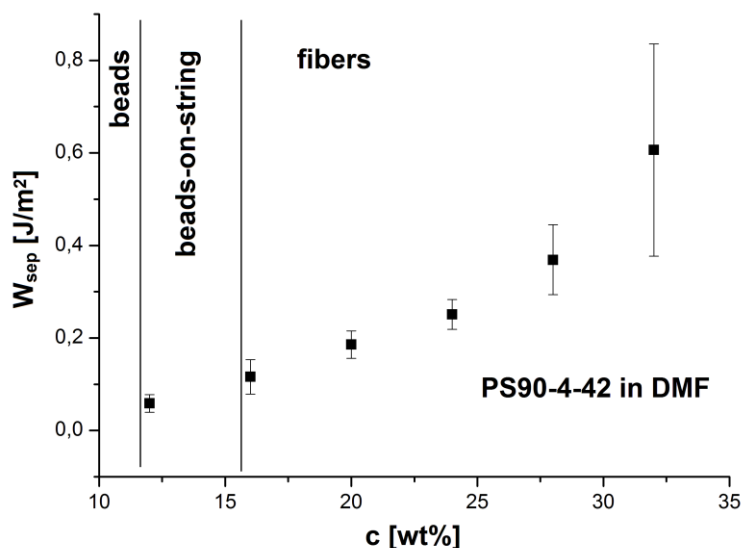
Figure 5.26: Plot of the separation energy $W_{sep}$ at a linear strike time of 50 ms, as a function of solution concentration for comb PS90-4-42 in DMF.

## 5.7 Conclusion

The effect of the molecular architecture on the morphology of electrospun micro- or nanofibers was investigated for linear and comb PS. The well-defined PS samples of Chapter 2 were electrospun and compared. Analyzing the dependence of the specific viscosity ($\eta_{sp}$) on the concentration of the polymer solutions enabled the prediction of morphological transition regimes in the electrospinning process. It was found that the onset of bead-free fiber formation from PS solutions was influenced by the topology of the comb, more specifically the number of branches and side chain length. Uniform, continuous, bead-free fibers from PS90-4-42, which had the fewest number of branches ($N_{br} = 4$) and the longest side chains ($M_n = 42$ kg/mol, ~ 2 entanglements per side chain in melt state), were successfully electrospun at a concentration that was a factor of 1.4 lower and a viscosity that was a factor of 16 lower compared to its linear counterpart with the same total molecular weight. Fibers formed from combs were more uniform and cylindrical with smoother surfaces and had a larger diameter compared with linear PS265.

The extensional properties of polymer solutions were then investigated with the improved CaBER. The improvement of the CaBER to include measurement of axial force made it possible to determine the separation energy $W_{sep}$ of a polymer solution between two parallel plates. For linear polymers, there was a critical concentration at which the separation energy changed drastically. This concentration was shown to be minimum concentration, where continuous bead free fibers could be electrospun.

For comb polymer solutions, there was no correlation between the critical concentration and the changes in the value of the separation energy.

## 6. Conclusions and outlook

Within this thesis, narrowly distributed linear and comb PS homopolymers with varying molecular weights for linear PS polymers and nearly constant molecular weights for comb PS polymers were anionically synthesized using high-vacuum and inert atmosphere techniques. All linear polymers were characterized via SEC to determine their molecular weights. For the polymer combs the length and number of branches was varied, but the total number of monomers in the side chains was kept constant. These samples were characterized with $^1$H-NMR (see Figure 2.11) and SEC-MALLS (see Table 2.1). The polymer combs have well-defined backbone ($M_{n,bb}$ ≈ 90 kg/mol) and side chain lengths with low dispersities ($Đ < 1.1$). All polymer combs were made with the same backbone, a small amount of branches (ca. 4 – 32 branches per backbone) and had a nearly constant total number of monomer segments in the side chains ($M_{n,comb}$ ≈ 250 kg/mol). These model polymers were used in the next steps for rheological and fiber spinning experiments.

The polymer combs were investigated in the linear regime using a van Gurp-Palmen plot ($\delta$ versus $|G^*|$), which shows two characteristic points for the samples with higher values of $N_{br}$, corresponding to the two minima in the plot. These minima were most prominent for PS90-13-12 and PS90-32-5. The uniaxial extensional measurements were further investigated. These measurements relate to the melt spinning of the model polymers. In the case of linear PS, an increase of the molecular weight is accompanied by low strain hardening at higher Hencky strain rates $\dot{\varepsilon}_H$. For PS combs, all samples underwent strain hardening over the range of the imposed extensional rate. At higher Hencky strain rates, an increase in the SHF can be observed with an increasing number of side arms. The polymer combs with entangled branches (PS90-5-30 and PS90-4-42) have slightly higher SHFs at lower Hencky strain rates.

The knowledge of the correlation between the molecular architecture (see Chapter 2) and the rheological properties (see Chapter 3) of the well-defined polymers is of utmost importance for the next step, the fiber spinning process.

The melt spinning setup used in this study was a capillary rheometer equipped with a Haul-off system (see Figure 4.4). The maximum of the draw-down ratio ($DDR_{max}$) was defined as a parameter to compare the spinnability of well-defined samples. These linear and comb PS sample melts were spun from a round die ($D$ = 0.5 mm) with a constant shear rate of 40 s$^{-1}$ and different take-up speeds. In general, the PS

combs showed better spinning properties in the melt state than the linear samples (see Table 4.1). The best results for the polymer combs were obtained from PS90-4-42 with a $DDR_{max}$ of 358 ± 61, which resulted in the finest filaments with a diameter of ~ 32 μm.

The fiber spinning process is limited by the onset of flow instabilities. Two sharkskin dies (a slit and a round die) were designed and constructed (see Figure 4.6, 4.7 and 4.10) to investigate the relationship between pressure fluctuations and melt flow instabilities in the die during the fiber spinning process. Each of these dies was equipped with a piezoelectric pressure transducer to detect these instabilities inside the die (see Figure 4.6 and Figure 4.10). The dies were installed on a commercial capillary rheometer (see Figure 4.6). A sample amount of ca. 100 g was needed for each experiment, which was not conceivable with well-defined anionically synthesized samples. Therefore, a series of commercial polymers were used instead in this part of the study. The melt flow instabilities were analyzed first by the Fourier transformation of the intensities for images of the extrudates and then by the Fourier transformation of the signals from the pressure transducer (see Figure 4.9 and Figure 4.11). The melt flow instabilities from both methods were clearly showed that the piezoelectric transducer picks up the melt instability. As an outlook, this work should be continued with an optimization of the synthesis route to produce larger amounts of well-defined polymers. Especially, we should consider that ca. 30 wt% of the polymer combs (up to ca. 50 wt% for samples with longer side chains e.g. PS90-4-42) was lost during the precipitation fractionation (see section 7.11) for the purification of the end product and this should be improved.

Another fiber spinning method used in this study to investigate the spinnability of well-defined polymers was electrospinning. The advantage of electrospinning is the small amount of material needed (e.g. 200 mg). Well-defined PS samples were electrospun from solutions with different concentrations. The morphological transitions from beads to bead free fibers (see Figure 5.9 and Figure 5.11), obtained fiber diameters (see Figure 5.10 and Figure 5.12) and different fiber surface morphologies (see Figure 5.14) in the electrospinning process were investigated. Here, the effect of molecular architecture on the morphology of electrospun thin fibers was investigated. The influence of the architecture of a polystyrene homopolymer (combs versus linear) was quantified. Analyzing the dependence of the specific viscosity ($\eta_{sp}$) on the concentration of the polymer solutions (see Figure 5.7), enabled

the prediction of morphological transition regimes in the electrospinning process. It was found that the onset of bead-free fiber formation from PS solutions was influenced by the topology of the polymer comb, more specifically the number of branches and side chain lengths. Uniform, continuous, bead-free fibers from PS90-4-42, which had the lowest number of branches ($N_{br}$ = 4) and the longest side chains ($M_n$ = 42 kg/mol, ~ 2 entanglements per side chain), were successfully electrospun at a concentration that was a factor of 1.4 lower and a viscosity that was a factor of 16 lower compared to its linear counterpart with the same total molecular weight (see Figure 5.13). Fibers formed from polymer combs were more uniform with smoother surfaces, had a more circular cross section and a larger diameter compared to linear PS265.

Comparison experimental findings showed better spinning properties for PS90-4-42 than other linear and comb polymer samples in both solution electrospinning and melt spinning process.

In this work electrospinning experiments with well-defined polymers were followed by investigations of the extensional properties of the electrospinning solutions with the Capillary break-up extensional rheometer (CaBER). The improvement of the CaBER to include measurement of the axial force made it possible to determine the separation energy $W_{sep}$ of a polymer solution between two parallel plates. For linear polymers at a critical concentration, there was a drastic change in the value of the separation energy (see Figure 5.22 and Figure 5.23). This concentration was shown to be the minimum concentration at which continuous bead free fibers could be electrospun. For comb polymer solutions, at a linear strike time of 50 ms, there was no correlation between the critical concentration and the changes in the value of the separation energy (see Figure 5.24, Figure 5.25 and Figure 5.26). In this study we investigated solutions of linear and comb PS samples. The PS combs with different backbone lengths and higher number of branching (3 < $N_{br}$ < 190 per backbone with $M_{n,bb}$ = 265 kg/mol, reached SHF > 200 for Hencky strains below 4 s$^{-1}$) was successfully synthesized in our research group [221]. As an outlook this work might be continued with solutions of well defined comb PS with more variations of $M_{n,bb}$, $M_{n,sc}$ and $N_{br}$. In addition, future work might include optimization of the CaBER experiment, especially for the determination of $W_{sep}$ with better control of temperature and humidity, similar to the electrospinning conditions.

## 7. Experimental methods and materials

## 7.1 High vacuum techniques for anionic polymerization

The model polymers used in this thesis were synthesized using a high vacuum line (Appendix A). The anionic polymerization is very sensitive to impurities such as water, oxygen and carbon dioxide. To remove traces of water attached to the glass surface, the glass vessels were evacuated ($p$ = ca. $10^{-3}$ mbar) and dried with a heat gun for several minutes at 600 °C, except Teflon sealings.  After cooling down the glass vessels were vented with dry argon (Argon 5.0). This procedure was repeated (three times) until all impurities were removed.

The purified solvents were condensed directly into the reactor. The solvent reservoir was heated with a water bath (e.g. toluene, T = 50 °C) and the reactor was cooled under vacuum with liquid nitrogen.
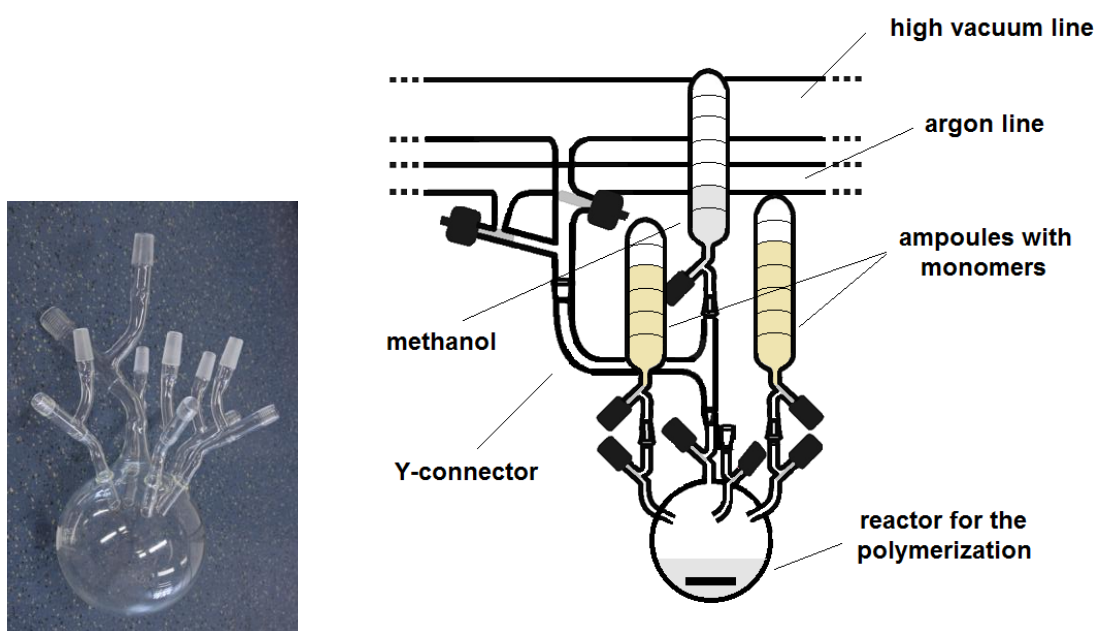


Figure 7.1: Left: Picture of an anionic polymerization reactor, which was used for the synthesis of the polymers, right: Sketch of a reactor for anionic polymerization connected to the high vacuum line.

Polymerization in a one liter reactor should be used for monomer quantities less than 50 g, and for low molecular weights (< 100 kg/mol) and nonpolar solvents, e.g. toluene. The dispersity of a synthesized polymer increases with the increasing viscosity. The reactor was connected via a Y-connector to the high vacuum line (see Figure 7.1). The ampoule with the termination solvent (e.g. methanol) can be

attached at the top of the Y-connector. The initiator can be added via a syringe under argon counterflow or via an ampoule.

## 7.2 Purification of styrene

The setup for purification of styrene is shown in Figure 7.2. To remove water from the glass surface, the distillation equipment was heated to 600 °C under vacuum for several minutes using a heat gun. After cooling down the distillation equipment was vented with argon. These steps were repeated twice to remove traces of water. The purification of styrene (Aldrich, 99 %) was carried out in two steps. First styrene was stirred over calcium hydride ($CaH_2$, Acros, 93 %) overnight. Subsequently it was distilled at reduced pressure at 85 °C into another flask containing dibutylmagnesium (Aldrich, 1 M in n-heptane). The n-heptane was removed under low pressure from the styrene prior to distillation. Finally the styrene was distilled into an ampoule at reduced pressure. For the purification steps, 1 g calcium hydride was used (flask A) and then 5 ml dibutylmagnesium solution (flask B) for 50 ml monomer. The monomer was degassed afterwards by three successive freez-evacuation-thaw cycles and then was then stored under argon at -18 °C until needed.
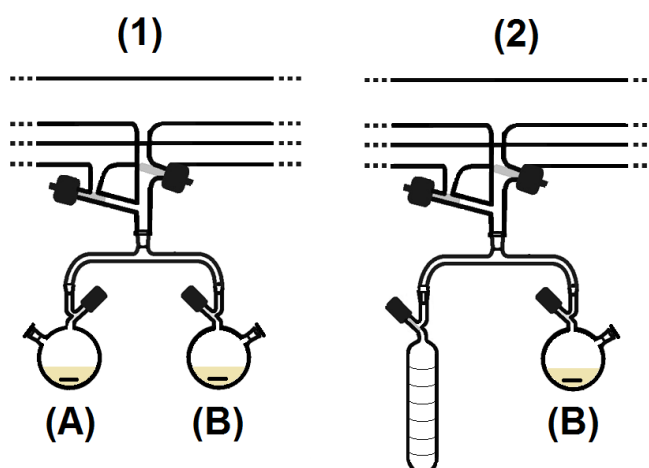


Figure 7.2: Distillation setup for purification of styrene in two steps.

## 7.3 Purification of methyl methacrylate

Methyl methacrylate (MMA) (Sigma-Aldrich, 99 %) was stirred over calcium hydride ($CaH_2$, Acros, 93 %) for two days. Subsequently it was distilled into an ampoule at reduced pressure at 65 °C. The monomer was degassed afterwards by three

successive freez-evacuation-thaw cycles and was then stored under argon at -18 °C until needed.

## 7.4 Purification of toluene

Toluene (Acros, 99.5 %) was boiled under reflux over $CaH_2$ for several days. After distillation it was stored over 1,1-diphenylhexyllithium in a solvent container, which was connected to the reactor through the vacuum line. The dark red color of 1,1-diphenylhexyllithium was used as an indicator to show the absence of protic impurities in the toluene.

## 7.5 Purification of Tetrahydrofuran

Tetrahydrofuran (THF) was dried over $CaH_2$ several days and was then additionally refluxed over sodium in the presence of benzophenone as an indicator under an argon atmosphere until a bright deep purple color was attained and was then distilled for further use.

## 7.6 Purification of 1,1- diphenylethylene

The apparatus for the purification of 1,1-diphenylethylene is shown schematically in Figure 7.3.
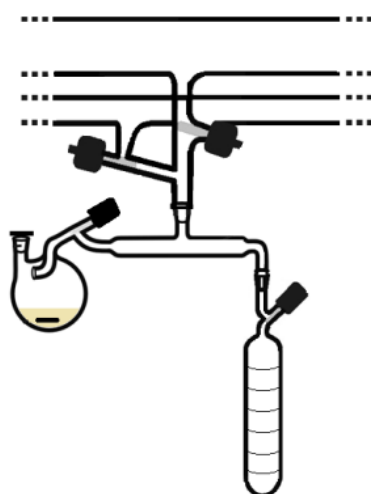


Figure 7.3: Sketch of a distillation setup for purification of styrene 1,1-diphenylethylene.

1,1-diphenylethylene (Acros, 99 %) was purified by a dropwise addition of n-butyllithium (n-BuLi) (Acros, 2.2 M in cyclohexane) until a red color was persistently formed and then distilled into ampoules (T = 85 °C) .

## 7.7 Degassing of methanol

Methanol was used for the termination of the anionic polymerization reaction. It contains dissolved oxygen, which had to be removed via degassing. The flask containing methanol was connected to the vacuum line through a stopcock. The methanol was frozen using liquid nitrogen and then a vacuum was applied to the frozen bulk (figure 7.4). The stopcock was then closed and the liquid was thawed until bubbles appeared. The liquid was then frozen again and exposed to vacuum. The freeze and thaw cycle was repeated until no bubbles arose in the liquid during the thaw step.
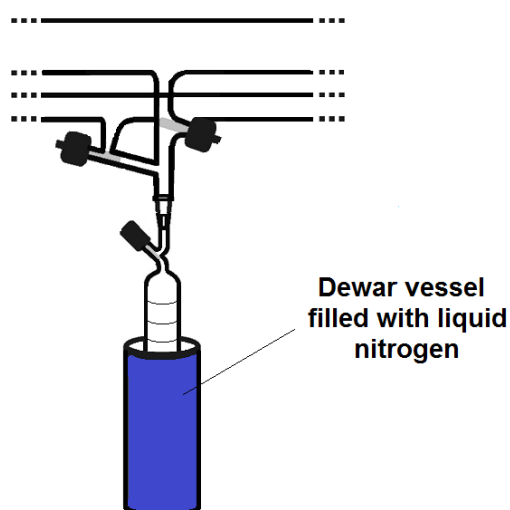
Dewar vessel
filled with liquid
nitrogen

Figure 7.4: Schematic sketch of the apparatus used for the degassing of methanol. The Dewar is filled with liquid nitrogen.

## 7.8 Synthesis of linear polystyrene as the backbone and side chain

Anionic polymerization of styrene was performed using high vacuum techniques as described in Figure 7.1. The ampoules and the polymerization reactor were equipped with high-vacuum PTFE stopcocks and ground glass joints. Dry toluene was introduced from the solvent reservoir through the vacuum line into the reactor. The polymerizations of styrene for the polymer backbone and side chains were performed

at room temperature with sec-Butyllithium (sec-BuLi) (Sigma-Aldrich, 1.4 M in cyclohexane) as the initiator and toluene as the solvent. The living polymer that later became the backbone was terminated by adding a small amount of degassed MeOH after complete conversion of the monomer (14 h). The polymer was precipitated in MeOH and dried at 70 °C under vacuum. The side branches were synthesized using a similar approach, but were not terminated except for a sample of the living PS that was collected for molecular characterization.

## 7.9 Synthesis of linear poly (methyl metacrylate)

The setup for the preparation of the initiator for the anionic polymerization of MMA is shown in Figure 7.5. The initiator for the polymerization of MMA was prepared in dry toluene. The toluene (~20 ml) was introduced into an ampoule, which was connected to the vacuum line and equipped with PTFE stopcocks. The desired amount of the initiator (sec-BuLi) was added with a syringe into the toluene under argon counter flow. Then an excess of 1,1-diphenylethylene (10% excess) was added to the toluene/sec-BuLi solution and the mixture was stirred for 30 min at room temperature.
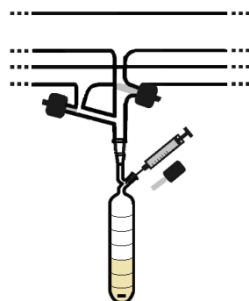


Figure 7.5: Schematic sketch of the setup used for the preparation of an initiator solution for the anionic polymerization of MMA.

The polymerization of MMA was carried out in THF (Vol. (THF)/Vol. (MMA) = 15/1), which was cooled to -78 °C using an acetone/liquid nitrogen cooling bath. The initiator was added fast to the THF/MMA solution and stirred for 1 h. The living polymer was terminated by adding a small amount of degassed MeOH, then precipitated in MeOH and dried at 70 °C under vacuum.

## 7.10   Acetylation of linear polystyrene

The partially acetylated PS backbone (< 2 mol %) was prepared by Friedel-Crafts acetylation of PS using acetyl chloride and anhydrous aluminum chloride as the acetylation agent and catalyst, respectively [88]. Chloroform ($CHCl_3$, Sigma-Aldrich, 99.9 %) was distilled from $CaH_2$ under argon before use. As an example of a model comb synthesis, the preparation of a comb polymer with an average of 16 acetylated groups per backbone is presented. A solution of 20 g PS ($M_n$ = 90 kg/mol, $Đ$ = 1.05) in chloroform (100 ml) was added to a stirred solution of acetyl chloride (Fluka, 99 %, 0.32 ml, 4.5 mmol), aluminum chloride (Sigma-Aldrich, 1 M in nitrobenzene, 4.5 ml, 4.5 mmol) and 20 ml chloroform under argon atmosphere. The mixture was stirred for 5 h at room temperature and then precipitated into acidified methanol (1000 ml, 15 ml HCl; 6 M). The polymer was precipitated again in MeOH and dried at 70 °C under vacuum.

## 7.11   Synthesis of polystyrene combs

A two liter round flask was used as the reactor for the synthesis of the PS combs (see Figure 7.6). A total of 20 g partially acetylated PS backbone was dissolved in 700 ml THF (Acros, 99.5 %) in a two liter round flask. The THF was dried as described in section 7.5. The solution of PS in THF was cooled to approximately - 80 °C with an acetone/liquid nitrogen cooling bath. The living PS side chains (50% excess) were added dropwise into the PS backbone solution. The reaction was allowed to continue for 1 h and then the residual living side chains were terminated with degassed methanol. Unreacted side chains were successfully separated from PS combs by repetition of precipitation/fractionation in a THF/methanol mixture. The polymer was filtered and dried at 70 °C under vacuum.
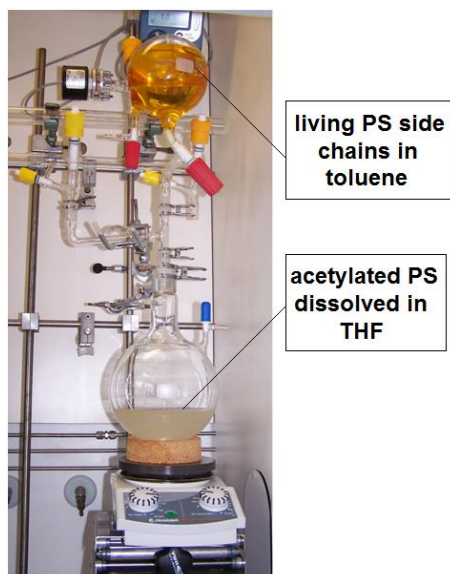
Figure 7.6: Picture of the two liter reactor, which is used for the synthesis of comb polymers. The reactor was connected via a Y-connector to the high vacuum line. The reactor was cooled down to approximately -80 °C and the living PS side chains were added dropwise to the solution containing the backbone.

## 7.12 Size exclusion chromatography (SEC)

The molecular weights of the linear backbone, side chains and fractionated combs were determined using size exclusion chromatography (SEC), which was operated with THF as the solvent and calibrated with linear PS standards. The concentrations of the polymer chains in the continuous eluent flow were analyzed by a differential refractive index (DRI) detector. The SEC system was calibrated using linear PS standards ranging from 476 to 2.5 x $10^6$ g/mol. The molecular weights of the linear PS obtained from SEC agreed with those calculated based on the monomer to initiator ratio within measurement uncertainties.

The absolute weight-averaged molecular weight ($M_w$) and the dispersity ($Đ$) of the combs were determined by SEC-MALLS (multi angle laser light scattering). A triple-detection SEC chromatographic setup was used for the determination of the Mark-Houwink-Kuhn-Sakurada (MHKS) parameters via a modular system (Polymer Standard Service, PSS Mainz/Agilent 1200 series) incorporating an ETA2010 viscosity detector (WGE Dr Bures) combined with a MALLS unit (PSS SLD7000/BI-MwA, Brookhaven Instruments). Sample separation was achieved via two linear columns provided by PSS (SDV-Lux-1000 Å and $10^5$ Å, 5 $\mu$m) with THF as the eluent

at 25 °C and a flow rate of 1 ml/min. The sample concentration was close to 3 mg/ml prior to injection. The injection volume was 100 μl.

## 7.13  NMR- Spectroscopy

The ^{1}H-NMR spectra of the partially acetylated PS backbone were measured in CDCl$_3$ with a Bruker Avance III Microbay 400 MHz spectrometer (typically 1024 scans). ^{1}H-NMR (400 MHz, CDCl$_3$): δ = 2.45 ppm (s, 3H, CO-C<u>H$_3$</u>), 7.5 - 7.7 ppm (m, 2H, benzyl protons ortho to acetyl group). The average number of acetyl groups per backbone was calculated from the ratio of the peak integrals of the CH$_3$ protons at 2.45 ppm and the five aromatic protons located between 6 and 7.5 ppm.

## 7.14  Rheological characterization

The rheological characterization of the polymer solutions was performed using a strain-controlled ARES G2 Rheometer (TA Instrument) equipped with a concentric cylinder measuring system consisting of a 18.6 mm diameter bob and 20 mm diameter cup. The viscosities of the solutions were measured using a steady shear rate sweep between 1 and 2000 s$^{-1}$. The sample temperature was maintained at 25 °C with a Peltier temperature controller during all experiments. The rheological measurements on the polymer melts were performed on the same rheometer using a 13 mm diameter parallel plate geometry and a gap of 1 mm. Oscillatory shear measurements were carried out at temperatures between 130 and 200 °C using a frequency range from 10$^{-2}$ to 100 rad/s at each temperature. Rheological master curves were referenced to 150 °C (T$_g$ + 50 °C) using Williams-Landel-Ferry (WLF) shift factors [104, 105]. The uniaxial extensional experiments were carried out using an extensional viscosity fixture (EVF) at extensional rates between 0.01 and 3 s$^{-1}$ with a maximum Hencky strain rate of $\varepsilon_H = 4$.

## 7.15  Electrospinning

Various solutions of linear and branched PS (samples described in Table 1) and two samples of linear PMMA were prepared by dissolving the desired amounts of the polymer samples in DMF. The polymers in DMF were stirred for 24 h to obtain a

homogeneous solution. The solutions were prepared with concentrations ranging from 4-46 wt % (PS90), 4-32 wt% (PS207), 4-28 wt % (PS265), 4-26 wt % (PS344), 2-22 wt % (PS475), 12-32 wt % (PS90-13-12, PS90-5-30 and PS90-4-42), 2-28 wt % (PMMA80) and 4-24 wt % (PMMA200). The solution was loaded into a 1 ml syringe. The syringe was placed in a syringe pump (NE-1000) connected to the electrospinning device (EC-CLI, IME Technologies, Netherlands). A 21 gauge needle (inner diameter ~ 0.6 mm), an electrical potential of 12 kV, a tip-to-collector distance of 17 cm and a pumping rate of 1.1 ml/h were used in all experiments. Electrospinning was conducted at room temperature (25 °C) and a relative humidity of 25%.
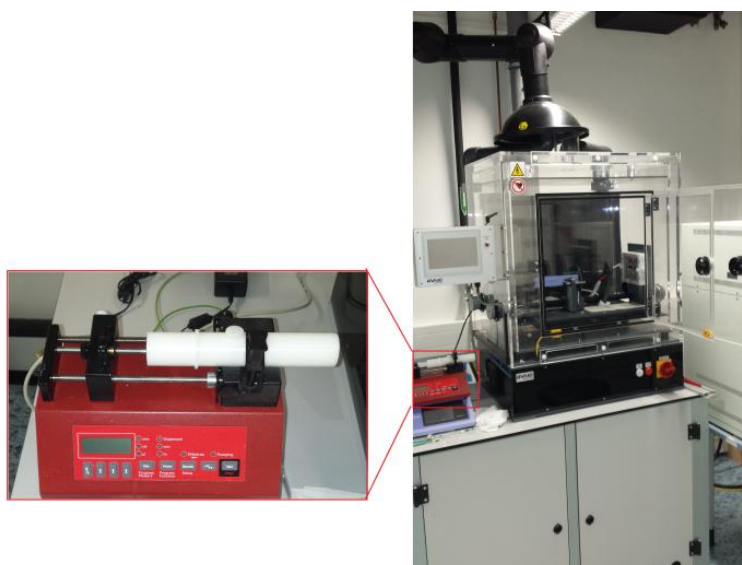


Figure 7.7: Picture of the electrospinning device (EC-CLI, IME Technologies, Netherlands), which was used for solution electrospinning in this project. The device is equipped with a programmable single syringe pump (NE-1000).

## 7.16   Scanning electron microscopy (SEM)

The morphology of the electrospun fibers was analyzed using a field emission scanning electron microscope (FESEM, Zeiss-AURIGA 60) with an accelerating voltage of 10 kV. Each sample was coated with gold using a Balzers SCD 040 sputter coater for 10 s prior to observation. Image processing software (ImageJ 1.48v) was used to measure the average diameter of the as-spun fibers, which was taken to be the mean value of 40 separate measurements.

Electron microscopes expand the range of light microscopes, which are limited due to the wavelength range of visible light, to smaller structures and smaller wavelengths respectively [222, 223]. The SEM is the most widely used of the electron beam instruments. In SEM the specimen is covered with a thin metal layer, usually gold, and the focused electron beam scans line by line over the surface of the specimen in the evacuated microscope column. The SEM consists of an electron source; accumulations of lenses (electromagnetic coils), detectors, and a vacuum system (chamber and pump system). The image is displayed on a computer system and/or a screen. The beam electrons are emitted from the cathode. The electrons are accelerated by a voltage of typically 0.5-30 kV. This forms a small beam near the anode with a diameter of about 10–50 μm. The spot size is too large to produce a sharp image. Therefore, it is demagnified by the lens system consisting of one or two condenser lenses and one objective lens and focused on the specimen surface. While the electron beam scans the surface line by line, the detectors collect and count the secondary and backscattered electrons [224]. The resulting signals for each point are converted to grey values. As a result a grey value image of the topography is obtained. The more electrons are detected, the brighter the image point will be. The magnification of SEM is in the range of 100-1,000,000 [225].

## 8. References

1. T. Hongu, G.O. Phillips, New fibers, Elsevier, 1997.
2. K. Chawla, Fibrous materials, Cambridge University Press, 2016.
3. R.R. Mather, R.H. Wardman, The chemistry of textile fibres, Royal Society of Chemistry, 2015.
4. J. Harington, F. Roe, Annals of the New York Academy of Sciences 132 (1965) 439-450.
5. S.S. Muthu, Textiles and Clothing Sustainability, Springer, 2016.
6. E. Aizenshtein, Fibre Chemistry 48 (2017), 447-455.
7. S. Eichhorn, J. Hearle, M. Jaffe, T. Kikutani, Handbook of textile fibre structure: Natural, regenerated, inorganic and specialist fibres, Elsevier, 2009.
8. J.W. Hearle, W.E. Morton, Physical properties of textile fibres, Elsevier, 2008.
9. R. Beyreuther, H. Brünig, Dynamics of fibre formation and processing: modelling and application in fibre and textile industry, Springer, 2006.
10. D.C. Huang, J.L. White, Polymer Engineering & Science 19 (1979) 609-616.
11. J. Zimmerman, M.I. Kohan, Journal of Polymer Science Part A: Polymer Chemistry 39 (2001) 2565-2570.
12. G. Odian, Principles of polymerization, John Wiley & Sons, 2004.
13. C. Andreoli, F. Freti, Man Made Fibers, ACIMIT Fondazione, 2004.
14. T. Kikutani, Progress in Fiber Spinning Technology. High-Performance and Specialty Fibers, Springer, 2016.
15. J.E. Mark, Physical properties of polymers handbook, Springer, 2007.
16. F. Moncrieff, Man-made fibres, John Wiley & Sons, 1963.
17. M. A. A. AlMa'adeed, I. Krupa. Polyolefin Compounds and Materials. Springer International Publishing, 2016.
18. J.M. Kelly, Journal of Macromolecular Science, Part C: Polymer Reviews 42 (2002) 355-371.
19. S.M. Kurtz, L. Pruitt, C.W. Jewett, R.P. Crawford, D.J. Crane, A.A. Edidin, Biomaterials 19 (1998) 1989-2003.
20. P. Smith, P.J. Lemstra, Journal of Materials Science 15 (1980) 505-514.
21. A. Pennings, R. Van Der Hooft, A. Postema, W. Hoogsteen, G.T. Brinke, Polymer Bulletin 16 (1986) 167-174.
22. A. Greiner, J.H. Wendorff, Electrospinning: A Fascinating Method for the Preparation of Ultrathin Fibers, Wiley-VCH, 2007.
23. A.L. Andrady, Science and technology of polymer nanofibers, John Wiley & Sons, 2008.
24. B. Ding, J. Yu, Electrospun nanofibers for energy and environmental applications, Springer, 2014.
25. N. Hadjichristidis, A. Hirao, Anionic Polymerization, Springer, 2015.
26. N. Hadjichristidis, S. Pispas, G. Floudas, Block Copolymers Synthetic Strategies, Physical Properties, and Applications, John Wiley & Sons, 2003.
27. T. Yamamoto, Y. Tezuka, Cyclic and Multicyclic Topological Polymers. Complex Macromolecular Architectures, John Wiley & Sons, 2011..
28. N. Hadjichristidis, H. Iatrou, S. Pispas, M. Pitsikalis, Journal of Polymer Science Part A, Polymer Chemistry 38 (2000) 3211-3234.
29. T. Higashimura, S. Aoshima, M. Sawamoto. New initiators for living cationic polymerization of vinyl compounds. Macromolecular Symposia, vol. 13, Wiley Online Library, 1988.
30. A. Gandini, Recent Advances In Cationic Polymerization. Integration of Fundamental Polymer Science and Technology, Springer, 1988.

31. G. Black, D. Maher, W. Risse, Handbook of Metathesis, Wiley-VCH, 2003.
32. H. Mark, Encyclopedia of Polymer Science and Technology, vol.12, John Wiley & Sons, Inc, 2005.
33. A.H.E. Müller, K. Matyjaszewski, Controlled and Living Polymerizations, Wiley-VCH, 2009.
34. D.J. Worsfold, S. Bywater, Canadian Journal of Chemistry 38 (1960) 1891-1900.
35. M. Morton, L.J. Fetters, Rubber Chemistry and Technology 48 (1975) 359-409.
36. L.J. Fetters, Journal of Research of the National Bureau of Standards, Section A: Physics and Chemistry 70A (1966) 421-433.
37. M. Szwarc, Nature 178 (1956) 1168-1169.
38. M. Szwarc, M. Levy, R. Milkovich, Journal of the American Chemical Society 78 (1956) 2656-2657.
39. M. Morton, F.R. Ells, Journal of Polymer Science 61 (1962) 25-29.
40. M. Morton, L.J. Fetters, Journal of Polymer Science: Macromolecular Reviews 2 (1967) 71-113.
41. C. Geacintov, J. Smid, M. Szwarc, Journal of the American Chemical Society 84 (1962) 2508-2514.
42. H.-G. Elias, Macromolecules, Wiley-VCH, 2005.
43. P.J. Flory, Journal of the American Chemical Society 62 (1940) 1561-1565.
44. R.F.T. Stepto, Pure and Applied Chemistry, 81 (2009) 351-353.
45. R.P. Quirk, Applications of Anionic Polymerization Research, American Chemical Society, 1998.
46. J. Clayden, N. Greeves, S. Warren, P. Wothers, Organic Chemistry, Oxford University Press, 2001.
47. F. Carey, Organic Chemistry 4th ed., McGraw-Hill, 2000.
48. D.E. Bergbreiter, J.R. Blanton, R. Chandran, M.D. Hein, K.J. Huang, D.R. Treadwell, S.A. Walker, Journal of Polymer Science Part A: Polymer Chemistry 27 (1989) 4205-4226.
49. M. Aldissi, F. Schué, H. Liebich, K. Geckeler, Polymer 26 (1985) 1096-1098.
50. G.K. Rickle, Journal of Macromolecular Science: Part A - Chemistry 23 (1986) 1287-1297.
51. A. Zilkha, B.-A. Feit, M. Frankel, Journal of Polymer Science 49 (1961) 231-240.
52. M. Horiba, N. Yamashita,T. Maeshima, Journal of Macromolecular Science: Part A - Chemistry 23 (1986) 1117-1123.
53. A.R. Lyons, E. Catterall, European Polymer Journal 7 (1971) 839-848.
54. H. Yuki, Y. Okamoto, Y. Kuwae, K. Hatada, Journal of Polymer Science, Polymer Chemistry 7 (1969) 1933-1946.
55. J.W. Mays, N. Hadjichristidis, Polymer Bulletin 22 (1989) 471-474.
56. J.C. Chen, L.J. Fetters, Polymer Engineering & Science 27 (1987) 1300-1309.
57. K. Se, M. Kijima, T. Fujimoto, Polymer journal 20 (1988) 791-799.
58. E. Ogawa, N. Yamaguchi, M. Shima, Polymer journal 18 (1986) 903-910.
59. I. Königsberg, J. Jagur-Grodzinski, Journal of Polymer Science Part A: Polymer Chemistry 21 (1983) 2649-2663.
60. H. McCormick, Journal of Polymer Science Part A: Polymer Chemistry 25 (1957) 488-490.
61. D. Ades, M. Fontanille, J. Leonard, M. Thomas, European Polymer Journal 19 (1983) 305-311.

62. P. Chaumont, G. Beinert, J. Herz, P. Rempp, Macromolecular Chemistry and Physics 180 (1979) 2061-2071.
63. P. Chaumont, G. Beinert, J. Herz, European Polymer Journal 18 (1982) 875-879.
64. I. Krasnoselskaya, B. Erussalimsky, Acta Polymerica 37 (1986) 72-75.
65. M. Möller, R.W. Lenz, Macromolecular Chemistry and Physics 190 (1989) 1153-1168.
66. C.C. Meverden, T.E. Hogen-Esch, Journal of Polymer Science Part A: Polymer Chemistry 23 (1985) 159-168.
67. A. Natalello, J. Morsbach, A. Friedel, A. Alkan, C. Tonhauser, A.H.E. Müller, H. Frey, Organic Process Research & Development 18 (2014) 1408-1412.
68. X. Chen, I.S. Ke, M. Li, J. Wu, M.A. Rickard, Journal of Raman Spectroscopy 48 (2017) 1002-1006.
69. H. Yuki, K. Hatada, Advances in Polymer Science, 31 (1979) 1-45.
70. R. Fayt, R. Forte, C. Jacobs, R. Jérôme, T. Ouhadi, P. Teyssie, S.K. Varshney, Macromolecules 20 (1987) 1442-1444.
71. S.K. Varshney, C. Jacobs, J.P. Hautekeer, P. Bayard, R. Jerome, R. Fayt, P. Teyssie, Macromolecules 24 (1991) 4997-5000.
72. D.L. Glusker, I. Lysloff, E. Stiles, Journal of Polymer Science Part A: Polymer Chemistry 49 (1961) 315-334.
73. K.F. Elgert, W. Ritter, Macromolecular Chemistry and Physics 177 (1976) 2021-2030.
74. D. Richards, Chemical Society Reviews 6 (1977) 235-260.
75. D.J. Worsfold, S. Bywater, Canadian Journal of Chemistry 42 (1964) 2884-2892.
76. H. Hsieh, R.P. Quirk, Anionic polymerization: principles and practical applications, CRC Press, 1996.
77. F.A. Carey, R.J. Sundberg, Organometallic Compounds of Group I and II Metals. Advanced Organic Chemistry, Part B: Reactions and Synthesis, Springer, 1990.
78. C. Elschenbroich, Organometallchemie, Wiesbaden Vieweg Teubner, 2008.
79. K. Matyjaszewski, M. Möller, Polymer science : a comprehensive reference, Elsevier, 2012.
80. K. Hong, D. Uhrig, J.W. Mays, Current Opinion in Solid State and Materials Science 4 (1999) 531-538.
81. N. Hadjichristidis, M. Pitsikalis, S. Pispas, H. Iatrou, Chemical reviews 101 (2001) 3747-3792.
82. H.-Q. Xie, D. Xie, Progress in polymer science 24 (1999) 275-313.
83. N. Hadjichristidis, H. Iatrou, M. Pitsikalis, J. Mays, Progress in Polymer Science 31 (2006) 1068-1132.
84. R.K. Iha, K.L. Wooley, A.M. Nystrom, D.J. Burke, M.J. Kade, C.J. Hawker, Chemical reviews 109 (2009) 5620-5686.
85. A. Vazaios, N. Hadjichristidis, Journal of Polymer Science Part A: Polymer Chemistry 43 (2005) 1038-1048.
86. D. Pantazis, I. Chalari, N. Hadjichristidis, Macromolecules 36 (2003) 3783-3785.
87. J. Yuan, A.H.E. Müller, K. Matyjaszewski, S.S. Sheiko, Polymer Science: A Comprehensive Reference, Elsevier, 2012.
88. M. Kempf, D. Ahirwal, M. Cziep, M. Wilhelm, Macromolecules 46 (2013) 4978-4994.
89. J. Li, M. Gauthier, Macromolecules 34 (2001) 8918-8924.

90. M. Janata, B. Masař, L. Toman, P. Vlček, P. Polická, J. Brus, P. Holler, Reactive and Functional Polymers 50 (2002) 67-75.
91. P.Y. Bruice, Essential organic chemistry, Pearson Education, 2006.
92. F.Z. Dorwald, A Guide to Successful Systhesis Design, Wiley-VCH, 2005.
93. K. Riazi, J. Kübel, M. Abbasi, K. Bachtin, S. Indris, H. Ehrenberg, R. Kádár, M. Wilhelm, Polymer 104 (2016) 240-250.
94. M.H. Wagner, J. Hepperle, H. Münstedt, Journal of Rheology 48 (2004) 489-503.
95. B.H. Zimm, R.W. Kilb, Journal of Polymer Science Part A: Polymer Chemistry 37 (1959) 19-42.
96. W.H. Stockmayer, M. Fixman, Annals of the New York Academy of Sciences 57 (1953) 334-352.
97. B.H. Zimm, W.H. Stockmayer, The Journal of Chemical Physics 17 (1949) 1301-1314.
98. H.L. Wagner, Journal of Physical and Chemical Reference Data 14 (1985) 1101-1106.
99. M.J.R. Cantow, Polymer Fractionation, Academic Press, 1967.
100. M.L. Huggins, Journal of Polymer Science Part A: Polymer Chemistry 16 (1955) 209-219.
101. M.L. Huggins, Journal of the American Chemical Society 86 (1964) 3535-3540.
102. P.J. Flory, The Journal of chemical physics 10 (1942) 51-61.
103. F. Francuskiewicz, Precipitation Fractionation. Polymer Fractionation, Springer, 1994.
104. J.M. Dealy, J. Wang, Melt rheology and its applications in the plastics industry, 2nd ed., Springer, 2013.
105. J.M. Dealy, R.G. Larson, Structure and Rheology of Molten Polymers: From Structure to Flow Behavior and Back Again, Carl Hanser, 2006.
106. F.A. Morrison, Understanding rheology, Topics in Chemical Engineering, Oxford University Press, 2001.
107. G. Schramm, A practical approach to rheology and rheometry, Haake Karlsruhe, 1994.
108. T.G. Mezger, The rheology handbook: for users of rotational and oscillatory rheometers, Vincentz Network, 2006.
109. F. Irgens, Rheology and non-Newtonian fluids, Springer, 2014.
110. A.A. Collyer, D.W. Clegg, Rheological Measurement, Springer, 1998.
111. M.L. Williams, R.F. Landel, J.D. Ferry, Journal of the American Chemical Society 77 (1955) 3701-3707.
112. M. Doi, S.F. Edwards, The theory of polymer dynamics, Oxford University Press, 1988.
113. W.W. Graessley, The entanglement concept in polymer rheology, Springer, 1974.
114. S. Wu, Journal of Polymer Science Part B: Polymer Physics 25 (1987) 557-566.
115. J.D. Ferry, Viscoelastic properties of polymers, John Wiley & Sons, 1980.
116. P.-G. de Gennes, The journal of chemical physics 55 (1971) 572-579.
117. H.A. Barnes, A handbook of elementary rheology, University of Wales, 2000.
118. L.J. Fetters, D.J. Lohse, R.H. Colby, Physical Properties of Polymers Handbook, Springer, 2007.
119. D.R. Daniels, T.C.B. McLeish, B.J. Crosby, R.N. Young, C.M. Fernyhough, Macromolecules 34 (2001) 7025-7033.

120. J. Hepperle, H. Münstedt, P. Haug, C. Eisenbach, Rheologica Acta 45 (2005) 151-163.
121. H. Münstedt, F.R. Schwarzl, Deformation and Flow of Polymeric Materials, Springer, 2014.
122. S. Trinkle, C. Friedrich, Rheologica Acta 40 (2001) 322-328.
123. S. Trinkle, P. Walter, C. Friedrich, Rheologica Acta 41 (2002) 103-113.
124. M.H. Wagner, V.H. Rolón-Garrido, K. Hyun, M. Wilhelm, Journal of Rheology 55 (2011) 495-516.
125. C.W. Macosko, Rheology: principles, measurements, and applications, Wiley-VCH, 1994.
126. J. Meissner, J. Hostettler, Rheologica Acta 33 (1994) 1-21.
127. H. Janeschitz-Kriegl, Polymer melt rheology and flow birefringence, Springer, 2012.
128. E. Bagley, Journal of Applied Physics 28 (1957) 624-627.
129. R. Eisenschitz, B. Rabinowitsch, K. Weissenberg, Zur Analyse des formänderungswiderstandes. Mitteilungen der deutschen Materialprüfungsanstalten, Springer, 1929.
130. H.M. Laun, Rheologica Acta 22 (1983) 171-185.
131. A. Senouci, A. Smith, Rheologica Acta 27 (1988) 546-554.
132. H.M. Laun, Rheologica Acta 42 (2003) 295-308.
133. W.P. Cox, E.H. Merz, Journal of Polymer Science 28 (1958) 619-622.
134. E. Morris, A. Cutler, S. Ross-Murphy, D. Rees, J. Price, Carbohydrate polymers (1981) 5-21.
135. T. Matsumoto, C. Hitomi, S. Onogi, Transactions of the Society of Rheology 19 (1975) 541-555.
136. W.-M. Kulicke, R. Porter, Rheologica Acta 19 (1980) 601-605.
137. W. Yang, M. Rao, Journal of food process engineering (1998) 191-207.
138. F. Fourné, Synthetic Fibers, Machines and Equipment, 1999.
139. M. Baerns, A. Behr, A. Brehm, J. Gmehling, H. Hofmann, U. Onken, Technische chemie, John Wiley & Sons, 2013.
140. M.E. Carter, Essential fiber chemistry, Dekker, 1971.
141. Z.K. Walczak, Processes of fiber formation, Elsevier, 2002.
142. C.D. Han, Rheology and Processing of Polymeric Materials: vol. 2: Polymer Processing, Oxford University Press, 2007.
143. A. Formhals. Process and apparatus for preparing artificial threads. US Patent, 1975504. 1934.
144. A. Södergard, M. Stolt. Poly (lactic acid): Synthesis, Structures, Properties, Processing and Applications, edited by R. Auras, L.T. Lim, SEM Selke, and H. Tsuji. John Wiley & Sons, 2010.
145. V. Gupta, V. Kothari, Manufactured fibre technology, Springer, 2012.
146. A. Ziabicki, H. Kawai, High-speed fiber spinning: science and engineering aspects, Wiley-Interscience, 1985.
147. J.W. Hearle, L. Hollick, D.K. Wilson, Yarn texturing technology, Elsevier, 2001.
148. M. Lewin, E.M. Pearce, Handbook of fiber chemistry, Crc press, 1998.
149. R. Beyreuther, R. Vogel, International Polymer Processing 11 (1996) 154-158.
150. A. Ziabicki, Fundamentals of Fiber Formation, Wiley, 1976.
151. S. Kase, Rheologica Acta 21 (1982) 210-211.
152. T. Matsuo, S. Kase, Journal of Applied Polymer Science 20 (1976) 367-376.
153. S. Kase, Journal of Applied Polymer Science 27 (1982) 2729-2730.
154. S.G. Hatzikiriakos, K.B. Migler, Polymer processing instabilities: control and understanding, CRC Press, 2004.

155. Y. Ide, J.L. White, Journal of Applied Polymer Science 20 (1976) 2511-2531.
156. Y. Ide, J.L. White, Journal of Non-Newtonian Fluid Mechanics 2 (1977) 281-298.
157. H. Chang, A. Lodge, Rheologica Acta 10 (1971) 448-449.
158. J.L. White, Y. Ide, Journal of Applied Polymer Science 22 (1978) 3057-3074.
159. C.J. Petrie, M.M. Denn, AIChE Journal 22 (1976) 209-236.
160. H. Palza, I.F. Naue, M. Wilhelm, Macromolecular rapid communications 30 (2009) 1799-1804.
161. R. Kádár, I. Naue, M. Wilhelm. Simultaneous in-situ analysis of instabilities and first normal stress difference during polymer melt extrusion flows. Transactions Nordic Rheology Society, vol. 22, 2014.
162. Z.M. Wang, One-dimensional nanostructures, Springer, 2008.
163. S. Fakirov, Nano-size Polymers, Springer, 2017.
164. N. Bhardwaj, S.C. Kundu, Biotechnology advances 28 (2010) 325-347.
165. J. Cooley, Apparatus for Electrically Dispersing Fluids US Patent Specification, 692631, (1902).
166. C.L. Norton. Method of and apparatus for producing fibrous or filamentary material. Google Patents, 1936.
167. J. Doshi, D.H. Reneker, Journal of electrostatics 35 (1995) 151-160.
168. D.H. Reneker, I. Chun, Nanotechnology 7 (1996) 216.
169. S.V. Fridrikh, J.H. Yu, M.P. Brenner, G.C. Rutledge, Physical Review Letters 90 (2003) 144502.
170. J.H. Wendorff, S. Agarwal, A. Greiner, Electrospinning: Materials, Processing, and Applications, Wiley-VCH, 2012.
171. X.H. Qin, S.Y. Wang, Journal of Applied Polymer Science 102 (2006) 1285-1290.
172. M. Langner, A. Greiner, Macromolecular Rapid Communications 37(2016), 351-355.
173. Y. Dai, W. Liu, E. Formo, Y. Sun, Y. Xia, Polymers for Advanced Technologies 22 (2011) 326-338.
174. M. Gorji, A.A.A. Jeddi, A.A. Gharehaghaji, Journal of Applied Polymer Science 125 (2012) 4135-4141.
175. D. Aussawasathien, J.H. Dong, L. Dai, Synthetic Metals 154 (2005) 37-40.
176. W.J. Li, C.T. Laurencin, E.J. Caterson, R.S. Tuan, F.K. Ko, Journal of Biomedical Materials Research, Part A 60 (2002) 613-621.
177. T.J. Sill, H.A. von Recum, Biomaterials 29 (2008) 1989-2006.
178. R. Kenawy el, G.L. Bowlin, K. Mansfield, J. Layman, D.G. Simpson, E.H. Sanders, G.E. Wnek, Journal of Controlled Release 81 (2002) 57-64.
179. D. Ahirwal, A. Hebraud, R. Kadar, M. Wilhelm, G. Schlatter, Soft Matter 9 (2013) 3164-3172.
180. I.L. Pereira, E. Ayres, L. Averous, G. Schlatter, A. Hebraud, A. de Paula, P. Viana, A. Goes, R. Oréfice, Journal of Materials Science: Materials in Medicine 25 (2014) 1137-1148.
181. S. Agarwal, J.H. Wendorff, A. Greiner, Polymer 49 (2008) 5603-5621.
182. S.L. Shenoy, W.D. Bates, H.L. Frisch, G.E. Wnek, Polymer 46 (2005) 3372-3384.
183. P.D. Dalton, D. Grafahrend, K. Klinkhammer, D. Klee, M. Möller, Polymer 48 (2007) 6823-6833.
184. D.H. Reneker, A.L. Yarin, E. Zussman, H. Xu, Advances in Applied Mechanics 41 (2007) 43-346.

185. L. Larrondo, R. St John Manley, Journal of Polymer Science Part B: Polymer Physics 19 (1981) 909-920.
186. L. Palangetic, N.K. Reddy, S. Srinivasan, R.E. Cohen, G.H. McKinley, C. Clasen, Polymer 55 (2014) 4920-4931.
187. P. Gupta, C. Elkins, T.E. Long, G.L. Wilkes, Polymer 46 (2005) 4799-4810.
188. S.H. Tan, R. Inai, M. Kotaki, S. Ramakrishna, Polymer 46 (2005) 6128-6134.
189. S. Megelski, J.S. Stephens, D.B. Chase, J.F. Rabolt, Macromolecules 35 (2002) 8456-8466.
190. C.J. Luo, M. Nangrejo, M. Edirisinghe, Polymer 51 (2010) 1654-1662.
191. M.G. McKee, G.L. Wilkes, R.H. Colby, T.E. Long, Macromolecules 37 (2004) 1760-1767.
192. B. Hager, G. Berry, Journal of Polymer Science Part B: Polymer Physics 20 (1982) 911-928.
193. A.V. Dobrynin, R.H. Colby, M. Rubinstein, Macromolecules 28 (1995) 1859-1871.
194. P. De Gennes, Macromolecules 9 (1976) 587-593.
195. P.G. de Gennes, Scaling Concepts in Polymer Physics, Cornell University, 1979.
196. R.H. Colby, L.J. Fetters, W.G. Funk, W.W. Graessley, Macromolecules 24 (1991) 3873-3882.
197. N. Hudson, W.A. MacDonald, A. Neilson, R.W. Richards, D.C. Sherrington, Macromolecules 33 (2000) 9255-9261.
198. A. Lederer, W. Burchard, A. Khalyavina, P. Lindner, R. Schweins, Angewandte Chemie International Edition 52 (2013) 4659-4663.
199. W. Radke, A.H.E. Müller, Macromolecules 38 (2005) 3949-3960.
200. A. Sinha, M.N. Roy, Physics and Chemistry of Liquids 44 (2006) 303-314.
201. C. Wang, C.H. Hsu, J.H. Lin, Macromolecules 39 (2006) 7662-7672.
202. M.L. Huggins, Journal of the American Chemical Society 64 (1942) 2716-2718.
203. W.-M. Kulicke, R. Kniewske, Rheologica Acta 23 (1984) 75-83.
204. L. Wannatong, A. Sirivat, P. Supaphol, Polymer International 53 (2004) 1851-1859.
205. G. Eda, S. Shivkumar, Journal of Applied Polymer Science 106 (2007) 475-487.
206. S.L. Anna, G.H. McKinley, Journal of Rheology 45 (2001) 115-138.
207. L.E. Rodd, T.P. Scott, J.J. Cooper-White, G.H. McKinley, Capillary break-up rheometry of low-viscosity elastic fluids,2004.
208. G.H. McKinley, O. Brauner, M. Yao, Korea-Australia Rheology Journal 13 (2001) 29-35.
209. M.I. Kolte, P. Szabo, Journal of Rheology 43 (1999) 609-625.
210. H.Y. Jian, S.V. Fridrikh, G.C. Rutledge, Polymer 47 (2006) 4789-4797.
211. L. Chen, L. Bromberg, T.A. Hatton, G.C. Rutledge, Polymer 49 (2008) 1266-1275.
212. H.-C. Chang, E.A. Demekhin, E. Kalaidin, Physics of Fluids 11 (1999) 1717-1737.
213. M. Stelter, G. Brenn, A. Yarin, R. Singh, F. Durst, Journal of Rheology 44 (2000) 595-616.
214. J. Li, M.A. Fontelos, Physics of Fluids 15 (2003) 922-937.
215. C. Clasen, J. Eggers, M.A. Fontelos, J. Li, G.H. McKinley, Journal of Fluid Mechanics 556 (2006) 283-308.
216. C.O. Klein, I.F.C. Naue, J. Nijman, M. Wilhelm, Soft Matter 7 (2009) 242-257.

217.  A. Zosel, Colloid & Polymer Science 263 (1985) 541-553.
218.  A. Zosel, The Journal of Adhesion 34 (1991) 201-209.
219.  A. Zosel, Journal of adhesion Science and technology 11 (1997) 1447-1457.
220.  A. Zosel, International journal of adhesion and adhesives 18 (1998) 265-271.
221.  M. Abbasi, L. Faust, K. Riazi, M. Wilhelm, Macromolecules 50 (2017) 5964-5977.
222.  R.F. Egerton, Physical principles of electron microscopy, Springer, 2005.
223.  P. Hawkes, J.C. Spence, Science of microscopy, Springer, 2008.
224.  L. Laperrire, G. Reinhart, CIRP encyclopedia of production engineering, Springer, 2014.
225.  H.N. Hansen, K. Carneiro, H. Haitjema, L. De Chiffre, CIRP Annals-Manufacturing Technology 55 (2006) 721-743.
226.  R.J. Young, P.A. Lovell, Introduction to polymers, CRC press, 2011.

## Appendix

### A. High vacuum line for anionic polymerization.
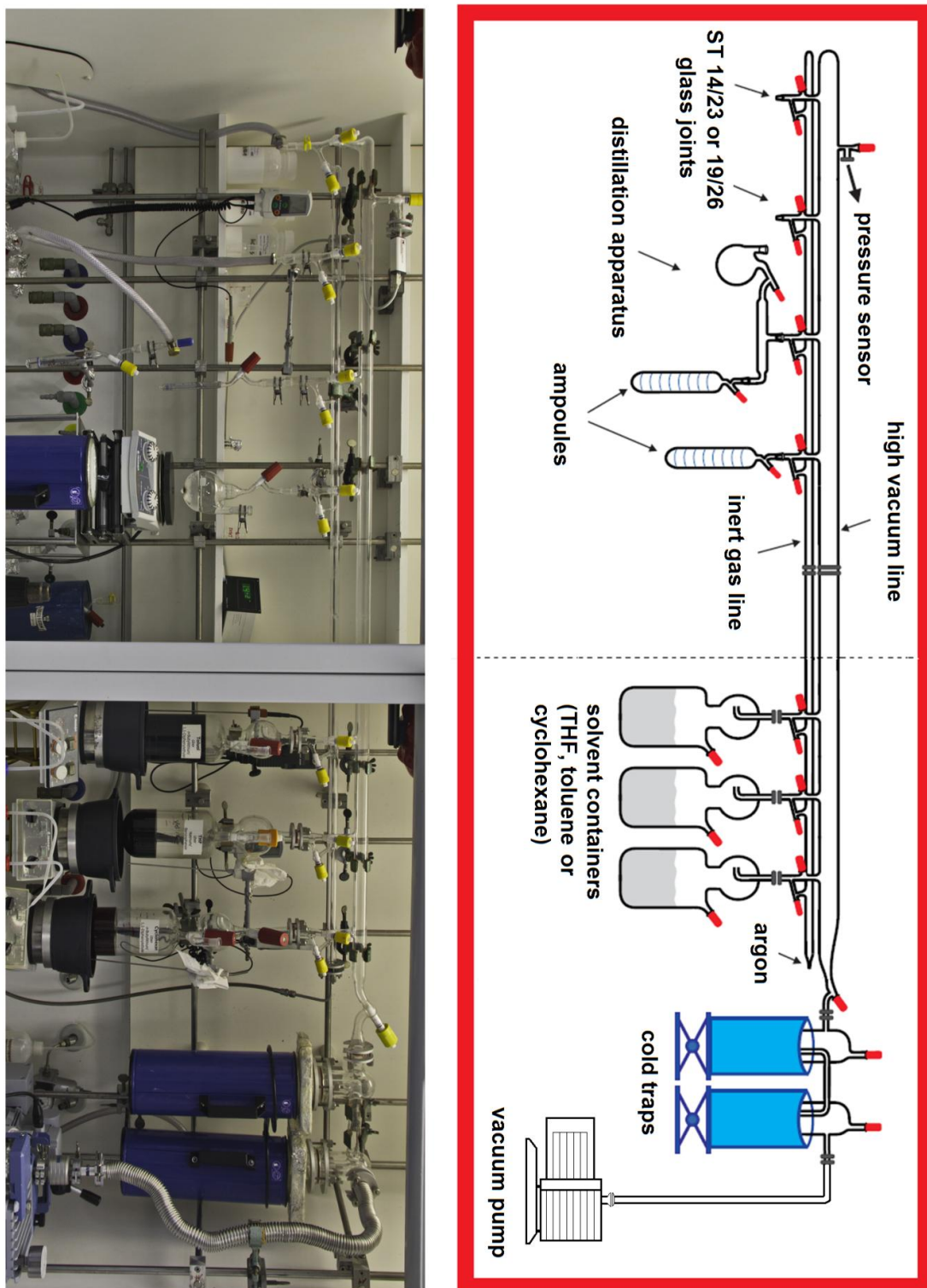


Figure a1: The construction of a glass high vacuum line for anionic polymerization, which was used for the synthesis of the polymers used in this work.

## B. Molar mass distribution of polymer synthesized by anionic polymerization

At the beginning of the anionic polymerization ($t = 0$), there are $N_0$ initiator species, which are able to initiate the monomers and they are equally active. It is assumed that the average rate at which a molecule monomer is added to a single active center (either an initiator species or a propagation chain) is equal ($k_i = k_p = k$). After a time $t$, $N$ of these initiator species decreases as follows [226]:

$$-\frac{dN}{dt} = kN \qquad (a.1)$$

with applying the integration limits:

$$\int_{N_0}^{N} \frac{dN}{N} = -\int_{0}^{t} kdt \qquad (a.2)$$

which by letting $\lambda = \int_{0}^{t} kdt$ can be solved as follows:

$$N = N_0 e^{-\lambda} \qquad (a.3)$$

The rate of change in the numbers of all other species $N_i$ ($i \in \mathbb{N}$) is given by the following equation:

$$\frac{dN_i}{dt} = k(N_{i-1} - N_i) \qquad (a.4)$$

since an $i$-mer is formed by addition of monomer to an $(i-1)$-mer. Recognizing that $d\lambda = Kdt$, the equation a.4 can be rearranged as follows:

$$\frac{dN_i}{d\lambda} + N_i = N_{i-1} \qquad (a.5)$$

The solution of the first order linear differential equation for $i \in \mathbb{N}$ gives:

$$N_1 = N_0 \lambda e^{-\lambda}$$

$$N_2 = N_0 \left(\frac{\lambda^2}{2!}\right) e^{-\lambda}$$

…

$$N_i = N_0 \left(\frac{\lambda^i}{i!}\right) e^{-\lambda} \qquad (a.6)$$

or

$$N_i = N_0 P(i) \qquad (a.7)$$

where $P(x)$ is the mole fraction of $i$-mers. The equation a.7 is similar to the frequency function of Poisson distribution and so the polymer has a Poisson distribution of molar mass. The number average molar mass of the polymer is given by:

$$M_n = \sum_{i=1}^{\infty} P(i) M_i \qquad (a.8)$$

Where $M_i$ is the molar mass of an i-mer $M_i = iM_0$, and $M_0$ is the molar mass of the monomer.

Using the mathematical relation $i^\lambda = \sum_{i=1}^{\infty} \lambda^i / i!$ and Equations a.6, a.7 and a.8, $M_n$ reduced to:

$$M_n = \lambda M_0 \qquad (a.9)$$

The total mass of polymer with $N$ living polymer molecules is $NM_0\lambda$. Thus, the weight fraction $w_i$ of $i$-mers is given by:

$$w_i = \frac{N_i M_i}{N M_0 \lambda} \qquad (a.10)$$

From Equation a.10, a.6 and $M_i = \lambda M_0$:

$$w_i = \frac{e^{-\lambda} \lambda^{i-1}}{(i-1)!} \qquad (a.11)$$

The weight-average molar mass is $M_w = \sum_{i=1}^{\infty} w_i M_i$. Using Equation a.11 and the mathematical relation $\sum_{i=1}^{\infty} i\lambda^{i-1}/(i-1)!$, the weight average molecular weight can be calculated as follows:

$$M_w = M_0(\lambda + 1) \qquad \text{(a.12)}$$

From Equation a.9 and a.12 the dispersity Đ for anionic polymerization calculated as follows:

$$Đ = \frac{M_w}{M_n} = \frac{1 + \lambda}{\lambda} = 1 + \frac{1}{\lambda}$$

# ACKNOWLEDGMENTS

**Christoph Pfeifer** and **Volker Räntzsch** for correcting parts of my thesis. My special thanks to Volker for interesting discussions about the crystallization of polyolefins.

**The group** of Prof. Wilhelm for their ongoing help and friendship. Also, thank you for enjoyable BBQs, Christmas parties and so on.

All the alumni of our group, especially **Dr. Timo Beskers**, **Dr. Lukas Schwab** and **Dr. Dimitri Merger**, for their help, their support and for all the enjoyable times with them.

**Sabine Weiland, Wolfgang Arbogast, Helena Hörig and Daniel Zimmermann,** for logistical help with all the adminstration works at the KIT, for DSC measurements and the many technical drawings.

A special thank you goes out to **my parents** who basically made all this work possible.

And last, but not least, to my wonderful wife **Azadeh** for her patience and support, especially during the last few months.